

Diss. ETH No. 16411

Heterogeneous ice nucleation in upper tropospheric aerosols

A dissertation submitted to the
SWISS FEDERAL INSTITUTE OF TECHNOLOGY
ZURICH

for the degree of
Doctor of Natural Sciences

presented by
BERNHARD ZOBRIST
Dipl. Natw. ETH
born 10. June 1975
citizen of Rapperswil, Switzerland

accepted on the recommendation of
Prof. Dr. T. Peter, examiner
Prof. Dr. T. Koop, co-examiner
Prof. Dr. R. Schwarzenbach, co-examiner
Dr. C. Marcolli, co-examiner

2006

Abstract

Cirrus clouds cover about 30% of the Earth's surface, affecting chemical and physical processes of the atmosphere. Their presence increases the scattering and absorption of solar radiation as well as the absorption of long wave terrestrial radiation. A change in cirrus cloud coverage may significantly alter the global radiation balance and hence the Earth's climate. So far, the exact mechanisms of cirrus cloud formation are largely unknown. Ice particles in cirrus clouds can form via homogeneous ice nucleation from liquid aerosols or by heterogeneous ice nucleation on solid ice nuclei (IN). Four different pathways have to be distinguished for heterogeneous ice nucleation, namely immersion, deposition, condensation and contact mode. It seems likely that solid IN may appear immersed in liquid aerosols in the upper troposphere (UT). Therefore, heterogeneous freezing experiments with four different IN (composed of nonadecanol, silica, silver iodide and oxalic acid) immersed in aqueous solutions have been investigated in a differential scanning calorimeter (DSC) and in a custom made single droplet apparatus. The results of the different IN show a consistent picture, namely the freezing temperatures are decreasing with decreasing water activity (a_w) of the solution. It was found that a constant offset ($\Delta a_{w,\text{het}}$) with respect to the ice melting curve can describe each data series very well, with $\Delta a_{w,\text{het}} = 0.101, 0.173, 0.180$ and 0.285 for IN containing nonadecanol, silica, silver iodide and oxalic acid, respectively. Heterogeneous ice nucleation rate coefficients (j_{het}) have been estimated from DSC freezing peaks for the emulsified aqueous solution samples with immersed silver iodide and oxalic acid. The obtained j_{het} values for different aqueous solutions containing the same kind of IN scatter by less than 1 order of magnitude. This implies that for a specific $\Delta a_{w,\text{het}}$ a constant j_{het} can be assumed for heterogeneous ice nucleation in the immersion mode. Therefore water activity based nucleation theory can be used to parameterize heterogeneous ice nucleation in the immersion mode analogously to homogeneous ice nucleation from supercooled liquid droplets.

Single particle aerosol mass spectrometry has observed oxalic acid in several field campaigns in the UT. Often large fractions of individual particles were oxalic acid, so that the present work argues that the oxalic acid occurs most likely in solid form with low volatility. The parameterization for oxalic acid obtained from the measurements (i.e., $\Delta a_{w,\text{het}}=0.285$) was implemented in a 1D microphysical model to estimate the possible effect of this ice nucleus on cirrus cloud properties. The results indicate that the ice number density (n_{ice}) of cirrus clouds containing solid oxalic acid IN is reduced by $\sim 50\%$ when compared to cirrus that exclusively formed by homogeneous nucleation. Such a reduction leads to optically thinner cirrus clouds and to faster sedimentation of ice particles. The global impact of the reduced n_{ice} caused by heterogeneous freezing of oxalic acid is estimated by the ECHAM4 global climate model to -0.3 Wm^{-2} , whereas the shortwave and longwave radiative forcing at the top-of-the atmosphere is considered. This result indicates the importance of heterogeneous ice nucleation for global climate.

Seite Leer /
Blank leaf

Zusammenfassung

Zirren bedecken rund 30% der Erdoberfläche und haben somit einen grossen Einfluss auf die chemischen und physikalischen Prozesse in der Atmosphäre. Sie verstärken sowohl die Streuung und Absorption von kurzwelliger Solarstrahlung als auch die Absorption langwelliger terrestrischer Strahlung. Eine Änderung des Zirren-Bedeckungsgrades könnte somit den globalen Strahlungshaushalt beträchtlich beeinflussen. Die exakten Bildungsmechanismen von Zirren sind bis jetzt nicht verstanden. Zirrus-Eisteilchen in der Atmosphäre können jedoch durch homogene oder heterogene Eisnukleation entstehen. Im letzteren Fall wird die Nukleation durch einen festen Eiskeim induziert, und dabei wird zwischen vier möglichen Gefriervorgängen unterschieden: Den Immersions-, den Depositions-, den Kondensations- und den Kontaktmodus. Da flüssige Aerosole in der oberen Troposphäre mit einem eingelagerten Eiskeim vorkommen können, wurden in dieser Arbeit heterogene Gefrierpunktmessungen von flüssigen Tröpfchen mit vier verschiedenen eingelagerten Eiskeimen untersucht (Nonadecanol, Siliziumdioxid, Silberiodid und Oxalsäure). Die Experimente wurden mit einem Dynamischen Differenz Kalorimeter (DSC) sowie mit einem selbst entwickelten Einzeltropfen-Kühlapparat durchgeführt. Die Gefriertemperaturen von Tropfen mit verschiedenen Eiskeimen weisen ein einheitliches Verhalten auf, nämlich eine Abnahme der Gefriertemperatur mit abnehmender Wasseraktivität (a_w) der Lösung. Ein konstantes $\Delta a_{w,het}$ in Bezug auf die Eisschmelzkurve von 0.101, 0.173, 0.180 und 0.285 wurde für Nonadecanol, Siliziumdioxid, Silberiodid und Oxalsäure bestimmt. Für die Experimente mit Nonadecanol und Oxalsäure wurden aus den gemessenen DSC Gefrierpeaks heterogene Eisnukleationsratenkoeffizienten (j_{het}) hergeleitet, wobei die Unterschiede für die verschiedenen Lösungen des jeweiligen Eiskeims kleiner als eine Grössenordnung sind. Diese Resultate zeigen, dass für ein bestimmtes $\Delta a_{w,het}$ ein konstantes j_{het} angenommen werden kann. Somit kann die auf Wasseraktivität basierende Nukleationstheorie für homogene Eisnukleation auch auf die heterogene Eisnukleation im Immersionsmodus ausgeweitet werden.

Massenspektrometrie an einzelnen Aerosolen hat in diversen Feldkampagnen feste Oxalsäure in der oberen Troposphäre nachgewiesen. Die Parametrisierung für die Experimente mit fester Oxalsäure wurde deshalb in ein 1-D mikrophysikalisches Modell eingebunden, um den Einfluss von diesem Eiskeim auf die mikrophysikalischen Eigenschaften von Zirren abzuschätzen. Die Resultate zeigen, dass die Eisteilchenanzahldichte (n_{ice}) für Zirren mit fester Oxalsäure $\sim 50\%$ kleiner ist als diejenige von homogen gefrorenen Zirren. Diese Reduktion führt zu optisch dünneren Zirren und zu einer Verstärkung von Eisteilchensedimentation. Das Klima Modell ECHAM4 schätzt den globalen Einfluss der verringerten n_{ice} auf -0.3 Wm^{-2} ab, wobei für die Simulation der kurz- und langwellige Strahlungsantrieb an der Obergrenze der Atmosphäre berücksichtigt wurde. Dieser beträchtliche Nettostrahlungsantrieb zeigt eindrücklich die Bedeutung der heterogenen Eisnukleation auf das globale Klima.

Seite Leer /
Blank leaf

Contents

Abstract	i
Zusammenfassung	iii
1 Introduction	1
1.1 The atmosphere	1
1.1.1 Evolution of the atmosphere and future climate change	2
1.2 Aerosols	3
1.3 Cirrus clouds and contrails	5
1.3.1 Cirrus clouds	5
1.3.2 Contrails	8
1.3.3 Ice particles in the lower troposphere	8
1.4 Ice nucleation in the atmosphere	9
1.5 Objectives of the thesis	11
2 Theory	13
2.1 Classical nucleation theory	13
2.1.1 Homogeneous ice nucleation	13
2.1.2 Heterogeneous ice nucleation	17
2.2 Water activity based ice nucleation theory	19
2.3 Statistical description of the ice nucleation process	21
3 Experimental	25
3.1 Differential scanning calorimetry	25

3.1.1	Emulsion calorimetry	26
3.1.2	Emulsion preparation	27
3.1.3	Typical DSC experiment	27
3.2	Single droplets cooling stage	29
3.2.1	Experimental setup	29
3.2.2	Typical experimental run	30
3.3	Linkam cooling stage	31
3.4	Silica globules synthesis	32
4	Results and discussion	35
4.1	Heterogeneous ice nucleation rate coefficients of water droplets covered with nonadecanol	35
4.2	Ice freezing experiments with various ice nuclei	45
4.2.1	Nonadecanol	45
4.2.2	Silver iodide (AgI)	47
4.2.3	Silica (SiO ₂)	49
4.2.4	Dicarboxylic acids	52
4.2.5	Miscellaneous IN	59
4.3	Water activity based ice nucleation theory for heterogeneous ice nucleation	60
4.4	Heterogeneous rate coefficients estimation from DSC freezing peaks	66
5	Atmospheric implications	73
5.1	Oxalic acid as a heterogeneous ice nucleus in the upper troposphere and its indirect aerosol effect	73
5.2	Nonadecanol and heterogeneous ice nucleation in the atmosphere	98
6	Conclusions and Outlook	101
6.1	Conclusions	101
6.2	Outlook	103
	Appendix	105
A	Temperature calibrations	105

A.1	DSC	105
A.1.1	Absolute temperature calibration	105
A.1.2	Freezing point calibration	105
A.1.3	Melting point calibration	106
A.1.4	Accuracy and precision of the different calibrations	107
A.2	Single droplet cooling stage	107
A.3	Linkam cooling stage	109
B	Statistical analysis	111
B.1	Comparison of the freezing temperatures of droplets covered with nonadecanol at the air/water and at the oil/water interface	111
B.2	t-test for the slopes of series of single droplets	112
B.3	Upper and lower limits of the poisson statistics	112
C	Heterogeneous freezing points measurements	115
C.1	Large droplets covered with nonadecanol	115
C.2	Emulsions with immersed AgI	115
C.3	Large droplets with suspended SiO ₂	115
	Bibliography	120
	Acknowledgments	135

Seite Leer /
Blank leaf

List of Figures

1.1	Structure of the atmosphere.	2
1.2	Anthropogenic forcing for several atmospheric factors	4
1.3	Photographs of different types of cirrus clouds and contrails	6
1.4	Scheme of the differences between homogeneous and heterogenous ice nucleation	9
2.1	The Gibbs free energy for a ice nucleation process	15
2.2	The contact angle α of an ice nucleus immersed in a liquid droplet	18
2.3	Homogeneous ice freezing points as a function of water activity	20
3.1	Schematic sketch of the emulsion calorimetry.	26
3.2	Photograph of an emulsion	27
3.3	Typical DSC experiment	28
3.4	Phase diagram of the binary NaCl/water system together with a heating curve of an emulsion made of a 9.9 wt% NaCl solution	29
3.5	Schematic diagram of the single droplet apparatus.	30
3.6	Detailed setup of the cooling cell.	31
3.7	Setup of the Linkam cooling stage	32
3.8	Photograph of the SiO ₂ globules	33
4.1	Scheme of a self assembled monolayer on a liquid droplet	36
4.2	Measured freezing points for six droplets covered with nonadecanol and one uncoated droplet as a function of iteration number	37
4.3	Measured heterogenous rate coefficients for the uncoated droplet as a function of temperature	40
4.4	Contact angle as a function of temperature	41

4.5	Heterogeneous rate coefficients of droplets covered with nonadecanol	42
4.6	Scheme of the basal <i>ab</i> plane of hexagonal ice	43
4.7	Ice melting and heterogeneous freezing points of different aqueous solution droplets covered with nonadecanol	46
4.8	DSC freezing curve of an emulsion containing in situ precipitated AgI	49
4.9	Homogeneous and heterogeneous freezing and corresponding ice melting points of emulsified aqueous solutions with immersed AgI	50
4.10	Heterogeneous freezing points of large droplets with suspended SiO ₂	52
4.11	DSC heat flow measurements of a 4.95 wt% oxalic acid/water solution	54
4.12	Heterogeneous freezing experiments with immersed Al ₂ O ₃	59
4.13	Heterogeneous freezing points of various IN as a function of a_w	61
4.14	Heterogeneous and homogeneous freezing points for different aqueous solutions with immersed AgI and OAD as a function of a_w	62
4.15	Heterogeneous freezing points of various IN as a function of a_w	63
4.16	Comparison of water activity based nucleation theory versus the λ -approach	66
4.17	DSC freezing peak of a homogeneously nucleated emulsified water sample	68
5.1	Typical DSC heat flow experiment of a oxalic acid/water solution	78
5.2	Experimental freezing points of micrometer sized aqueous solution droplets containing solid OAD	84
5.3	PALMS mass spectra of a single particle containing oxalic acid	87
5.4	Ice number density as a function of cooling rates for homogeneous and heterogeneous ice nucleation with OAD	88
5.5	Simulated ice particle number density distributions at different height levels	89
5.6	Global shortwave, longwave and net TOA effect calculated with the ECHAM4-model	91
5.7	Radius of ice particles as a function of ice number density per bin	99
5.8	Heterogeneous freezing temperatures of large droplets covered with a partial nonadecanol monolayer	100

List of Tables

3.1	Required ingredients for the SiO ₂ globules synthesis	32
4.1	Analysis of ice nucleation properties for six droplets coated with nonadecanol and one uncoated droplet	39
4.2	Lattice parameters of the 2D crystalline structure for different long chain alcohols.	44
4.3	Freezing point comparison of large droplets with and without suspended SiO ₂	51
4.4	Summary of experiments with binary dicarboxylic acid/water systems	55
4.5	Summary of measurements for oxalic acid/aqueous solution systems	57
4.6	λ and $T_{f0,het}$ for nonadecanol, SiO ₂ , AgI and OAD	65
4.7	Sensitivity study of j_{hom} for different τ and r_{drop} values	69
4.8	Calculated $j_{het,AgI}$ for emulsified samples containing solid AgI	70
4.9	Calculated $j_{het,OAD}$ for emulsified samples containing immersed OAD	71
5.1	Summary of experiments with binary dicarboxylic acid/water systems	79
5.2	Summary of measurements for oxalic acid/aqueous solution systems	81
5.3	Vapor pressure measurement of aqueous oxalic acid droplets	95
A.1	Absolute temperature calibration of the DSC	106
A.2	Freezing point calibration of the DSC	106
A.3	Melting point calibration for pure substances in the DSC	108
A.4	Melting point calibration for emulsified aqueous solutions of the DSC	108
A.5	Absolute temperature calibration of the single droplet apparatus	109
B.1	Statistical comparison of the freezing temperature of droplets covered with nonadecanol at the air/water and at the oil/water interface	111

B.2	t-test statistics for the slopes for the data series of single droplets	112
B.3	Upper and lower freezing event limits of the poisson statistics on the 95% confidence level	113
C.1	Heterogenous freezing and melting points of droplets covered with nonadecanol	116
C.2	Homogeneous, heterogcneous and ice melting points of emulsified samples containing immersed AgI	117
C.3	Heterogcncous freezing points of large droplets with suspended SiO ₂	119

Chapter 1

Introduction

1.1 The atmosphere

The Earth's atmosphere is viewed as the gas layer surrounding our planet, retained by gravity. Figure 1.1 shows temperature and pressure of the US standard atmosphere as a function of altitude. As the altitude within the atmosphere increases, the number of molecules is decreasing leading to an exponential decrease of atmospheric pressure with increasing altitude. Already at around 5 km, the pressure has halved compared to ground level pressure. In the troposphere, the temperature is decreasing due to adiabatic expansion and reaches a minimum at the tropopause. The ozone (O_3) in the stratosphere absorbs UV radiation and causes an increase in temperature with height, which reaches its maximum at ~ 50 km. The temperature is then decreasing again and reaches a second minimum at the mesopause. Above this level, hard UV radiation is absorbed by N_2 and O_2 and leading again to a temperature increase.

The troposphere can be considered as the layer in which weather takes place and where most of earth/atmosphere interactions occur (e.g., the hydrological cycle). Depending on latitude and season, the height of the tropopause reaches values up to 18 km in the tropics, compared to ~ 8 km in polar regions. In Fig. 1.1 a mean value of 12 km is depicted for the tropopause. The bluish area in Fig. 1.1 between 6 and 17 km indicates the region where cirrus clouds may occur in the troposphere.

Besides diverse trace gases (e.g., CO_2 , H_2O , CH_4 , NO_x , O_3), the atmosphere consists of three major components, namely N_2 (78%), O_2 (21%) and argon (1%). The mixing ratios of these three gases are constant. However, the concentrations of the trace gases can exhibit changes in time and altitude. Since some of them are reactive species (e.g., NO_x , O_3) and/or may have a large greenhouse potential (e.g., H_2O , CO_2 , CH_4), they are of great interest in atmospheric sciences. Besides gases, the atmosphere contains also a great variety of aerosols. Aerosol particles (~ 0.002 - $50 \mu m$) are suspended as solids or liquids or can exist also as a mixture of both (Scinfeld and Pandis, 1998). Some aerosols

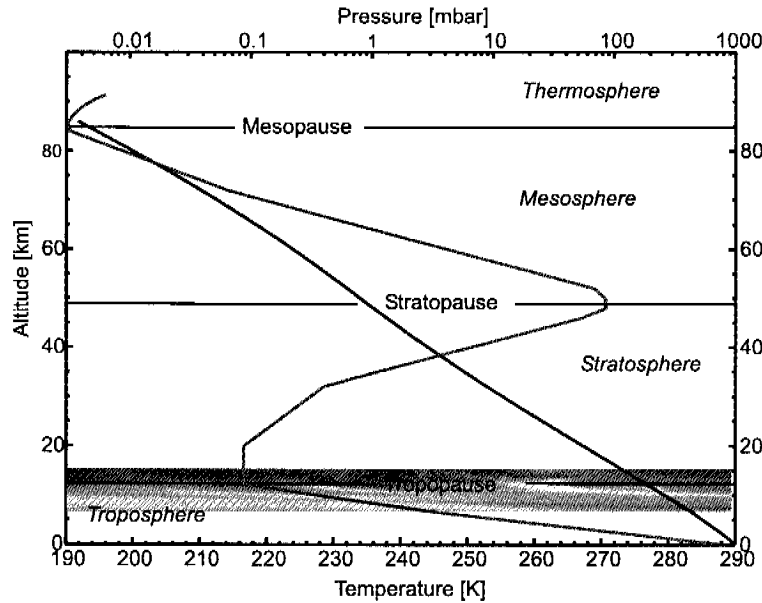


Figure 1.1: *Temperature (red line) and pressure (blue line) of the US standard atmosphere as a function of altitude. The different strata are given in italic letters, whereas their boundaries are depicted by the black horizontal lines. The area between ~ 6 and 17 km indicates the altitudes of cirrus occurrence. Note that a mean value of 12 km is assumed for the tropopause, but depending on season and latitude it may assume values between 8 to 18 km.*

are produced naturally, originating from volcanoes, dust storms, forest and grassland fires, living vegetation, and sea spray. But, burning of fossil fuels, industrial and other anthropogenic activities also generate large amounts of various aerosols, which alter the chemical and physical properties of the atmosphere (Finlayson-Pitts and Pitts, 2000).

1.1.1 Evolution of the atmosphere and future climate change

Over the entire lifetime of the Earth, the chemical composition of the atmosphere has changed several times. In the beginning, the two light molecules H_2 and He were dominant, but these two gases were mostly lost to space (Wayne, 2000). At a later time, large volcanoes led to a H_2O ($\sim 80\%$), CO_2 ($\sim 11\%$), H_2S ($\sim 6\%$) dominated atmosphere. Over the years, Earth was cooling down, and the released water vapor started to condense and oceans were formed by large rainfalls (Wayne, 2000). In these newly created oceans, life has developed. The O_2 concentration was increased due to photosynthesis by anaerobic bacteria. However, since the O_3 layer was not formed yet, stronger UV radiation than nowadays reached the Earth surface, and thus most of the oxygen was converted into O_3 via photolysis of molecular oxygen. At this time, the oxidation from Fe^{2+} to Fe^{3+} was a

second large sink for the O_2 concentration (Graedel and Crutzen, 1994). While the ozone concentration increased, less shortwave UV radiation reached the Earth surface because of the large absorption of this radiation by O_3 molecules in the stratosphere. Therefore, the situation on Earth was improved for biogenic evolution, which enforced photosynthesis intensity and therefore led to an enrichment in the O_2 concentration. Around three to four hundred million years ago, the O_2 as well as the O_3 have reached current concentrations (Seinfeld and Pandis, 1998). On the other hand, human activities have led in this century to a strong decrease of the O_3 concentration in some parts of the ozone layer in the stratosphere, which can result in harmful damages for human beings, flora and fauna. Because of the inert behavior of N_2 , its fraction was continuously increasing with decreasing total pressure of the Earth's atmosphere (Wayne, 2000). In contrast, CO_2 concentration has fluctuated also on smaller time scales, resulting in a change of the global mean temperature. Good agreement between increasing CO_2 concentration and increasing temperature was found in ice cores of the Antarctica (Petit et al., 1999). In current climate discussions, the increasing CO_2 concentration is assumed to have the largest influence on the rising global mean temperature. But besides CO_2 , other greenhouse gases such as methane (CH_4), nitrous oxide (N_2O), O_3 and halocarbons also enforce the anthropogenic greenhouse effect. It is assumed, that all greenhouse gases that are released by human activities together have caused a global mean radiative forcing of $\sim +2.5 \text{ Wm}^{-2}$ compared to 1750 (Fig. 1.2). However, several other climate factors are poorly understood and less well quantified. The indirect aerosol effect, for example, is not well understood yet, but might be similar in the size but with opposite sign compared to the effect of well-mixed greenhouse gases. The large uncertainties (indicated by the vertical lines in Fig. 1.2) connected with the different types of forcing clearly indicate that accurate descriptions and quantifications of the less understood factors are strongly needed to estimate their influence on the future climate.

1.2 Aerosols

Aerosols appear in the atmosphere either by direct emission from various sources (primary aerosols) or are formed in situ by gas to particle conversion (secondary aerosols) (e.g., Finlayson-Pitts and Pitts, 2000; Kulmala et al., 2004). The size distribution and the composition of aerosol particles can undergo strong changes by coagulation with other particles, by chemical reactions, by condensation, by evaporation, or by activation as cloud condensation (CCN) or ice nuclei (IN) (Seinfeld and Pandis, 1998). Thus, size distributions and especially compositions of aerosols are specific for different geographical regions and heights in the atmosphere.

Aerosols can exert a climate forcing in two different ways, namely by the direct and the indirect aerosol effect. The direct aerosol effect on climate is due to scattering and absorp-

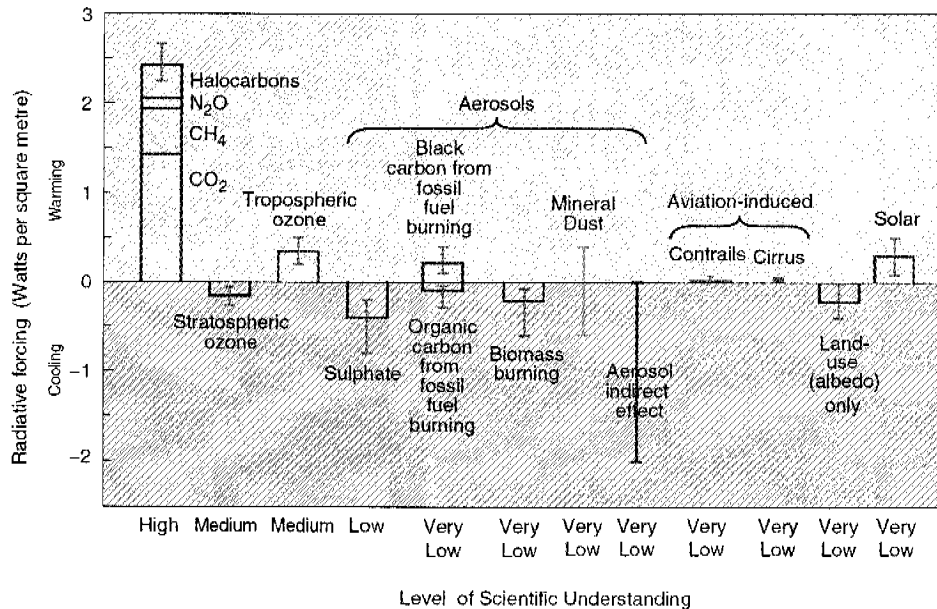


Figure 1.2: Anthropogenic forcing for several atmospheric factors for the year 2000 relative to 1750 (before industrial revolution). The heights of the bars represent best estimations of the contributions of these forcings, which can either result in warming or cooling. The vertical lines depict the uncertainty range for the different forcings. (Adapted from Houghton et al., 2001)

tion of sunlight by aerosols, which are mainly determined by the physical state, the radius, the absorption cross section and the chemical composition of the particles. Aerosols can take up or release water, which results in a large increase or decrease in radius, and consequently enhance or reduce the scattering intensity of the aerosol, respectively.

Aerosols exert also an indirect effect by acting as CCN for liquid or as IN for ice clouds, thereby affecting the initial cloud droplet number concentration, cloud lifetime and albedo. A higher number of CCN results in a higher droplet number, assuming a constant liquid water path (Twomey effect or first indirect aerosol effect), which consequently increases the optical depth of the liquid cloud. Such a reduction of the droplet size on the other hand reduces precipitation efficiency and thus increases cloud lifetime (second indirect effect) (Albrecht, 1989). The cooling from both indirect effects has been estimated by climate models for liquid clouds to be -1 to -4.4 Wm^{-2} in the global mean, but this estimate is still very poorly constrained (Lohmann and Lesins, 2002).

An increase in the number of ice crystals in cirrus clouds would also exert a Twomey effect in the same way as that for water clouds, namely an increase in ice particle number density of the cloud. But this effect is rather small when the ice particles are solely induced by homogeneous ice nucleation, because the number of ice crystals is rarely limited by the number of supercooled aerosol particles (Lohmann and Kärcher, 2002). But, an increase of IN could lead more preferably to heterogeneous ice nucleation, which may enlarge the size

of the ice crystals distinctly and thus reduce the radiative effect in the infrared compared to a cirrus cloud with a higher number density formed by homogeneous ice nucleation. However, Kärcher and Lohmann (2003) concluded, that the influence of only one type of IN immersed with a nucleation threshold of 1.3-1.4 in ice saturation is rather small. Since the indirect aerosol effect, especially for cirrus clouds, is so far not well understood and quantified, further investigations are strongly demanded (Lohmann and Feichter, 2005). The composition of the background aerosol in the upper troposphere (UT) consists mainly of an aqueous mixture of H_2SO_4 , NH_4HSO_4 , $(\text{NH}_4)_2\text{SO}_4$ and some other inorganic ions such as nitrates (Martin, 2000). These aerosols are assumed to be the precursors for homogeneously nucleated cirrus clouds. Besides this dominating inorganic fraction, Murphy et al. (1998) observed also a large amount of various organic compounds in single particle measurements. The authors concluded, that most organics were internally mixed with the inorganic fraction. From a modeling study, Kärcher and Koop (2005) concluded that a mixture of malonic and sulfuric acid particles nucleate at larger ice saturation ratio than pure sulfuric acid particles. This result is affirmed by observations during the CRYSYAL-FACE field campaign (Cirrus Regional Study of Tropical Anvils and Cirrus Layers-Florida Area Cirrus Experiment). It was found that ice particles contain a smaller organic fraction than the interstitial aerosols (Cziczo et al., 2004a). But, since organics may also act as IN, they can affect homogeneous as well as heterogeneous ice nucleation. So far, just a small fraction of the entire organic composition has been identified on the level of individual compounds (Kanakidou et al., 2005). Moreover, hardly any studies have analyzed the composition of UT organic aerosols. In a recent field campaign, Narukawa et al. (2003a) focused on dicarboxylic acids in the free troposphere and found that oxalic, malonic, adipic and azelaic acid were the major representatives of this substance class in all samples. Thus a better analysis of the organic composition in the UT together with their influence on ice particles formation is highly needed in future investigations.

1.3 Cirrus clouds and contrails

1.3.1 Cirrus clouds

Clouds are in general an accumulation of liquid and/or frozen water particles that are suspended in the atmosphere. The clouds are either formed on CCN in the case of liquid clouds or are nucleated out of supercooled liquid droplets or by IN in the case of ice clouds. According to international agreements, 10 types of main clouds are distinguished, depending on their occurrence and phase state: cirrus, cirrostratus, cirrocumulus, altocumulus, altostratus, nimbostratus, stratocumulus, stratus, cumulus, cumulonimbus (WMO, 1956). The first three cloud types consist exclusively of ice, whereas in some of the other clouds, liquid water or a mixture of water droplets with ice crystals is dominating. The World

Meteorological Organization (WMO) defines the three types of cirrus due to their optical attributes (see also Fig. 1.3):

- Cirrus appear as detached clouds in the form of white, delicate filaments or white or mostly white patches or narrow bands. These clouds have a fibrous (hair-like) appearance, or a silky sheen, or both (see Fig. 1.3a).
- Cirrostratus are transparent or whitish veil of fibrous (hair-like) clouds. Their smooth appearance covers totally or partially the sky, and often produce either partial or complete halo phenomena (see Fig. 1.3b).
- Cirrocumulus appear as a thin, white patch or layer of cloud without shading and are composed of very small elements in the form of grains or ripples. These clouds are merged or separated, and more or less regularly arranged and most of the elements have an apparent width of less than one degree (see Fig. 1.3c).

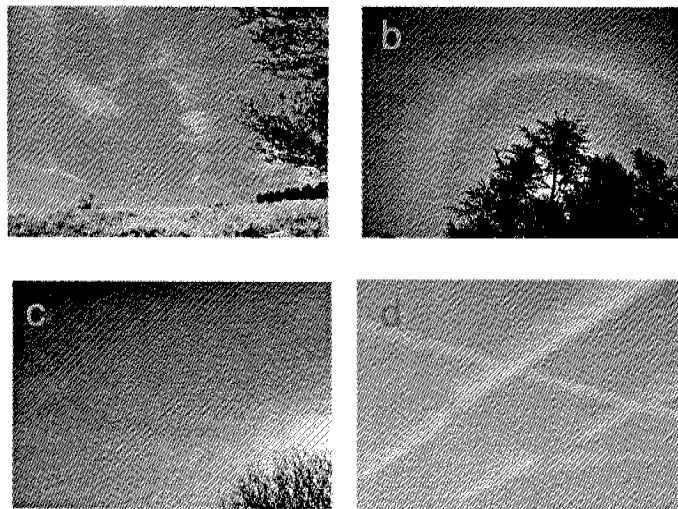


Figure 1.3: Photographs of the different types of cirrus clouds and contrails. Panel a: Cirrus, b: Cirrostratus, c: Cirrocumulus d: Contrails. (Photographs: www.metcoschweiz.ch)

Cirrus clouds cover more than 20% of the planet (Baker, 1997) and thus play an important role in determining the Earth's climate. Depending on height and region of appearance, the size of the ice particles, the ice number density, the optical depth (τ), the thickness and the horizontal distribution of the cirrus cloud can diverse. Ultra Thin Tropical Cirrus (UTTC), for example, have a typical ice crystal radius of $\sim 5 \mu\text{m}$ and ice number densities of $5\text{-}10 \text{ L}^{-1}$. Further, these clouds are optically thin ($\tau \approx 10^{-4}$) and have a small vertical thickness (200-300 m), but their horizontal extension can reach thousands of square kilometers (Luo et al., 2003). In comparison, cirrus clouds at lower altitudes are often

optically denser ($0.3 < \tau < 3.0$) and have a larger vertical thickness together with a smaller horizontal extension (Sassen, 2002). This short comparison points out clearly, that the microphysical properties of cirrus clouds can vary distinctly, which complicates the issue of cirrus clouds.

Since the technical development of instruments to measure cirrus cloud properties has largely improved in the last decades, they can be studied today by ground based monitoring (e.g., Lidar), satellite measurements (e.g., SAGE II) as well as by aircraft campaigns (e.g., SUCCESS, FIRE I and II, INCA, CRYSTAL-FACE). This development helps to get a better knowledge of the variety of cirrus clouds. Further, the obtained data can then be implemented in models, which deepen also the understanding of cirrus clouds and help to estimate their influence on the global climate. A survey of cirrus clouds is given in the book "Cirrus" by D. K. Lynch, K. Sassen, D. O'C. Starr and G. Stephens. Here, just one recent aircraft campaign is introduced shortly and one major conclusion is presented.

The INCA campaign (INterhemispheric differences in Cirrus properties from Anthropogenic emissions) took place in the year 2000. One major aim was to determine the differences in cirrus properties of air masses with low and high aerosol loadings, which are of importance for climate and ozone distribution in the UT and lower stratosphere. Therefore measurements were performed in the Northern and Southern Hemisphere (NH and SH) at similar latitudes and in the same seasonal period. Besides an extensive instrumentation on an aircraft, also ground based measurements were performed. One major finding of the campaign was, that the levels of pollution in the tropopause region of the NH and SH mid-latitudes are distinctly different, namely a higher aerosol pollution in the NH is present. Ström et al. (2003) pointed out, that cirrus clouds during the SH campaign formed preferentially at RHs between 140 and 155%, whereas clouds in the NH campaign formed at RHs somewhat below 130%, indicating a possible strong connection between the aerosol pollution and cirrus cloud formation. It seems likely that homogeneous ice nucleation is preferred in the cleaner air of the SH, whereas cirrus formation in the NH could mainly occur by heterogeneous ice nucleation. However, Haag et al. (2003) added, that the INCA data do not support the notion that ice crystals exclusively form on heterogeneous IN, stressing the paramount importance of homogeneous freezing in the formation of mid-latitude cirrus clouds, which is also claimed by Baker (1997). Despite several important improvements of the cirrus cloud understanding, the general question regarding the exact formation process still remains unresolved.

Besides the formation process of cirrus clouds, also their influence on the radiative forcing is a key issue in atmospheric sciences, which is again connected to their formation. Because of homogeneous ice nucleation results in a larger number of smaller ice particles than heterogeneous ice nucleation, the formation process of cirrus clouds affects obviously the radiative forcing (Zhang et al., 1999). The net radiative cloud forcing of a cirrus cloud is the sum of a solar albedo (UV or shortwave radiation) and greenhouse (IR or longwave radiation) effect (Schumann, 2002). A positive net forcing corresponds to a net heating

Earth's atmosphere. Since cirrus clouds have a lower temperature than surfaces the infrared radiation is emitted from (e.g., liquid clouds, Earth's surface), the IR contribution is positive. On the other hand, cirrus clouds increase Earth's albedo and thus have negative forcing in the UV range. Considering the sum of both effects, cirrus clouds at the top of the troposphere together with deep convective cloud anvils contribute to the warming of the Earth (see also Fig. 1.2), which is in contrast to clouds in the boundary layer (Baker, 1997).

1.3.2 Contrails

Contrails, made of ice particles, have been firstly observed in the beginning of the 20th century behind propeller driven aircrafts (see Fig. 1.3d; Schumann, 2002). Since contrails are also formed behind jet engines of aircrafts, they cover today a considerable fraction of the troposphere as a result of the large increase in global aircraft traffic. Measurements have shown, that saturation with respect to liquid water is required to form contrails. This means, that firstly a liquid cloud forms, which may freeze in the time period of ~ 0.1 s to ice (Jensen and Toon, 1997; Kärcher et al., 1998). The exact formation of contrail particles is a complex microphysical process, which is influenced by the ambient humidity, temperature and the amount of emitted ions, soot particles and sulfur content of the fuel and several other parameters (Yu and Turco, 1998).

However, aircraft exhaust may also lead indirectly to cirrus clouds by the transformation of persistent contrails into cirrus clouds. Ice supersaturated air is often free of visible cirrus clouds, because supersaturation is too small to nucleate ice particles. But persistent contrails may remain for hours and consequently can become a spreading cirrus cloud (Schumann, 2002). Further, contrail ice particles may also sediment and thus dehydrate the air or act as seeds and induce cloud formation at a lower level.

1.3.3 Ice particles in the lower troposphere

Ice particles in the lower troposphere are an important chain link for the formation of rain in the mid-latitudes. Nimbostratus and cumulonimbus often consist of a mixture of ice and supercooled liquid droplets (Schönwiese, 2003). At the same temperature, the vapor pressure over ice is smaller than that over supercooled water, and thus ice particles will grow at the expense of the water droplets, which is known as the Bergeron-Findeisen process. Once ice particles have reached a critical size, they will fall down and most of them will melt at lower altitudes and thus reach the Earth's surface as liquid droplets. Since temperature in such clouds are above the homogeneous freezing point of supercooled droplets, these ice particles will be formed by heterogeneous ice nucleation.

1.4 Ice nucleation in the atmosphere

As seen above, ice particles in the atmosphere can either form by homogeneous or heterogeneous ice nucleation. Homogeneous nucleation refers to the spontaneous and stochastic nucleation of ice from a supercooled liquid droplet in the absence of any foreign solid phase. On the other hand, heterogeneous ice nucleation occurs on surfaces, which lower the activation energy for the nucleation process. Figure 1.4 shows schematically the differences between homogeneous and heterogeneous ice nucleation. Let us consider a

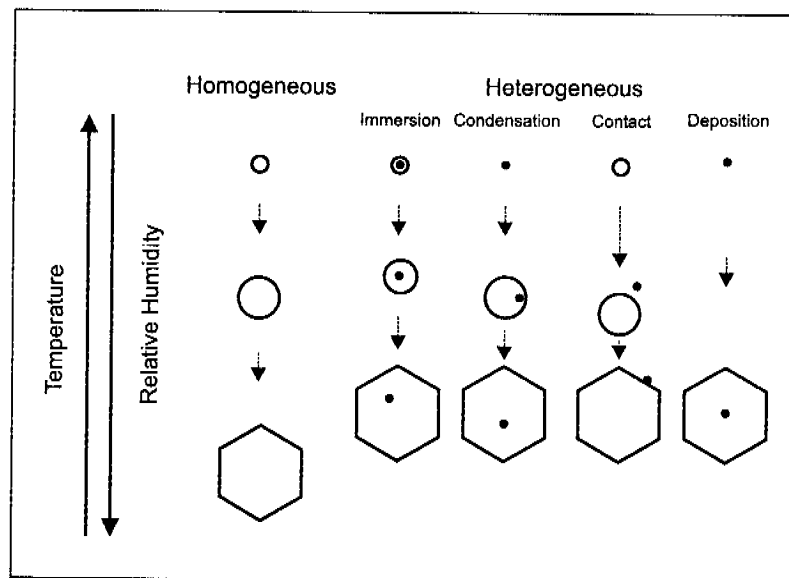


Figure 1.4: Scheme of the differences between homogeneous and heterogeneous ice nucleation. The black circles depict supercooled aqueous solution droplets, whereas the black points and the black hexagons illustrate the IN and the nucleated ice particles, respectively. The nucleation sequence for the different nucleation modes follows the black arrows from higher to lower temperatures.

liquid droplet without an ice nucleus that cools adiabatically in a rising air parcel (see left path in Fig. 1.4). While the relative humidity is increasing, the droplet takes up water, and consequently grows and becomes more dilute. The water uptake of the aerosol, and thus its size and concentration are determined by the partial pressure of water in the gas phase and the water vapor pressure of the droplet. At a certain relative humidity or supersaturation, the droplet will freeze homogeneously to ice. The freezing temperature depends on the droplet size and the water vapor pressure of the droplet (Koop et al., 2000).

If a solid insoluble ice nucleus is immersed in a liquid droplet, the droplet will also grow by water uptake while it is lifted up. But the ice nucleus lowers the required activation energy for the nucleation process, hence the droplet will freeze at a lower ice supersaturation

than in the homogeneous case (so called immersion mode, DeMott, 2002). A second pathway can be considered as follows. A solid particle can firstly reach water saturation, and hence form a liquid droplet. The droplet will then either immediately freeze upon activation or after further cooling (see also Section. 1.3.2). This pathway is called the condensation mode. An insoluble particle, e.g. mineral dust, can act as ice nucleus in two possible modes (two pathways on the right side of Fig. 1.4). Firstly, the solid particle can collide with a supercooled liquid droplet, initiating ice nucleation at the moment of contact. Secondly, at a certain relative humidity, an insoluble solid aerosol can adsorb water directly from the gas phase and the ice will be formed directly on the surface of the solid particle, the deposition mode.

In a recent review article on ice production in tropospheric clouds, Cantrell and Heymsfield (2005) claimed that mineral dust and soot are the most important IN in the UT. Based on PALMS measurement (Particle Analysis by Laser Mass Spectrometry), DeMott et al. (2003) concluded that ice particles formed by heterogeneous ice nucleation consist mainly of mineral dust or fly ash ($\sim 33\%$), metallic origin ($\sim 25\%$) and sulfate or organic compounds ($\sim 25\%$). In the CRYSTAL-FACE campaign, a large mineral dust layer originating from the Sahara at $\sim 1-5$ km was observed with a Polarization Diversity Lidar. It was found, that heterogeneous ice nucleation on the mineral dust was induced at temperatures up to 268 K in an altocumulus cloud (Sassen et al., 2003). Further measurements on the WB-57 on the same day indicate, that mineral dust was also the major ice nucleus in a cirrus cloud at ~ 12 km (Cziczo et al., 2004b). The mineral dust was transported by large updraft winds from the dust layer at lower altitudes to the cirrus cloud level. In the same cirrus cloud, also meteoritic material that sedimented down from the stratosphere was found in several analyzed ice residues. The authors concluded that $\sim 8\%$ of the ice crystals in this cloud have been nucleated on the stratospheric aerosol particles. Laboratory studies on immersed kaolinite and montmorillonite (Zuberi et al., 2002) and hematite and corundum (Hung et al., 2003) particles in aqueous $(\text{NH}_4)_2\text{SO}_4$ solutions have shown an increase in freezing temperature compared to homogeneous ice nucleation of ~ 10 and ~ 6 K, respectively. Archuleta et al. (2005) found that also Al_2O_3 , $3\text{Al}_2\text{O}_3 \cdot 2\text{SiO}_2$, and Fe_2O_3 in dilute H_2SO_4 solutions can act as heterogeneous IN. The field and laboratory studies together affirm the importance of mineral dust as an ice nucleus in the UT.

Some liquid $(\text{NH}_4)_2\text{SO}_4\text{-H}_2\text{SO}_4\text{-H}_2\text{O}$ particles in the UT may contain a solid core of crystallized salt (Tabazadeh and Toon, 1998), namely $(\text{NH}_4)_2\text{SO}_4$ and letovicite ($(\text{NH}_4)_3\text{H}(\text{SO}_4)_2$), whereas solid letovicite is more abundant than $(\text{NH}_4)_2\text{SO}_4$ in UT (Colberg et al., 2003). Zuberi et al. (2001) found that single $(\text{NH}_4)_2\text{SO}_4$ and letovicite crystals have just a weak ice nucleation efficiency. But, if atmospheric aerosols contain solid $(\text{NH}_4)_2\text{SO}_4$ in the form of micro-crystals, with the associated surface defects and higher surface area, they might function as efficient heterogeneous IN (Zuberi et al., 2001). Therefore it seems likely that $(\text{NH}_4)_2\text{SO}_4$ together with mineral dust are so far

the most common IN in the UT. Biogenic aerosols, e.g., leaf and pollen, can also have a good ice nucleation ability (Diehl et al., 2002). So far it remains unsolved whether such IN influence cirrus formation in the UT.

In the laboratory, the freezing ability of hundreds of organic IN, mostly in the deposition mode, have been tested (Fukuta, 1963; Parungo and Lodge Jr., 1965; Fukuta, 1966; Higuchi and Fukuta, 1966; Rosinski, 1980; Gavish et al., 1990). Rather surprisingly, several tested substances induce ice nucleation just below the ice melting point (e.g., metaldehyde freezes ice in the deposition mode at ~ 272 K). Therefore, together with the large uncertainty connected with the composition of the organic aerosol and their occurrence in the UT, organic IN have probably the potential to play a major role in heterogeneous ice nucleation in the UT.

1.5 Objectives of the thesis

Since the formation process of cirrus clouds and the resulting influence on the climate is still poorly understood, heterogeneous ice nucleation experiments of supercooled liquid droplets with immersed IN are performed in this thesis. This means, the ice nucleation ability of various IN (inorganic and organic ones) immersed in aqueous solutions is investigated with different experimental techniques. The results of the freezing point measurements are used to find a generalization of heterogeneous ice nucleation in the immersion mode. Further, model simulations are performed to estimate the change in microphysical and radiative properties of heterogeneously nucleated cirrus clouds when compared to cirrus clouds formed exclusively via homogeneous ice nucleation.

Seite Leer /
Blank leaf

Chapter 2

Theory

Since the historical work of Volmer and Weber (1926), many other contributors (e.g., Farkas, 1927; Becker and Döring, 1935; Zeldovich, 1942; Turnbull and Fisher, 1949) have improved and deepened the description of vapor to liquid or liquid to solid phase transitions. Today, in several textbooks (e.g., Seinfeld and Pandis, 1998; Pruppacher and Klett, 1997) these approaches are summarized as the classical nucleation theory (CNT), in which the change of the Gibbs free energy of such a phase transition is described. In the first two sections, the CNT for the homogeneous and heterogeneous ice nucleation is briefly presented. In Section 2.2, a recently published approach by Koop et al. (2000) for homogeneous ice nucleation from supercooled liquid droplets is discussed. A statistical description of the ice nucleation process is given at the end of the chapter.

2.1 Classical nucleation theory

A liquid aerosol can be supercooled far below its equilibrium melting point before it freezes to ice either by homogeneous or heterogeneous nucleation (Seinfeld and Pandis, 1998; Pruppacher and Klett, 1997). Homogeneous nucleation refers to the spontaneous and stochastic nucleation of ice in supercooled liquid droplets in absence of any foreign substrate. In the other case, nucleation occurs at an additional surface of so called ice nuclei (IN). Both processes describe a first order phase transition with the same physical concepts behind them.

2.1.1 Homogeneous ice nucleation

The first step in a liquid to solid phase transition is the formation of small molecular clusters inside the liquid phase, which are formed due to small fluctuations in the liquid. Once the size of such a cluster exceeds a critical value, it starts spontaneously to form

a cluster of macroscopic size, and hence nucleation starts. The change of the Gibbs free energy of a cluster consisting of i molecules can be described by,

$$\Delta G_i(T) = [\mu_{\text{sol}}(T) - \mu_{\text{liq}}(T)] \cdot i + 4\pi r_i^2 \sigma_{\text{sl}}(T), \quad (2.1)$$

where $\mu_{\text{sol}}(T)$ and $\mu_{\text{liq}}(T)$ are the chemical potentials of the solid and the liquid phase, respectively, T is the absolute temperature in Kelvin, r_i is the radius of the molecular cluster and $\sigma_{\text{sl}}(T)$ is the interfacial tension between the solid and the liquid phase. The first term in Eq. 2.1 describes the energy change for the transfer of molecules from the liquid to the solid cluster and the second one takes into account the formation of a new interface. It is important to note, that in the CNT it is assumed that clusters of a small number of molecules have the same interfacial tension as the bulk liquid. This major assumption of the CNT is often called the capillarity approximation, and poses a weakness of the entire theory. The difference of the chemical potentials can be expressed as,

$$\mu_{\text{sol}}(T) - \mu_{\text{liq}}(T) = -kT \ln \left(\frac{p_{\text{H}_2\text{O}}(T)}{p_{\text{ice}}(T)} \right), \quad (2.2)$$

where k is the Boltzmann constant, $p_{\text{H}_2\text{O}}$ and p_{ice} are the vapor pressures of supercooled water and ice at the same temperature, respectively. This ratio is often defined as the saturation ratio $S(T)$. The number of molecules in the cluster, i , can be expressed as,

$$i = \frac{4\pi r_i^3}{3v_{\text{ice}}(T)}, \quad (2.3)$$

where $v_{\text{ice}}(T)$ is the molecular volume of ice.

Inserting Eq. 2.2 and Eq. 2.3 into Eq. 2.1 leads to,

$$\Delta G_i(T) = -\frac{4\pi r_i^3}{3v_{\text{ice}}(T)} kT \ln S(T) + 4\pi r_i^2 \sigma_{\text{sl}}(T). \quad (2.4)$$

The second law of thermodynamics states, that for $\Delta G \geq 0$ a process does not occur. If $\Delta G \leq 0$, a process can start spontaneously, whereby often a activation energy is required. Since, the second term in Eq. 2.4 is positive at all times, the first one discriminates whether $\Delta G \geq 0$, and thus a molecular cluster will be formed or not. Obviously, for $S < 1$, the first term is also positive, which leads to a monotonous increase of ΔG_i (Fig. 2.1) and hence the nucleation process will never start. On the other hand, if $S > 1$, Eq. 2.1 contains both positive and negative contributions. For small r_i , the increase in Gibbs free energy due to the second term is larger than the decrease because of the formation of a solid phase. The critical radius size of the molecular cluster (r_{hom}) for homogeneous ice nucleation can be determined by setting $\partial \Delta G_i / \partial r = 0$,

$$r_{\text{hom}}(T) = \frac{2\sigma_{\text{sl}}(T)v_{\text{ice}}(T)}{kT \ln S(T)}, \quad (2.5)$$

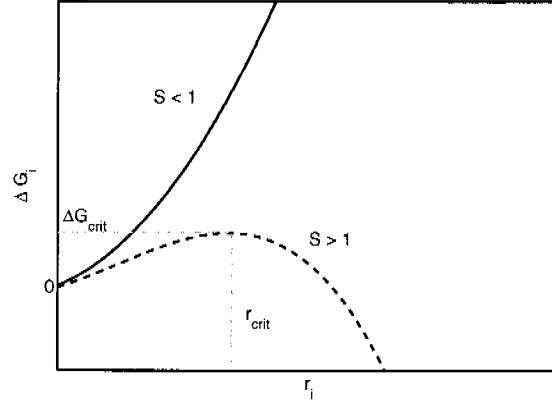


Figure 2.1: The Gibbs free energy (ΔG_i) as a function of the radius of the molecular cluster. Solid line: $S < 1$. Therefore ΔG_i is monotonously increasing. Dashed line: $S > 1$. After ΔG_i reaches a maximum at r_{hom} , the nucleation process starts spontaneously.

With Eq. 2.5, also a critical Gibbs free energy value for homogeneous ice nucleation can be obtained as,

$$\Delta G_{\text{hom}}(T) = \frac{16\pi\sigma_{\text{sl}}^3(T)v_{\text{ice}}^2(T)}{3[kT \ln S(T)]^2}. \quad (2.6)$$

The equilibrium number of critical molecular clusters (n_{eq}) formed in the liquid phase per unit of volume is given by the Boltzmann distribution,

$$n_{\text{eq}}(T) = n_v \exp\left(-\frac{\Delta G_{\text{hom}}(T)}{kT}\right), \quad (2.7)$$

where n_v is the number density of water molecules in the volume, with a typical value of $3.1 \cdot 10^{22} \text{ cm}^{-3}$.

Until now, only the formation of a critical cluster has been considered. Nevertheless, the formation of critical clusters is also limited through the diffusion energy (ΔF_{diff}) across the water/ice interface. The flux of water molecules to the ice embryo per unit time (F) can be expressed as,

$$F(T) = \frac{kT}{h} \exp\left(-\frac{\Delta F_{\text{diff}}(T)}{kT}\right), \quad (2.8)$$

whereby h is Planck's constant. The product of the last two equations leads now to the homogeneous ice nucleation rate coefficient per unit time and unit volume,

$$j_{\text{hom}}(T) = \frac{kT}{h} \exp\left(-\frac{\Delta F_{\text{diff}}(T)}{kT}\right) \cdot n_v \exp\left(-\frac{\Delta G_{\text{hom}}(T)}{kT}\right). \quad (2.9)$$

From Eq. 2.9 the homogeneous nucleation rate, ω , can be derived as,

$$\omega_{\text{hom}}(T) = j_{\text{hom}}(T) \cdot V_{\text{sample}}, \quad (2.10)$$

where V_{sample} is the volume of the investigated sample. So far, a theoretical description for the homogeneous rate has been presented, but several parameters, namely σ_{sl} , v_{ice} , S and ΔF_{diff} , depend on temperature. Measurements in the supercooled regime for σ_{sl} and ΔF_{diff} do not exist, and hence parameterizations are needed to express the temperature dependence. The other two parameters can be described by well known other variables. In the next part, parameterizations of these parameters are presented for pure water. The diffusion activity energy per molecule is defined as (Atkins, 1996),

$$\Delta F_{\text{diff}}(T) = \frac{\partial \ln D}{\partial \ln \frac{1}{T}} \cdot k, \quad (2.11)$$

where D is the diffusivity, which can be expressed by the Vogel-Fulcher-Tammann equation (Smith and Kay, 1999):

$$D(T) = D_0 \exp\left(\frac{E}{T - T_0}\right). \quad (2.12)$$

Thus, Eq. 2.11 leads to,

$$\Delta F_{\text{diff}}(T) = \frac{kT^2 \cdot E}{(T - T_0)^2}, \quad (2.13)$$

where E and T_0 are 892 K and 118 K, respectively (Smith and Kay, 1999). This parameterization is valid in the temperature range between 150 and 273 K.

As mentioned before, $S(T)$ is defined as the ratio between the vapor pressure of supercooled liquid water and the vapor pressure of ice at the same temperature. Over the years, several parameterizations have been published for both variables (Murphy and Koop, 2005). Here, the vapor pressure over ice, $p_{\text{ice}}(T)$ [hPa], is expressed as,

$$p_{\text{ice}}(T) = 5.752 \cdot 10^{10} \cdot \exp\left(-20.947 \cdot T_{\text{m}}^0/T - 3.56654 \cdot \ln(T_{\text{m}}^0/T) - 2.01889 \cdot T/T_{\text{m}}^0\right) \quad (2.14)$$

T_{m}^0 is the melting point of pure water in Kelvin and the parameterization is valid in the range between 150 and 273 K. According to Koop et al. (2000), $p_{\text{H}_2\text{O}}(T)$ [hPa] can be described as,

$$p_{\text{H}_2\text{O}}(T) \approx p_{\text{ice}}(T) \cdot \exp\left(-\frac{210368 + 131.438 \cdot T - 3.32373 \cdot 10^6/T - 41729.1 \cdot \ln T}{RT}\right) \quad (2.15)$$

with a validity range of $150 < T < 273$ K.

v_{ice} can be parameterized as,

$$v_{\text{ice}}(T) = \frac{1}{N_{\text{a}}} \cdot \left[\left(\frac{M_w}{\rho_0} \right)^{1/3} \cdot \left(1 + 10^{-6} \cdot (14892.96 \cdot dt + 7461.1 \cdot dt^2 - 2266.3 \cdot dt^3) \right) \right]^3 \quad (2.16)$$

where N_a is the Avogadro number, M_w is the molar mass of water ($=18.0148 \text{ gmol}^{-1}$), ρ_0 is the density of ice at T_m^0 ($=0.91661 \text{ gcm}^{-3}$, Hobbs, 1974) and dt is equal to $\frac{T-T_m^0}{T_m^0}$.

σ_{sl} is poorly quantified in the supercooled region for two reasons. Firstly, the macroscopic interface energy between water and bulk ice is so far not measured in the supercooled regime. And secondly, since the ice embryo can be smaller than 1 nm in radius, σ_{sl} may also differ from the macroscopic interface energy. Therefore, this quantity was derived by fitting measurements of the homogeneous ice nucleation rate of Pruppacher and Klett (1997), Krämer et al. (1999), Duft and Leisner (2004), Benz et al. (2005), Stöckel et al. (2005), Kabath et al. (2006) and own measurements using Eq. 2.9. This leads consequently for $\sigma_{sl}(T)$ [Jcm^{-2}] to:

$$\sigma_{sl}(T) = 3.298 \cdot 10^{-6} + 1.2048 \cdot 10^{-6} \cdot dt - 4.6705 \cdot 10^{-5} \cdot dt^2. \quad (2.17)$$

This fit function was derived in the temperature range of $210 \leq T \leq 245 \text{ K}$. Since an extrapolation is in good agreement with the measurement of σ_{sl} at T_m^0 by Hobbs (1974), one is able to apply this parameterization up to T_m^0 .

So far, the homogeneous nucleation rate is fully described, and in the next paragraph, the major differences of the heterogeneous rate coefficient are presented.

2.1.2 Heterogeneous ice nucleation

The heterogeneous ice nucleation on insoluble particles may take place at much lower supersaturation than homogeneous nucleation. Hence this process can take an important role in the atmosphere. As mentioned in the introduction, four different types of the heterogeneous nucleation have to be distinguished. Since within this thesis only experiments in the immersion mode are performed, the following theoretical section is focused on the description of the heterogeneous nucleation from supercooled droplets with an immersed ice nucleus. Nevertheless, the classical theory for the heterogeneous ice nucleation starts independently of the various modes of freezing.

The additional surface of the ice nucleus leads to a reduction of the Gibbs free energy for the nucleation by,

$$\Delta G_{\text{het}}(T) = \Delta G_{\text{hom}}(T)f(\alpha) \quad (2.18)$$

where $f(\alpha)$ is a reduction factor, which is given by Seinfeld and Pandis (1998) as,

$$f(\alpha) = \frac{1}{4}(2 + \cos \alpha)(1 - \cos \alpha)^2. \quad (2.19)$$

The cosine of the contact angle α between the nucleus, the liquid and the ice can be described as,

$$\cos \alpha = \frac{\sigma_{\text{liquid/nucleus}} - \sigma_{\text{ice/nucleus}}}{\sigma_{\text{liquid/ice}}}, \quad (2.20)$$

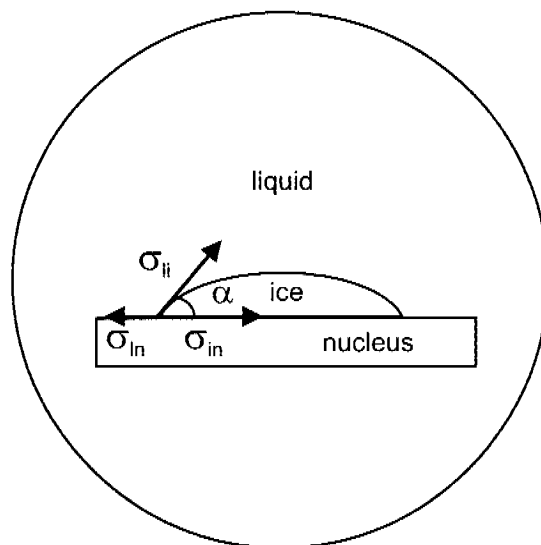


Figure 2.2: The contact angle (α) of an ice nucleus immersed in a liquid droplet determined by the interfacial tensions (σ). The labels l , i and n denote liquid, ice and nucleus, respectively.

where the σ 's are the interfacial tensions between the different partners (See Fig. 2.2). The function $f(\alpha)$ assumes values between 0 and 1. Consequently α has to lie in the range of 0 to 180°, whereas for $\alpha=180^\circ$ the heterogeneous nucleation is no longer favored over the homogeneous nucleation and for $\alpha=0^\circ$ nucleation starts as soon as supersaturation is reached.

The heterogeneous nucleation rate coefficient for supercooled liquid droplets with an immersed ice nucleus, $j_{\text{het}}(T)$, can be described similar to the homogeneous case as (Pruppacher and Klett, 1997):

$$j_{\text{het}}(T) = \frac{kT}{h} \exp\left(-\frac{\Delta F_{\text{diff}}(T)}{kT}\right) \cdot n_s \exp\left(-\frac{\Delta G_{\text{het}}(T)}{kT}\right), \quad (2.21)$$

where n_s ($\approx 10^{15} \text{cm}^{-2}$) is the number density of water molecules at the nucleus/water interface. Thus the heterogeneous rate is,

$$\omega_{\text{het}}(T) = j_{\text{het}}(T) \cdot S_{\text{IN}}, \quad (2.22)$$

where S_{IN} is the total surface of the ice nucleus. Atmospheric IN can exhibit a complex morphology and an inhomogeneous structure (e.g., soot). Therefore S_{IN} has to be estimated with possibly large uncertainties.

Obviously, only the Gibbs free energy has to be adjusted for the heterogeneous rate coefficient, and, n_s has to replace n_v , which indicates that heterogeneous ice nucleation is a surface dominated process. So far, the contact angle remains as the only unknown variable for $j_{\text{het}}(T)$.

2.2 Water activity based ice nucleation theory

In a recent study, Koop et al. (2000) described a new thermodynamical model for homogeneous ice nucleation of supercooled aqueous solutions. Considering an extensive set of experimental data, the authors concluded that homogeneous ice nucleation depends not on the nature of a solute, but solely on the water activity, a_w , of the solution, which is defined as,

$$a_w(T, c) = \frac{p_{\text{sol}}(T, c)}{p_{\text{H}_2\text{O}}(T)}, \quad (2.23)$$

where c is the concentration of the solution, and $p_{\text{sol}}(T, c)$ and $p_{\text{H}_2\text{O}}(T)$ are the vapor pressures of the solution and of pure water at the same temperature, respectively. At the ice melting point, the aqueous solution and the ice are in equilibrium and hence their vapor pressures are equal.

$$p_{\text{sol}}(T_m) = p_{\text{ice}}(T_m). \quad (2.24)$$

This results to the water activity at the ice melting point for any solution:

$$a_w(T_m) = \frac{p_{\text{ice}}(T_m)}{p_{\text{H}_2\text{O}}(T_m)}. \quad (2.25)$$

In the previous section, parameterizations for the vapor pressure of ice and supercooled water have been derived (Eq. 2.14 and Eq. 2.15), and thus the water activity at the ice melting point leads to:

$$a_w(T_m) = \exp\left(\frac{210368 + 131.438 \cdot T_m - 3.32373 \cdot 10^6/T_m - 41729.1 \cdot \ln T_m}{RT_m}\right). \quad (2.26)$$

Here, T_m denotes the ice melting point of the aqueous solution in Kelvin. So far, a simple parameterization has been derived to calculate the water activity at the ice melting point independent of the nature of the solute. At the ice freezing point, on the other hand, the above mentioned equilibrium conditions (Eq. 2.24) are no longer fulfilled. Furthermore no measurements of the water activity are available in the supercooled regime. However, Koop et al. (2000) found that the water activity for a series of solutions show just a slight temperature dependence above the ice melting point. If this trend is extrapolated below the ice melting point, the water activity at the freezing point, $a_w(T_f)$ can be estimated as,

$$a_w(T_f) = a_w(T_m). \quad (2.27)$$

Figure 2.3 shows the freezing points of micrometer sized droplets of aqueous solutions with 18 different solutes as a function of a_w , whereby the water activity at the freezing points is determined with the measured melting points and Eqs. 2.26 and 2.27. The solid

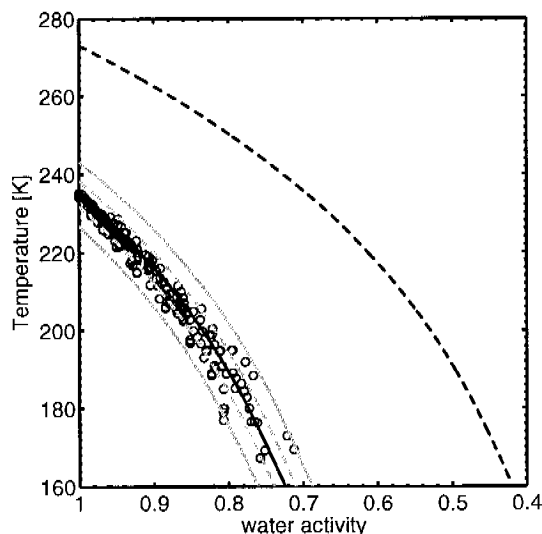


Figure 2.3: *Bullets: Homogeneous ice freezing points of micrometer sized droplets of aqueous solutions with 18 different solutes as a function of a_w (Koop et al., 2000). The dashed black line is the ice melting point curve. The solid black curve is the melting point curve horizontally shifted by a constant $\Delta a_w = 0.305$. The grey dashed and solid lines indicate a ± 2 and 5% deviation of the black solid curve, respectively. (Courtesy of Koop, 2004)*

black curve depicts the ice melting point curve horizontally shifted by a constant offset $\Delta a_w = 0.305$. Since this number is only valid for the homogeneous ice nucleation, it will from now on be denoted as $\Delta a_{w,\text{hom}}$.

The major uncertainty of this theory is the assumption of equal water activities at the ice melting and ice freezing point for a given concentration. The thin curves in Fig. 2.3 depicts clearly, that the assumption is valid for all of the investigated substances within an error of 5%. Koop (2004) used a simple model to describe the possible temperature dependence of the water activity. From the simulations, the author concluded that the observed spread in the data of Fig. 2.3 is very likely due to the fact, that water activities may slightly increase as well as decrease with decreasing temperature. Because no measurements in the supercooled region exist, the above assumption of a constant water activity is applied. If a supercooled liquid aerosol particle in the atmosphere is at a certain temperature in equilibrium with the gas phase, i.e., $p_{\text{sol}}(T) = p_{\text{gas}}(T)$, the water activity is equal to the relative humidity (RH):

$$a_w(T) \stackrel{\text{def}}{=} \frac{p_{\text{sol}}(T)}{p_{\text{H}_2\text{O}}(T)} \stackrel{\text{equil.}}{=} \frac{p_{\text{gas}}(T)}{p_{\text{H}_2\text{O}}(T)} \stackrel{\text{def}}{=} RH(T). \quad (2.28)$$

Note, that the Kelvin effect has been neglected, but it becomes only important for particles with diameters smaller than $0.1 \mu\text{m}$. So, the water activity based theory can predict the

homogeneous ice freezing temperature of any given liquid aerosol particle based on the relative humidity of an air parcel. It is important to note, that $\Delta a_{w,\text{hom}}=0.305$ is valid for one homogeneous ice nucleation rate coefficient, namely $j_{\text{hom}} \approx 10^{10} \text{ cm}^{-3}\text{s}^{-1}$. For others Δa_w , j_{hom} can be calculated as:

$$\log j_{\text{hom}} = -906.7 + 8502 \cdot \Delta a_w - 26924 \cdot \Delta a_w^2 + 29180 \cdot \Delta a_w^3. \quad (2.29)$$

This equation is valid for $0.26 < \Delta a_w < 0.34$.

2.3 Statistical description of the ice nucleation process

It was shown in Section 2.1 that an ice embryo has to exceed a critical size inside a liquid before the nucleation process takes place. The formation of this critical embryo, and therefore the nucleation event, is independent of any previous nucleation attempts. It was shown in a previous work, that the poisson statistics can be used to treat the stochastic freezing probability of single freezing experiments (Koop et al., 1997).

The formula of Bernoulli or the binomial distribution describes the frequency, $P_m(n)$, of m successful nucleation events with the probability p , in a sequence of n independent nucleation attempts (Taubenheim, 1969).

$$P_m(n) = \binom{n}{m} p^m (1-p)^{n-m} \quad (2.30)$$

In this formula n and m are integers. For $p=0.5$, the binomial distribution is symmetric around the value $m=n/2$, and in all other cases a asymmetric distribution results. Since every water molecule in the sample can be the core of a critical ice embryo, n can be treated as the total number of molecules in the sample.

So far, the frequency of successful attempts is independent of time. The question, what is the probability that an event occurs umpteen times in a specific time interval, t , leads to the Poisson formula of unfrequent events in a specific time interval,

$$P_m(t) = \frac{\lambda^m}{m!} e^{-\lambda}, \quad (2.31)$$

where $\lambda = n \cdot p$ is the mean value of events in the time interval t . Although p goes to zero, the product of $n \cdot p$ results in a finite number (Taubenheim, 1969).

Now, the mean nucleation rate, ω , of the entire sample can be introduced as,

$$\omega = \frac{\lambda}{t}. \quad (2.32)$$

Thus Eq. 2.31 can be rewritten as:

$$P_m(t) = \frac{(\omega t)^m}{m!} e^{-\omega t}. \quad (2.33)$$

This equation indicates the probability of observing m nucleation events in the time interval $[0, t]$. For $m=0$, the first factor in Eq. 2.33 goes to unity and thus results in exponential decline, similar to the radioactive decay.

In the case of a series of independent samples, Eq. 2.33 can be treated as (Koop et al., 1997),

$$P_m(t) = \frac{(\omega t)^m}{m!} e^{-\omega t} \simeq \frac{n_{\text{liq}}(t)}{n_{\text{tot}} m!} (\ln \{ \frac{n_{\text{tot}}}{n_{\text{liq}}(t)} \})^m \quad (2.34)$$

where ω is the mean nucleation rate in the time interval, n_{liq} and n_{tot} are the samples still liquid after the time interval t and the total number of samples, respectively. The approximation in Eq. 2.34 becomes more accurate with increasing n_{tot} , but is already valid for $n_{\text{tot}} \geq 5$. One has to consider, that ω depends on parameters such as temperature and size of the sample.

Introducing the total observation time t_{tot} ,

$$t_{\text{tot}} = \sum_{i=0}^{n_{\text{liq}}} t_{\text{liq},i} + \sum_{i=0}^{n_{\text{nuc}}} t_{\text{nuc},i}, \quad (2.35)$$

where $t_{\text{liq},i}$ and $t_{\text{nuc},i}$ are the times of particles being liquid or solid in the bin i , respectively. The nucleation rate, ω , can be derived with

$$\begin{aligned} n_{\text{nuc}} &= \sum_{m=0}^{\infty} m P_m(t_{\text{tot}}) = \sum_{m=1}^{\infty} m \frac{(\omega t_{\text{tot}})^m}{m!} e^{-\omega t_{\text{tot}}} \\ &= \omega t_{\text{tot}} \sum_{m=1}^{\infty} \frac{(\omega t_{\text{tot}})^{m-1}}{(m-1)!} e^{-\omega t_{\text{tot}}} = \omega t_{\text{tot}} \sum_{m'=0}^{\infty} \frac{(\omega t_{\text{tot}})^{m'}}{(m')!} e^{-\omega t_{\text{tot}}} \\ &= t_{\text{tot}} \sum_{m'=0}^{\infty} P_{m'}(t_{\text{tot}}) \\ &= \omega t_{\text{tot}} \end{aligned} \quad (2.36)$$

where $m' = m - 1$ and the normalization $\sum_{m'=0}^{\infty} P_{m'}(t_{\text{tot}}) = 1$ is used.

This leads to the nucleation rate

$$\omega = \frac{n_{\text{nuc}}}{t_{\text{tot}}}. \quad (2.37)$$

Dividing Eq. 2.37 by either the volume of the sample, V_{sample} , or the surface of the IN, S_{IN} , leads to the homogeneous or heterogeneous nucleation rate coefficient, respectively.

$$j_{\text{hom}} = \frac{\omega}{V_{\text{sample}}} \quad \text{or} \quad j_{\text{het}} = \frac{\omega}{S_{\text{IN}}}. \quad (2.38)$$

Thus the theoretically derived equations for the homogeneous (Eqs. 2.9 and 2.29) and for the heterogeneous (Eq. 2.21) rate coefficients can be compared with statistical analysis of single droplet measurements.

Seite Leer /
Blank leaf

Chapter 3

Experimental

Calorimetric and optical techniques are two approaches to investigate the freezing and melting of aqueous solution droplets. In this work three different setups are used, in such a way that the radius of the droplets and the experimental temperature range can be varied between 2 μm to 1 mm and from 150 to 273 K, respectively.

3.1 Differential scanning calorimetry

Differential scanning calorimetry is a thermo-analytical technique in which the difference of required heat to increase or decrease the temperature of a sample and a reference is measured as a function of time or temperature (Hemminger and Cammenga, 1989). The sample and reference pans are both kept throughout the experiment at nearly the same temperature. Usually, the cell with the sample and the reference are cooled or heated at constant cooling rate. Therefore, while the two pans are in a thermodynamic equilibrium, i.e., no chemical or physical reaction happens, the measured heat flow difference is always zero. When for example a melting process occurs in the sample, the heat flow to the sample must be consequently increased to keep the same temperature as in the reference sample. Thus, by observing this difference in heat flow as a function of time or temperature, the total amount of absorbed or released energy during such a transition can be measured. Further the phase transition temperature (e.g. melting or freezing point of ice) can be determined. The differential scanning calorimetry technique may also be used to observe more subtle phase changes, such as glass transitions.

Here, a commercial Differential scanning calorimeter (DSC, TA Q10) with a LNCS cooling system is used. This setup allows to measure the temperature in the range of 130 to 600 K, with a precision of ± 0.01 K. The cooling and heating rates can be adjusted between 0.01 and 50 Kmin^{-1} . The DSC pan can be charged with bulk or emulsified samples. An empty DSC pan is always used as the reference sample.

3.1.1 Emulsion calorimetry

Samples of aqueous solutions are often contaminated by dust or other particles, which may induce heterogeneous ice nucleation at higher temperature than in the homogeneous case. The large volume of a bulk sample enhances the probability, that a sample contains a higher number of such ice nuclei. To overcome this problem, the volume of the sample can be reduced to the volume of a micrometer sized droplet (Fig. 3.1). On the other hand,

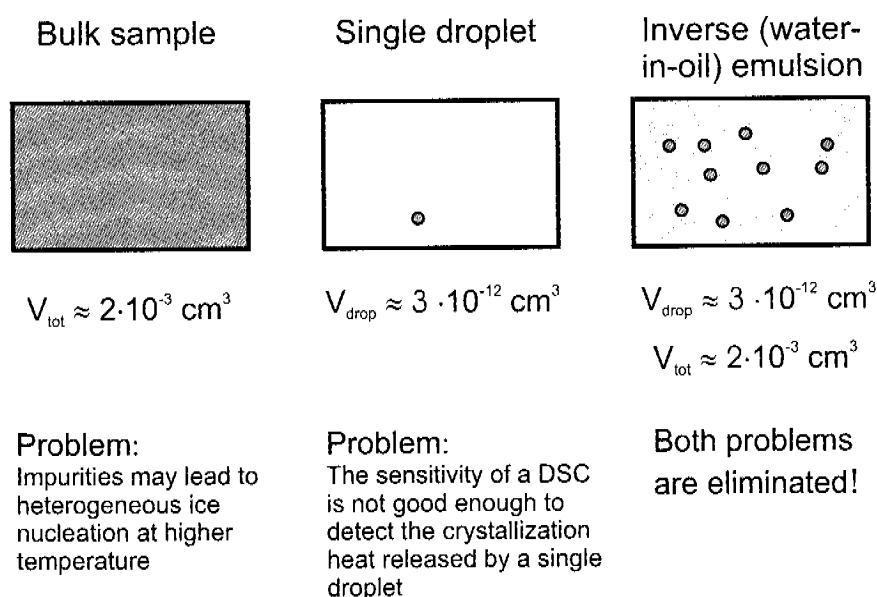


Figure 3.1: Schematic sketch of the emulsion calorimetry.

the crystallization heat of such a droplet is smaller than the detection limit of a regular DSC. But the sum of the crystallization heats of a large number of micrometer sized droplets is large enough to be detected by a DSC. Such a situation is realized in inverse (water-in-oil) emulsions, which contain two immiscible substances, usually a hydrophobic and a hydrophilic substance, combined with an emulsifier. Since an emulsion consists of a large number of droplets, one can be ensured that just a small fraction of the droplets will contain unintentionally an ice nucleus. Therefore, emulsion calorimetry allows to investigate homogeneous ice nucleation. However, the droplets can also be seeded by a specific ice nucleus, and hence emulsions are also a potent tool to observe heterogeneous ice nucleation.

3.1.2 Emulsion preparation

A procedure to produce almost mono disperse inverse emulsions with a mean radius of $3 \pm 2 \mu\text{m}$ was developed and applied in a previous work (Zobrist, 2001). The emulsions were made by adding 0.8 ml of a 23 wt% lanolin/mineral oil solution to 0.2 ml of an aqueous solutions (made with distilled and deionized water, 18.2 M Ω). The samples were emulsified by applying a commercial drilling machine for 15 minutes. Lanolin, a natural product obtained from the fleccc of sheep, is the emulsifier. Approximately 25 mg of the prepared emulsion is used for a DSC run, which corresponds to $\sim 10^7$ droplets. Figure 3.2 shows a picture of an emulsion taken with 100 times magnification. Throughout the entire thesis, this procedure was used to make the emulsions.

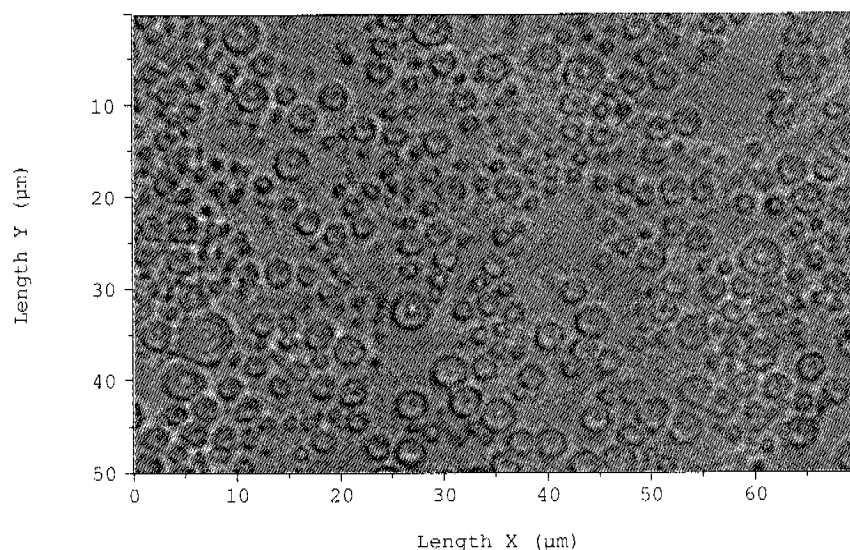


Figure 3.2: Photograph of an emulsion taken with 100 times magnification. The black circles depict the aqueous droplets in the oil matrix.

3.1.3 Typical DSC experiment

Figure 3.3 shows the raw data for a cooling and heating curve of a typical experiment with an emulsion made of a 9.9 wt% NaCl solution. The sample is cooled with a constant cooling rate (10 Kmin^{-1}) and a large exothermic peak appears at about 220 K, which is assigned to freezing of the water in the emulsion. The ice freezing point of the sample is determined by the onset of the peak (marked by the black lines). In the heating cycle (rate = 1 Kmin^{-1}) two endothermic peaks appear, a larger one at about 250 K and a smaller one close to 270 K. The first one is due to the eutectic melting of the $\text{NaCl} \cdot 2\text{H}_2\text{O}$

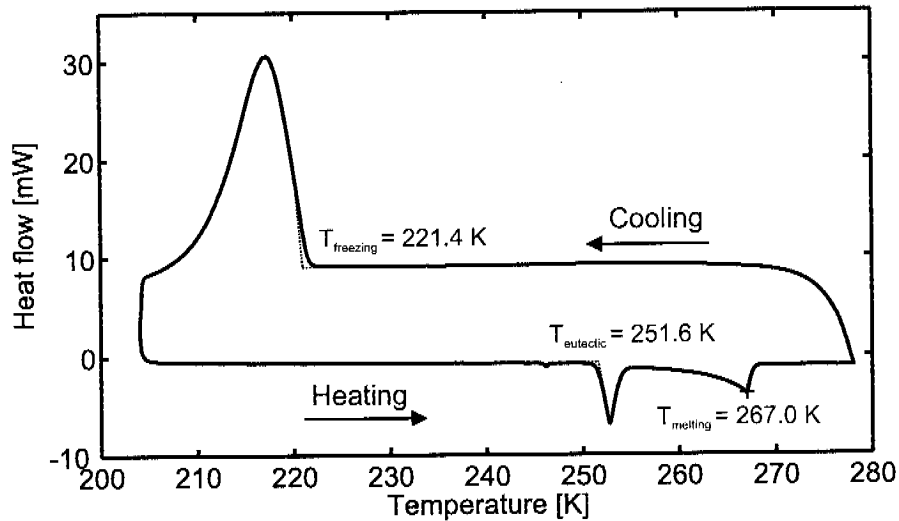


Figure 3.3: DSC cooling and heating curves for a typical experiment with an emulsion made of a 9.9 wt% NaCl solution. The black arrows indicate the running direction of the experiment. T_{freezing} , T_{eutectic} and T_{melting} denote the ice freezing, the eutectic melting and the ice melting point of the sample, respectively. The first two are determined with the onset of the peak, whereas the latter one is obtained at the minimum of the curve (black cross).

(Linke, 1958). The eutectic melting point temperature is defined by the onset of the peak (again marked by the black lines). The smaller peak at higher temperature presents the ice melting point of the aqueous solution. The two melting processes are examined more in detail in Fig. 3.4. In the binary NaCl/water phase diagram, four different regions can be distinguished, with ice, crystalline $\text{NaCl}\cdot 2\text{H}_2\text{O}$ and an aqueous NaCl solution as possible components. After the heating cycle of the emulsion is started, the heat flow curve (right panel) remains almost constant until the temperature reaches the eutectic melting point line (red dashed line in the right panel). At this temperature, the eutectic melting of the mixture leads to a strong endothermic peak. There, the ice is in equilibrium with a solution of the eutectic concentration (black circle in the left panel of Fig. 3.4). Since the initial concentration of the solution is lower than the eutectic concentration, the sample follows the red solid line on the left side of the eutectic melting point to higher temperatures, until it reaches the final melting temperature (large black cross). After the large melting peak, $\text{NaCl}\cdot 2\text{H}_2\text{O}$ and a part of the ice the endothermic signal is rising again due to the further melting of the ice until it peaks when the ice is completely melted and consists solely of an aqueous NaCl solution. The left panel of Fig. 3.4 shows clearly, that these melting process results in different shapes of the peaks in the DSC heating curves. Therefore, individual temperature calibrations are needed for both processes (Appendix A.1). Note that all the peaks, also the freezing peak in Fig. 3.3, depend strongly on cooling or heating rate,

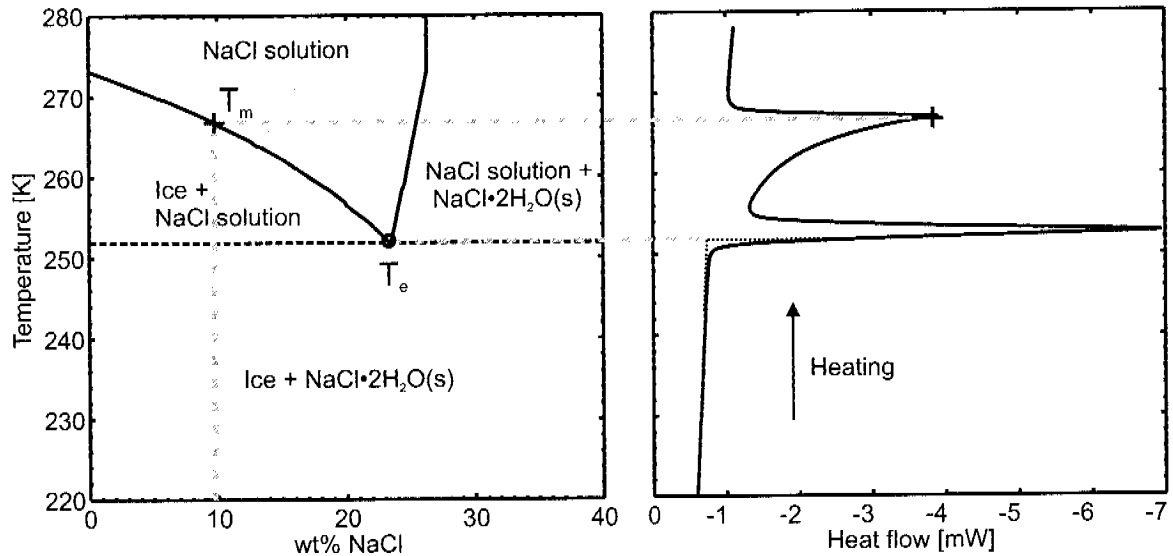


Figure 3.4: Phase diagram of the binary NaCl/water system (left panel, Linke, 1958) together with a heating curve of an emulsion made of a 9.9 wt% NaCl solution (right panel). (see text for details)

namely, a larger rate leads to broader peak. This phenomenon has also been considered for the temperature calibrations.

3.2 Single droplets cooling stage

A large part of this thesis was devoted to the construction up of a cooling stage, which allows to measure optically the freezing points of several single droplets simultaneously. With the measured freezing points, one has the possibility to obtain easily a statistical information on the nucleation process.

3.2.1 Experimental setup

Figure 3.5 depicts a schematic diagram of the entire setup, which consists of a cooling cell, a digital camera (C-Cam ccf15) with an external light source, a temperature controller (LTC-11) and a computer to control the experiment and to save the data. The entire setup is operated by a Labview user interface on the computer (Dobler, 2003), whereby the LTC-11 and the C-Cam are connected by a RS232 and a LVDS interface, respectively. The resolution of the digital camera is 512×512 pixel. An IR filter, made of small water tanks, is placed in front of the halogen lamps to avoid an uncontrolled heating of the cooling cell by the light source. The center of the entire setup is the cooling cell,

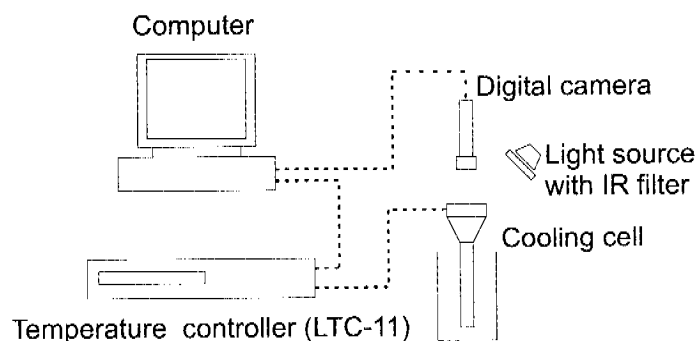


Figure 3.5: Schematic diagram of the entire experimental setup.

which is shown detailed in Fig. 3.6. The small cell inside the cooling cell consists of a hydrophobically coated glass substrate, on which up to 10 droplets are placed (see also the right panel of Fig. 3.6). The cell is sealed by a cap, which is made of an O-ring and glass plate stuck on. The small cell is placed on a large copper block, which is embedded and sealed by a flange. For optical detection, a glass window is inserted in the top of the flange. A large copper rod is placed in the liquid nitrogen. The flange and the rod are connected with a cylindrical aluminum piece. The temperature of the copper block is controlled by a combination of constant cooling by the liquid nitrogen and toward heating by a heating foil (Minco, HK 5561R37.4L12A), which is mounted below the copper block. A temperature sensor (Pt100) is attached to the copper block and connected with the LTC-11. This setup allows to control the temperature of the copper block, and therefore of the small cell, in the range of 180 to 300 K. The temperature calibration of the cooling cell is performed with the melting points of several organic substances (Appendix A.2).

3.2.2 Typical experimental run

Firstly, a glass substrate ($\varnothing=18$ mm) is coated with a hydrophobic layer. For this purpose, a few droplet of a 5% dimethyldichlorosilane/heptane solution are placed together with the glass substrate in a sealed glass cup (Knopf, 2003). The hydrophobic coated substrates have to be cleaned with acetone and water before they are used for an experiment. Up to 6 droplets are placed with a commercial micro pipette onto this glass substrate and immediately sealed with the small cap. The small cell is then placed onto the copper block and the entire cell is closed with the flange. The Labview interface, developed by Dobler (2003), consists of two parts. Firstly, the position of the droplets and their radii are set. Further the desired camera section is adjusted. These data are important for the subsequent analysis. In the second Labview application, the cooling and heating rates

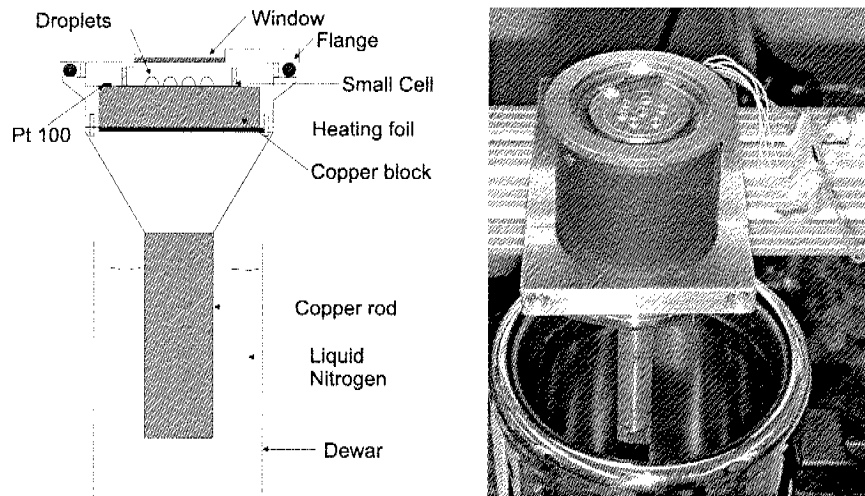


Figure 3.6: *Left panel: Detailed schematic setup of the cooling cell. Right panel: Photo of the cell with opened small cell.*

(typically 3 and 1 Kmin^{-1} , respectively), the start and end temperatures and the time interval between pictures taken with the camera can be set. Further, the live image is shown during the entire experimental run. The data for the cooling and heating cycles are saved in two different files.

After the dewar is filled with liquid nitrogen, the experiment can start. Note, that after the cooling cycle, the dewar must be refilled with liquid nitrogen. All the other applications are fully automated.

The raw data are saved in a binary code, and hence must be converted for the analysis into an ASCII code. This is performed with a third Labview application. Then, the resulting files can be analyzed with a simple Matlab routine, which leads to unambiguous freezing and melting points assignments to the droplets (Dobler, 2003).

3.3 Linkam cooling stage

The setup consists of a Linkam cooling stage (LTS 120), which is mounted on a microscope (Olympus BX 40), and connected to an external temperature controller (PE94) (Fig. 3.7). The temperature of the cooling stage can be adjusted between 243 and 393 K with a precision of ± 0.1 K, whereby a water cooled cooling inside the cell and a peltier element adjust the temperature of the sample block. Further, the cell is fixed onto motorized xy microscope stage platform. A commercial glass slide as the sample substrate is placed onto the temperature controlled sample block inside the cell. The temperature controller is connected over a RS232 port with a commercial computer, on which a HPVEE user

interface operates the setup (Gasser and Jöri, 2004). A CCD camera is set on the microscope and hence an experiment can be monitored on a digital video recorder. The entire setup is constructed for transmission as well as for reflection microscopy. The temperature calibration is shown in Appendix A.3.

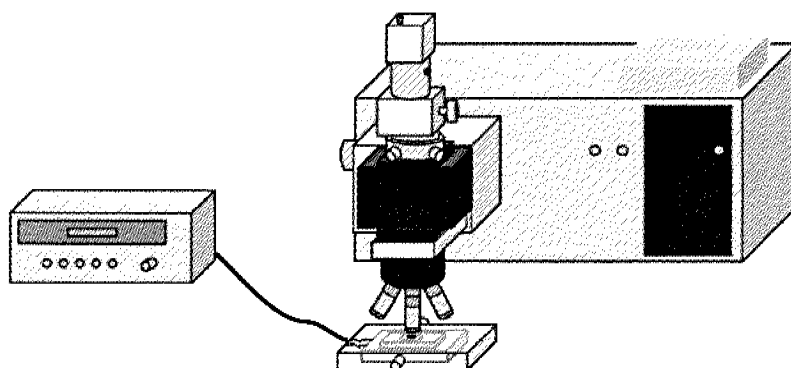


Figure 3.7: Setup of the Linkam cooling stage connected with a microscope (Courtesy of Gasser and Jöri, 2004)

3.4 Silica globules synthesis

Stöber et al. (1968) developed a simple synthesis to obtain nanometer sized silica (SiO_2) globules starting from tetracthylorthosilicate in the presence of an Ethanol/ NH_3 / H_2O mixture. It was shown, that the size of the globules depends on the ratio between the NH_3 and the H_2O concentration. Namely, the smaller this ratio, the smaller is the radius of the globules (van Helden et al., 1981). Our goal was to achieve a radius of ~ 100 nm. The four ingredients listed in Tab. 3.1 are added one after the other to a 500 ml Schott bottle and the mixture is stirred with a magnetic stirrer at room temperature for 18 hours. In a second part, the nanometer sized globules are isolated from the solvent mixture, which

Table 3.1: Required ingredients for the SiO_2 globules synthesis

$\text{C}_2\text{H}_5\text{OH}$ (pure, Fluka)	188 ml
H_2O (distilled and deionized water, 18.2 M Ω)	7 ml
25% $\text{NH}_3/\text{H}_2\text{O}$ (standard solution, Fluka)	7 ml
Tetra ethyl ortho silicate (TEOS, 99,9999%, Fluka)	8 ml

contains C_2H_5OH , NH_3 and H_2O . The mixture is divided in several centrifuge tubes, which are centrifuged for 1h with a velocity of 4000 rpm. Then the overlaying solution was poured off. The tubes were filled with distilled water and kept in an ultrasonic bath for 10 min. This entire procedure was repeated four times for every tube. This results in a whity solid substance, the pure SiO_2 globules. The powder is placed for 16 h in an oven at $100^\circ C$ and weighted afterwards. After the globules were placed again for 4 h in the oven, it was found that the mass of the globules remained constant. Therefore, one is certain that no water or alcohol remains attached to the globules. Figure 3.8 shows a photograph of the isolated SiO_2 globules made with an electron microscope. The globules have a mean diameter between 80-100 nm. With the pure globules a stock solution (0.47 wt% SiO_2 /water) is made, from which the further aqueous solutions are produced. Before using the solutions for an experiment, they were placed in an ultrasonic bath to prevent that the globules adhere to each other.

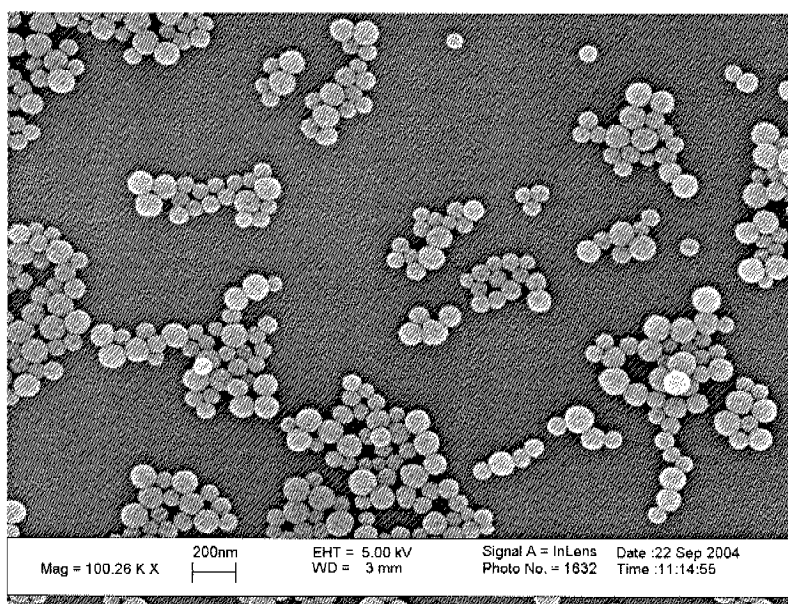


Figure 3.8: Photograph of the isolated SiO_2 globules performed with an Electron microscope with a magnification of 10^5 .

Seite Leer /
Blank leaf

Chapter 4

Results and discussion

A major problem that complicates the investigation of heterogeneous ice nucleation in the laboratory is the control of physical and chemical properties of the ice nuclei (IN). Desirable properties of IN are a well characterized surface and a high reproducibility, because this opens the possibility to repeat the experiments frequently enough to obtain a statistical information. In the first section, measurements of heterogeneous nucleation rate coefficients of droplets covered with nonadecanol are presented. Then heterogeneous freezing experiments with two organic and two inorganic IN are described separately. Two different approaches are then presented to analyze the results of heterogeneous freezing experiments for the different IN.

4.1 Heterogeneous ice nucleation rate coefficients of water droplets covered with nonadecanol

In order to determine the heterogeneous ice nucleation rate coefficient from single droplet experiments, a highly reproducible ice nucleus with a well characterized surface is favorable. Gavish et al. (1990) have shown that long chain alcohols ($C_nH_{2n+1}OH$ with $14 \leq n \leq 31$) arranged at the air/water interface of a liquid droplet fulfil both criteria. These alcohols, consist of a long hydrophobic tail and a hydrophilic OH head group, are insoluble in water and have a low vapor pressure. Depending on the chain number, large droplets covered with long chain alcohols can induce ice nucleation of temperature of up to 272 K.

Here, experiments were performed exclusively with nonadecanol, $C_{19}H_{39}OH$. Because of the small droplet sizes and the long experimental observation times, the monolayer arrangement is slightly changed compared to Gavish et al. (1990), namely the monolayer is not arranged at the air/water interface, but rather at a water/mineral oil interface (Fig. 4.1). This modification was necessary to prevent the droplet from evaporation. However, addi-

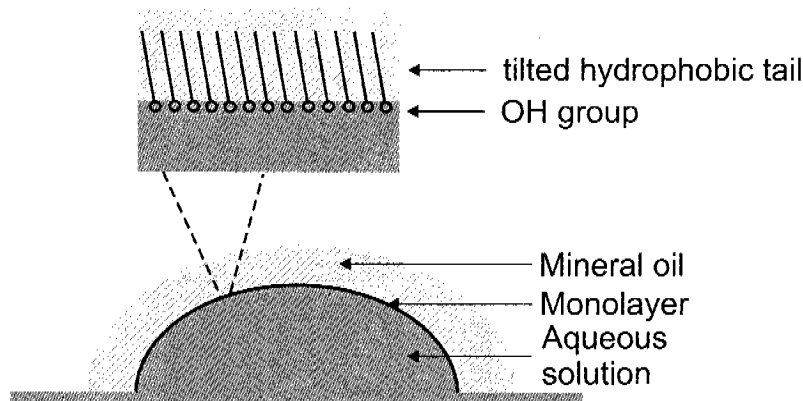


Figure 4.1: Scheme of a self-assembled monolayer of long chain alcohols at a water/mineral oil interface. The OH group is immersed into the water droplet.

tional experiments performed in this study with the nonadecanol arranged at the air/water interface indicate that no statistical significant difference (Wilcoxon rank sum test on a 5% level, see Appendix B.1) was found for the freezing temperature of droplets covered with the used nonadecanol/mineral oil solution and droplets where the nonadecanol is arranged at the air/water interface. Therefore, one can conclude that the droplets are fully covered and that nonadecanol has the same efficiency as an ice nucleus at the mineral oil/water interface as at the air/water interface. Further, a microscope photograph was taken at the beginning and at the end of every series to verify that the droplet size did not decrease due to water evaporation with increasing experimental duration.

The droplets are either placed with a pipette directly onto the DSC pan or sprayed with a custom made droplet generator (Knopf, 2003) onto the standard microscope glass slide for the Linkam cooling stage. Then, the droplets are covered with $\sim 50 \mu\text{l}$ of a $3.3 \cdot 10^{-3} \text{ M}$ nonadecanol/mineral oil solution, resulting in a self-assembled nonadecanol monolayer at the interface between the droplets and the mineral oil. The concentration of the nonadecanol/mineral oil solution is chosen higher than necessary for a complete monolayer coverage, to ensure that a full coating exists, even if a part of the nonadecanol molecules remain in the thin oil film covering the droplet.

Freezing points of differently sized droplets covered with a nonadecanol/mineral oil solution are investigated in the DSC and the Linkam cooling stage. The measurements with droplet radii of $r = 31$ and $48 \mu\text{m}$ were performed in the Linkam cooling stage, whereas the ones with $r = 320$ - $1100 \mu\text{m}$ in the DSC. For all experiments a moderate cooling rate of 10 Kmin^{-1} is used. Figure 4.2 shows the freezing point measurements of differently sized single water droplets covered with nonadecanol as a function of iteration number. Also included is a reference measurement of a droplet covered only with pure mineral oil without nonadecanol ($r = 1100 \mu\text{m}$), where the aluminum surface of the DSC pan acts

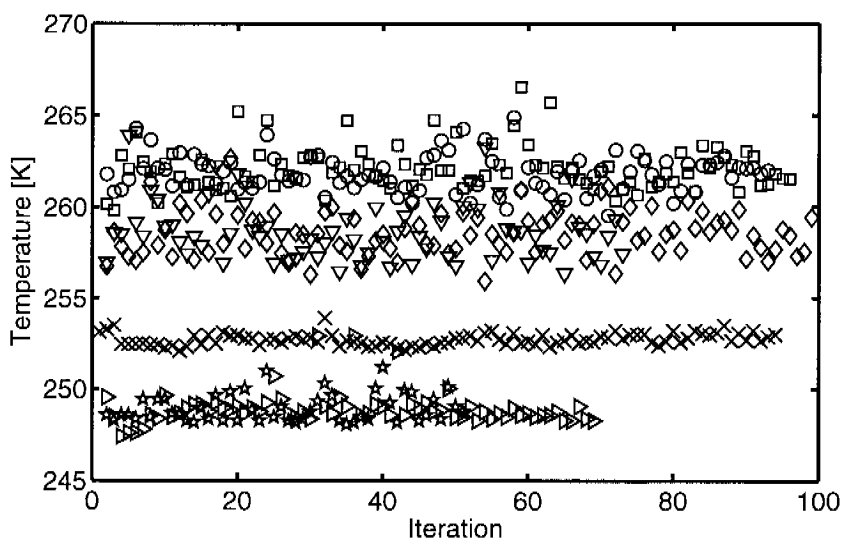


Figure 4.2: Measured freezing points for six droplets covered with nonadecanol and one uncoated droplet as a function of iteration number. Covered droplets: circles and squares: $r = 1100 \mu\text{m}$, diamonds and downward triangles: $r = 370$ and $320 \mu\text{m}$, respectively, stars and right pointed triangles: $r = 31$ and $48 \mu\text{m}$, respectively. Uncovered droplet: crosses: $r = 1100 \mu\text{m}$

as an ice nucleus. The freezing points of this droplet are always clearly below those of the coated droplets of the same size (circles and squares with crosses). Thus, one can conclude that the DSC pan surface does not induce ice nucleation of the droplets covered with nonadecanol. The slopes of a linear fit through the data series were tested with a t-test on a 5% level (see Appendix B.2) to ensure that no systematical increase or deviations in the freezing temperature occurs during the experiment time. Only series with no statistically significant deviance in slopes were taken. Since in the first experimental run a different starting temperature is used, the first freezing point is skipped for all series. This is necessary, because Socoly and Seidler (2001a) recently have reported that the freezing temperature of droplets covered with long chain alcohols depend on the start temperature of the experimental run, indicating the potential for pre-activation of such self assembled monolayers. This means that depending on the temperature, the crystalline structure of such alcohols may have a slightly different orientation thus may induce ice nucleation at a lower temperatures. So, one can treat each series as a sum of independent, identically conditioned freezing point measurements, which is a required condition for poisson statistics.

Most series show a broad scatter in freezing temperatures as a function of iteration number, which clearly reflects the stochastic behavior of the nucleation process. The scatter of the covered droplets is getting narrower with decreasing radii or decreasing temperature.

On the other hand, the freezing points of the uncoated droplet fall into a very narrow range. To evaluate each data series in more detail and to apply poisson statistics, each series of Fig. 4.2 is divided into equally sized temperature bins. Since every series is treated separately and the purpose was to obtain similar bin numbers, the temperature interval of the bins varies for each series. A mean nucleation rate coefficient (j_{het} , see Tab. 4.1) is calculated with Eq. 2.38 for every bin in a series, whereby the surfaces of the IN for the coated and the uncoated droplets are assumed to be a hemisphere and circular area, respectively. According to Eq. 2.21, a contact angle is calculated for each measured j_{het} . Table 4.1 indicates clearly, that j_{het} strongly increases with decreasing temperature. The difference between the first and the last bin is 2 orders of magnitude in the rate coefficient in a temperature range of 1.4 K, which is similar to that of the homogeneous ice nucleation rate coefficient from supercooled liquid water droplets (~ 2.1 orders of magnitude per 1.4 K, Pruppacher and Klett, 1997). Figure 4.3 shows the measured j_{het} values and a calculated curve (with Eq. 2.21, $\alpha_{\text{mean}} = 69.2^\circ$) as a function of temperature for the uncoated droplet series. α_{mean} represents an average value of the α 's weighted by the number of freezing events in the same bin. The large steepness of the calculated curve points out, that the freezing probability distribution of the measurements as a function of temperature must be extremely narrow and thus extremely sensitive to small temperature variances resulting from the temperature calibration. Upper and lower heterogeneous limits of j_{het} resulting from the poisson statistics are depicted for each measured j_{het} as thin vertical lines (see Appendix B.3). The relatively small number of freezing events per bin evaluated with poisson statistics leads to an asymmetric uncertainty range for the different data points. Considering the uncertainty ranges resulting from the poisson statistics together with that of the temperature calibration, the measured j_{het} are well described by the calculated curve with a constant α_{mean} , although the calculated values for α show a slight increase with decreasing temperature (see Tab. 4.1). A constant α for a rigid surface is in accordance with Seeley and Seidler (2001b), which found in similar experiments that $\alpha = 69^\circ$ fit their results best for droplets on a glass substrate. Measurements over a wider temperature range could further strengthen the conclusion of a constant α for the alumina surface of the DSC pan, but was not possible to achieve with the present experimental setups.

The measured j_{het} of the droplets covered with nonadecanol cover a wider range in temperature than those for the uncovered droplet. The increase of j_{het} as a function of temperature is just ~ 0.28 orders of magnitude in a temperature range of 1.4 K. Within the scheme of CNT, this small slope is reflected by a pronounced linear increase of α with decreasing temperature (Fig. 4.4). Figure 4.5 shows a comparison of two calculated curves of j_{het} as a function of temperature. The dashed blue line is obtained with a mean value of 56.8° for α_{mean} , which is again calculated as an average of the α 's weighted by the number of freezing events in the bin. On the other hand, the solid blue line is obtained with the temperature dependent function for α (see Fig. 4.4). It is obvious, that a constant α can not reproduce the measured heterogeneous nucleation rate coefficients. The slope of the

Table 4.1: Analysis of ice nucleation properties for six droplets coated with nonadecanol and one uncoated droplet. The symbols and colors are the same as in Fig. 4.2. r : radius of the droplet, n_{tot} : total number of freezing events in a series, $n_{\text{nuc},i}$: number of freezing events in a specific bin, T_i : mean temperature of a bin, $j_{\text{het},i}$: calculated mean heterogeneous rate coefficient of a bin. α : Contact angle calculated with Eq. 2.21.

Series		$r = 1100 [\mu\text{m}]$			Series		$r = 1100 [\mu\text{m}]$		
bin i	$n_{\text{nuc},i}$	T_i [K]	$\log j_{\text{het},i} [\text{cm}^{-2}\text{s}^{-1}]$	α	$n_{\text{nuc},i}$	T_i [K]	$\log j_{\text{het},i} [\text{cm}^{-2}\text{s}^{-1}]$	α	
1	10	260.1	0.792	51.3	18	260.5	0.701	50.3	
2	31	261.1	0.416	48.9	50	261.8	0.267	47.3	
3	36	262.2	0.087	46.4	18	263.2	-0.436	44.3	
4	11	263.3	-0.571	44.1	7	264.5	-0.895	41.0	
5	4	264.4	-1.041	41.5	2	265.9	-1.460	37.5	
Series		$r = 370 [\mu\text{m}]$			Series		$r = 320 [\mu\text{m}]$		
bin i	$n_{\text{nuc},i}$	T_i [K]	$\log j_{\text{het},i} [\text{cm}^{-2}\text{s}^{-1}]$	α	$n_{\text{nuc},i}$	T_i [K]	$\log j_{\text{het},i} [\text{cm}^{-2}\text{s}^{-1}]$	α	
1	14	256.6	1.633	58.8	24	257.1	1.531	57.7	
2	39	258.0	1.218	56.0	30	258.6	1.112	54.5	
3	33	259.3	0.824	53.1	11	260.1	0.501	51.3	
4	10	260.7	0.191	50.3	5	261.6	0.103	47.9	
5	2	262.0	-0.528	47.4	2	263.1	-0.312	44.31	
Series		$r = 31 [\mu\text{m}]$			Series		$r = 48 [\mu\text{m}]$		
bin i	$n_{\text{nuc},i}$	T_i [K]	$\log j_{\text{het},i} [\text{cm}^{-2}\text{s}^{-1}]$	α	$n_{\text{nuc},i}$	T_i [K]	$\log j_{\text{het},i} [\text{cm}^{-2}\text{s}^{-1}]$	α	
1	30	248.5	3.787	76.1	39	248.1	3.535	77.5	
2	11	249.3	3.060	75.2	25	249.5	2.564	75.3	
3	7	250.0	2.748	73.6	1	250.9	1.112	73.5	
4	2	250.8	2.170	72.4	3	252.2	1.582	69.4	
Series		$r = 1100 [\mu\text{m}]$			Series		$r = 1100 [\mu\text{m}]$		
bin i	$n_{\text{nuc},i}$	T_i [K]	$\log j_{\text{het},i} [\text{cm}^{-2}\text{s}^{-1}]$	α	$n_{\text{nuc},i}$	T_i [K]	$\log j_{\text{het},i} [\text{cm}^{-2}\text{s}^{-1}]$	α	
1	31	252.3	1.168	69.7					
2	46	252.8	0.605	69.1					
3	13	253.2	-0.138	68.7					
4	3	253.7	-0.803	68.2					

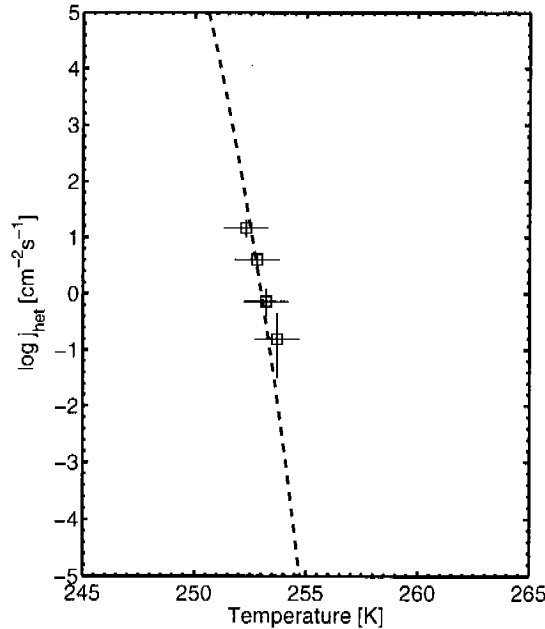


Figure 4.3: Measured heterogeneous rate coefficients for the uncoated droplet (squares) as a function of temperature. Dashed line: Calculated j_{het} with a constant α_{mean} of 69.2° . The horizontal and vertical black lines are the errors in the temperature measurements and the uncertainties due to the poisson statistics on the 95% level, respectively.

fit is too steep and does not flatten with decreasing temperature. The calculated curve with the temperature dependent α describes the measurements much better. At higher temperatures the slope of the solid blue curve has the same steepness as the dashed blue curve, but also reproduces the more flat part at ~ 255 K as well as the new increase at lower temperatures. Considering also the poisson uncertainties on the 95% level together with the temperature uncertainties, most of the data points are nicely reproduced by the solid blue curve. This comparison shows, that the temperature dependence of j_{het} is dominantly determined by α , which becomes obvious by considering Eq. 2.21 in more detail. Factors one ($\frac{kT}{h}$) and three (n_s) depend only linear on temperature and ΔF_{diff} increases somewhat with decreasing temperature ($\frac{\Delta F_{\text{diff}}(250 \text{ K})}{\Delta F_{\text{diff}}(265 \text{ K})} \simeq 1.1$). Thus, the term $\Delta G_{\text{hom}} \cdot f(\alpha)$ has to describe most of the temperature dependence of j_{het} . ΔG_{hom} is very large close to the melting point of ice, but decreases strongly with decreasing temperature leading to the steep increase of the nucleation rate coefficient characteristic for homogeneous ice nucleation. A constant α leads to a shift of this curve to higher nucleation rate coefficients while preserving its slope. A variable α is therefore indispensable to achieve a change of this slope.

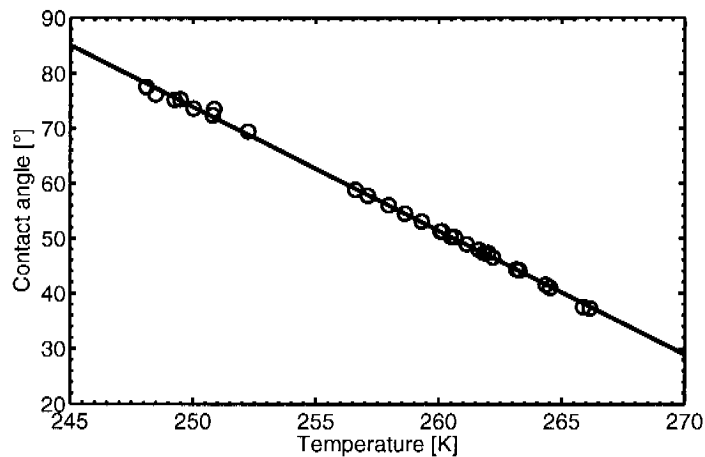


Figure 4.4: Circles: Calculated α values for water droplets covered with nonadecanol as a function of temperature (see Tab. 4.1). Solid line: linear fit of the circles, whereas $\alpha(T) = 636.196 - 2.249T$. α is given in degree and the function is valid for $248 \leq T \leq 268$ K.

In a recent work, the kinetics of the ice nucleation process of single water droplet series covered with 4 different long chain alcohols (C_{25} - C_{28}) over a small temperature range were reported ($261 \text{ K} < T < 268 \text{ K}$, Seeley and Scidler, 2001b). By reducing the prefactor (first three factors of Eq. 2.21) by 15 orders of magnitude, Seeley and Scidler (2001b) were able to bring their measurements in accordance to CNT, while keeping α constant (their α 's lies in a range between 19 and 31° for the different alcohols). The authors claimed, that this reduction can mainly be explained as a result of a hindered molecular diffusion of the water molecules to the interfacial plane, resulting from the dipole forces between the long chain alcohol film and the interfacial water molecules. The dashed dotted blue line in Fig. 4.5 is obtained by using the approach of Seeley and Scidler (2001b), i.e., reducing the prefactor by 15 orders of magnitude and keeping α constant. At higher temperature, this results in a far better agreement with the measured j_{het} than that obtained with just a constant α . However, the curve does not monotonously increase with decreasing temperature, which is clearly in contrast to the measurements. The shape of the curve with the reduced prefactor is not surprising, since the leveling off at lower temperatures is a general feature of CNT which is just shifted to lower nucleation rate coefficient values when one reduces the prefactor. It is therefore obvious, that a general reduction of the prefactor by a constant value can not solve the discrepancy between CNT and the measurements.

So far, we have seen that the measured heterogeneous rate coefficient of differently sized droplets covered with nonadecanol can be reproduced by assuming a temperature dependent α . The reasons for this large increase of α with decreasing temperature still remain unclear. Note that an enlarged α implies that the efficiency of the ice nucleus is getting

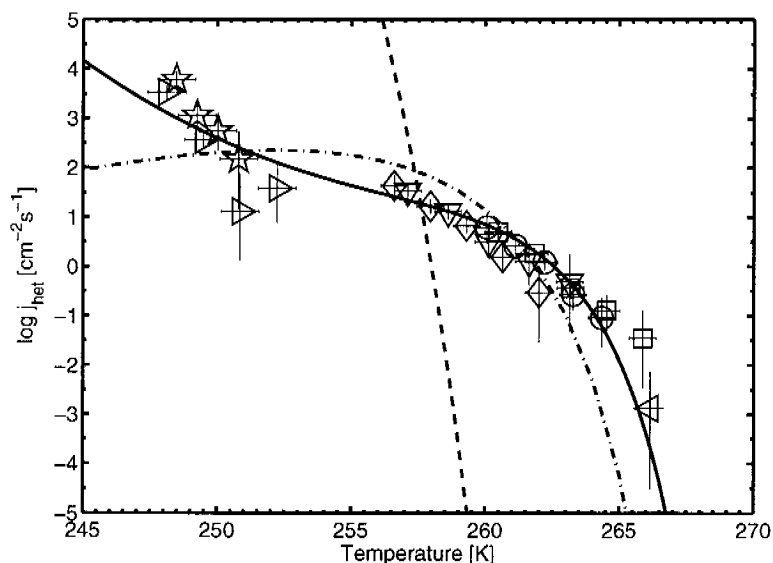


Figure 4.5: Measured heterogeneous nucleation rate coefficients for six single water droplets covered with nonadecanol as a function of temperature. The symbols are the same as in Fig. 4.2. Additionally, a direct measurement of j_{het} (left pointed triangle) at 266.15 K is added. For this purpose, a 3 μl droplet covered with the nonadecanol/mineral oil solution was kept at 266.15 K in the DSC and the time was measured until the droplet froze. Thus the nucleation rate coefficient can be calculated directly with Eq. 2.37 and 2.38. Dashed blue line: Best fit of the CNT with a constant α of 56.8° , solid blue line: Best fit of the CNT with temperature dependent α (see Fig. 4.4), dashed dotted blue line: best fit according to the approach of Seeley and Seidler (2001b). The horizontal and vertical red lines are the errors in temperature and the uncertainties due to the poisson statistics on the 95% level, respectively. The three curves are discussed more detailed in the text.

worse. In the next paragraph, the molecular arrangement and structural properties of long chain alcohols on the water droplets are presented, which could help to find a possible explanation for the changing contact angle with decreasing temperature.

Together with the close structural match of the alcohols' 2D lattice and that of hexagonal ice, the tilt angle of the molecules on the droplet surface, the molecular motion of the alcohols, and the degree of order of the 2D lattice have been identified as major factors influencing the nucleation efficiency of long chain alcohols arranged at the air/water interface (Gavish et al., 1990; Majewski et al., 1993; Popovitz-Biro et al., 1994; Majewski et al., 1995). The basal ab plane of the hexagonal unit cell of ice forms a rectangle with the dimension of 4.52 and 7.83 \AA (Fig. 4.6). Table 4.1 lists measured lattice parameter for some long chain alcohols on water droplets at 278 K and on vitreous ice. The measurements at 278 K confirm that in general a close match with the rectangle in the unit cell of

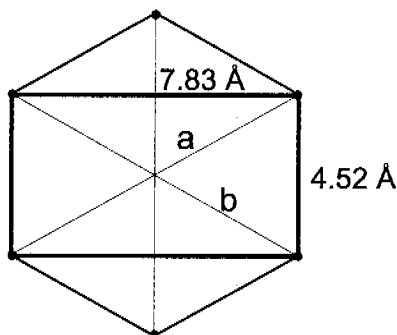


Figure 4.6: View onto the basal ab plane of the hexagonal ice unit cell. Note, that the length of the c -axis (perpendicular to the paper plane) of the hexagonal ice lattice is 7.36 \AA . However, since nucleation for this type of IN occurs onto the ab plane of the hexagonal lattice, the length of the c -axis of the ice lattice does not affect the nucleation process.

ice exists. C31 has a closer area match to ice than C30, a smaller tilt angle and induces ice nucleation at a $\sim 7 \text{ K}$ higher temperature. On the other hand, droplets covered with C23 have a higher freezing temperature than those of C30, although the 2D area and the tilt angle are both larger when compared to those of C30, implying a worse match with ice. Therefore, it seems reasonable that the lattice parameters alone can not determine whether a long chain alcohol is a good ice nucleus or not. Popovitz-Biro et al. (1994) found, that alcohols with odd and even C-atom numbers have a different OH group orientation in the water droplets, which will strongly influence the ice nucleation ability, since this head group will probably be the core of the ice embryo. The authors further concluded that the OH group orientation coupled with the possible molecular rearrangement on the droplet surface are additional reasons for the nucleation efficiency of the alcohols. This argument seems to be more convincing, because the two alcohols C31 and C30 have almost identical lattice parameters and tilt angles, but their heterogeneous freezing temperature is distinctly different. In a recent theoretical work, Nutt and Stone (2003) were not able to reproduce the different ice nucleation abilities of C31 and C30 using intermolecular potentials, and thus concluded that accurate Molecular Dynamics (MD) simulations are needed to determine the exact arrangement of long chain alcohols on the water surface. It seems reasonable, that the lattice parameters can change as a function of temperature, and therefore improve or reduce the freezing ability of such an alcohol. Measurements of the lattice parameters on vitreous ice indicate that the match for the C31 alcohol remain almost constant over this large temperature range, which is not true for the C16 alcohol. In a MD study between 272 and 300 K, Dai and Evans (2001) found a slight decrease of the lattice parameter as well as the tilt angle for the three alcohols C29, C30 and C31, which is in accordance with the measurements of Majewski et al. (1993). Since long chain alcohols have a considerable molecular motion at the water surface, the alcohols may re-

Table 4.2: Lattice parameters of the 2D crystalline structure for different long chain alcohols on water droplets at 5°C (Majewski et al., 1995) and on vitreous ice at ~100 K (Majewski et al., 1993). T_{het} are the heterogeneous freezing temperatures of large droplets covered with the long chain alcohol (Gavish et al., 1990).

Long chain alcohols					
On water droplets at 278 K					
number of C-atoms	a [Å]	b [Å]	2D area (ab/2) [Å ²]	tilt angle (γ) [°]	T_{het} [K]
31	4.98	7.45	18.55	7.0	272.02
30	4.99	7.49	18.69	7.5	265.17
23	5.00	7.56	18.80	9.5	269.38
20	5.05	8.00	20.20	19.0	262.22
19	5.03	8.13	20.45	21.0	266.13
18	4.99	8.19	20.44	19.5	262.14
17	4.94	8.34	21.10	18.5	262.66
16	4.86	8.41	20.84	16.0	259.44
On vitreous ice at ~100 K					
31	5.05	7.42	18.73	-	-
16	5.00	7.20	18.00	-	-
Hexagonal ice					
-	4.52	7.83	17.63	-	-

arranged themselves into a closer match to the ice lattice (Popovitz-Biro et al., 1994). A rearrangement of molecules will need an external amount of energy, which probably will depend strongly on the number of rearranged molecules. Because the critical ice embryo is larger at higher temperature, the required rearrangement energy would also be larger at higher temperature. This would imply that long chain alcohols are worse IN at higher temperature, which is in contrast to the measurements. Because of the increasing viscosity of water with decreasing temperature, a rearrangement of the long chain alcohols could indeed be worsened at lower temperature, which would consequently lead to an increase in the contact angle. On the other hand, the contact angle depends on the interrelation between the interfacial tensions of the different interfaces between ice, water and the long chain alcohol (see Eq. 2.20 and Fig. 2.2). The interfacial tension between water and ice can be parameterized over a wide temperature range, but no measurements in the supercooled regime of the interfacial tension of water/nonadecanol could be found in the literature. Even more pronounced, the interfacial tension between ice and the crystalline 2D structure of the long chain alcohols are not measurable at all. This shows one weakness of CNT, namely that the contact angle is approximated by macroscopic interfacial tensions, whereas the nucleation process itself happens on a microscopic scale. Therefore, one may

consider the temperature dependent α simply as a parameter that scales ΔG_{hom} , without knowing the exact physics behind it. Similar studies with other IN could help to gain more knowledge on the factors that influence the nucleation abilities of long chain alcohols and/or heterogeneous ice nucleation in general.

Nevertheless, the obtained fit function for j_{het} with a variable α can be used in micro-physical models, to estimate a possible change in ice number density and ice particle sizes of clouds nucleated by heterogeneous ice nucleation with nonadecanol compared to a homogeneously nucleated cloud. Such simulations are presented in Section 5.2.

4.2 Ice freezing experiments with various ice nuclei

Heterogeneous freezing points of different aqueous solutions containing various IN (two organic and two inorganic) are investigated with the DSC and the single droplet apparatus. The IN are either immersed in the droplet or arranged on the droplet's surface. The IN were chosen to have either atmospheric relevance and/or good physical and chemical properties for laboratory experiments. Besides the interest in heterogeneous ice nucleation in the atmosphere, a second goal of the experiments was to get a better knowledge of heterogeneous ice nucleation processes in general.

4.2.1 Nonadecanol

In Section 4.1, ice nucleation experiments with nonadecanol arranged at the air/mineral oil interface on pure water droplets have been investigated. So far, whether nonadecanol nor another long chain alcohols were never investigated arranged on aqueous solutions droplets and thus Single droplet measurements of different aqueous solutions covered with nonadecanol at the air/water interface are presented. The experiments were performed with the single droplet apparatus described in Chapter 3.2 and the solutes are chosen to cover a large range in freezing temperatures. In each experimental run, six $3 \mu\text{l}$ droplets are placed on a hydrophobically coated glass substrate. The nonadecanol monolayer is prepared by spreading $0.5 \mu\text{l}$ of a $2.5 \cdot 10^{-4}$ M nonadecanol/hexane solution. After ~ 10 seconds, the hexane is evaporated and subsequently the droplets are sealed with the small cell. In a regular experimental run, five freezing and melting cycles are performed with the same droplet. Since the first freezing cycle starts from a different temperature than the other four cycles, it is skipped for the evaluation of all measurements.

Figure 4.7 depicts ice melting and heterogeneous freezing points for different aqueous solution droplets covered with nonadecanol as a function of mole fraction of the solute. Each data series represents four freezing and melting cycles of 6 to 12 independent droplets of similar concentrations. To take into account possible evaporation during sample preparation and/or during the experimental observation time, the mole fraction is calculated for

each droplet with the measured ice melting points. This means, together with literature data (Bertram et al., 2000; Linke, 1958) the measured melting points can be transformed into a mole fraction value for each data point. If the solutions behaved ideally, all measured melting points would fall onto a straight curve, since under ideal conditions, the melting point temperature is independent of the nature of the solute, but solely depends on the concentration. However, Fig. 4.7 depicts clearly, that at high concentrations of the solution, ideality is not fulfilled.

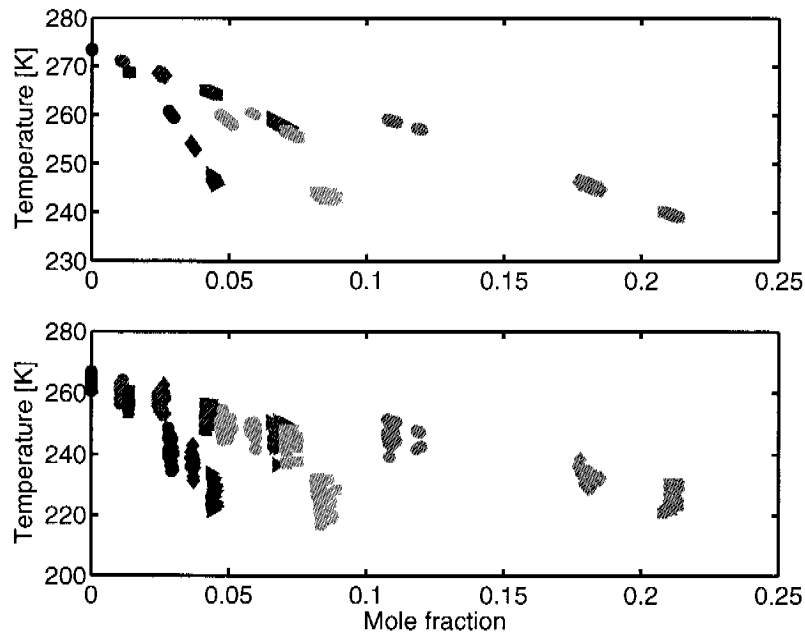


Figure 4.7: Ice melting (upper panel) and heterogeneous ice freezing points (lower panel) of different aqueous solution droplets covered with nonadecanol as a function of mole fraction of the solute. Each symbol represents one ice freezing or melting point, respectively. The same color and symbol code is used for both panels. \bullet : H_2O ; \blacklozenge , \blacktriangle and \blacktriangleright : 5.56, 14.98, 23.90 and 34.21 wt% $(NH_4)_2SO_4$; \blacksquare , \bullet , \blacklozenge and \blacktriangleright : 6.89, 13.71, 17.31 and 19.58 wt% $MgCl_2$; \ast and \blacksquare : 29.81 and 43.84 wt% $Cu(NO_3)_2$; \ast and \blacksquare : 15.11 and 19.85 wt% $NaCl$; \bullet , \blacklozenge and \blacksquare : 30.01, 42.86 and 48.08 wt% ethylene glycol. Because of clarity, the temperature uncertainties due to calibration are not depicted, but they correspond to twice the size of the symbols, i.e., ± 0.2 K, respectively.

The heterogeneous freezing points of a single data series vary considerably, whereby the scatter is somewhat increasing with decreasing freezing temperature. The maximal difference between the highest and the lowest freezing temperature of a series is almost 16 K (see last line in Tab. C.1). This large scatter can be explained mainly by two reasons. Firstly, nucleation is a stochastic process and secondly, a possible change in the concentration of the droplets would also contribute to the scatter. The influence of the latter point can be investigated in the melting points of the droplets. The melting points of a series of similar prepared droplets show a larger scatter than expected from the temperature uncertainty of the calibration, indicating that the concentrations of the droplets in a series differ slightly. For example, four melting points of the same droplet in the magenta colored bullets series correspond to a distinctly larger mole fraction than the other melting points of the series, indicating that the concentration of this droplet was already at the beginning of the experimental run different. Because of the different ice melting points for similar prepared droplets, the droplets can not be treated as equal samples, which is a required condition to apply poisson statistics. Hence, these data series can not be used to estimate heterogeneous rate coefficient with poisson statistics. In summary, Fig. 4.7 depicts clearly that the measured heterogeneous freezing points depend on nature of the solute and not only on the mole fraction. For example, the blue right pointed triangles and the cyan bullets have the same mole fraction, but their freezing points are distinctly different (more than 20 K between in their median freezing temperature).

4.2.2 Silver iodide (AgI)

It was found in laboratory experiments, that AgI initializes ice nucleation in the deposition mode at temperatures up to 269 K (Pruppacher and Klett, 1997). In the 50's, scientists have started to use this capability to prevent the growth of large ice particles in lower tropospheric clouds, because such ice particles can cause large damage on agriculture by hailstorms. For this purpose the clouds were seeded with solid AgI powder, which should result in a larger ice number density and smaller particles. However, most of these field mission have been stopped, because of little success. Nevertheless AgI is one of the most investigated IN in the laboratory overall, whereas as the deposition mode with pure water vapor (Pruppacher and Klett, 1997) as well as the immersion mode in pure water have been investigated (Heneghan et al., 2002). Here, freezing experiments with immersed AgI in emulsified aqueous solution are presented.

Two different approaches for the AgI preparation have been tested, whereas all experiments were performed in the DSC. Firstly, AgI powder was suspended in an aqueous solutions, from which small portions were taken for the preparation of the emulsions and secondly, AgI is precipitated in droplets while the emulsions were drilled. Experiments

using the first approach were performed as follows: The aqueous suspension of the AgI powder is placed in an ultrasonic bath for 15 min, and before the emulsion is prepared with this solution. The freezing curves of such emulsions were identical with those of homogeneous ice nucleation in the absence of the heterogeneous IN. Therefore, one can conclude, that no solid AgI is present in the emulsion droplets. Since AgI has a high density, it seems likely that during the preparation the AgI sediments to the bottom of the test tube. Therefore, experiments using this approach were no longer pursued.

To precipitate AgI crystals *in situ*, the procedure for the emulsion preparation (see Chapter 3.1.2) has to be changed slightly. Now, 0.1 ml of a 1.64 wt% AgNO₃, 1.6 ml of a 22 wt% lanolin/mineral oil and 0.1 ml of a 1.61 wt% KI solution are added one after the other to a test tube. This mixture is stirred for 5 min, leading to the precipitation of AgI crystals within the emulsion droplets. Then 0.4 ml of an additional solution (e.g., 10 wt% LiCl solution) is added and then the entire mixture is stirred for another 15 min. Since the solubility product of AgI is smaller than the solubility products of LiI, AgCl, KCl or LiNO₃ and the LiCl is added lastly, one can be certain that AgI must have been precipitated. The composition of the emulsion droplets consists of solid AgI together with an aqueous remainder solution containing solvated K⁺, NO₃⁻ and the additional solution. All the solutes were taken into account to calculate the concentration within the emulsion droplets. Further it was assumed, that AgI is fully precipitated.

Figure 4.8 depicts a DSC freezing curve of an emulsion containing *in situ* precipitated AgI and a 10 wt% LiCl solution is was used for the additional solution. Two large freezing peaks can be identified at two different temperatures, which indicates clearly that not all droplets in the emulsion behave equally. The first freezing peak represents heterogeneous freezing on the precipitated AgI crystals, whereas the second one corresponds to the homogeneous freezing of the aqueous droplets in the emulsion. Since heterogeneous freezing temperature can depend on the surface of the ice nucleus, experiments with a ~ 1.5 smaller total AgI surface compared to the above preparation method have been investigated. For this purpose, only 0.05 ml of the AgNO₃ and the KI solutions are used for the emulsion preparation, respectively. The preparation procedure with the larger AgI surface is denoted as the blue procedure, whereas the other one as the red procedure.

Figure 4.9 shows the measured ice melting, heterogeneous and homogeneous ice freezing points of different emulsified aqueous solutions samples as a function of total mole fraction of the solution. The shown data are mean values for several freezing and melting points of the same emulsions (All single measurements are listed in Tab. C.2). In all three panels, the data are widely scattered as a function of mole fraction. For example, the black square and the grey bullet have nearly the same mole fraction (~ 0.06), but the heterogeneous and homogeneous freezing points as well as the ice melting points differ up to 25 K. A similar behavior was also found for the large droplets covered with nonadecanol (see Section 4.2.1). The scatter in the heterogeneous freezing points could be influenced by the varying surface of the AgI. However, considering the two green bullets at a mole fraction

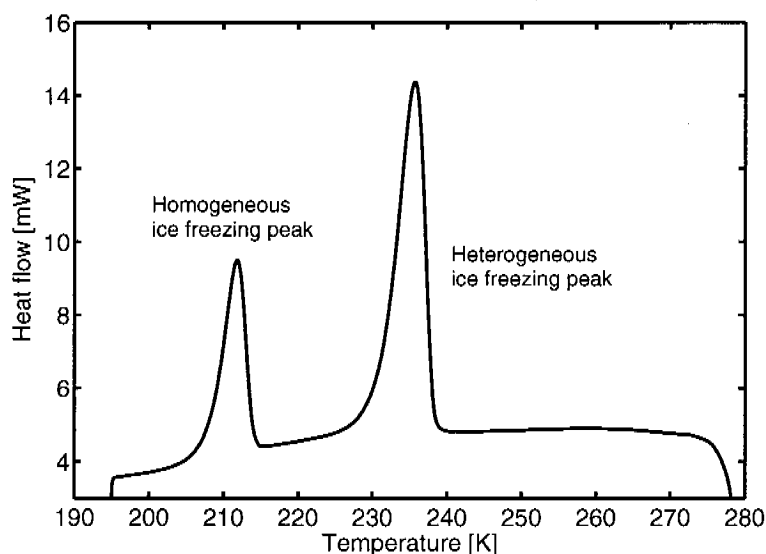


Figure 4.8: DSC freezing curve of an emulsion containing *in situ* precipitated AgI, whereas a 10 wt% LiCl solution is used for the additional solution. Two freezing peaks are identified, the heterogeneous at higher temperature and the homogeneous freezing peak at lower temperature, indicating that not in all droplets AgI was present.

close to zero, indicates that the difference in the heterogeneous freezing points of the two samples is smaller than 0.2 K, which is smaller than the precision of emulsions preparation (Note that in the upper two panels the points are almost congruent and therefore one is hardly visible.). Therefore, one can conclude, that an enlargement of the AgI surface by a factor of ~ 1.5 does not change the heterogeneous freezing temperature. Thus, the heterogeneous nucleation rate as a function of temperature must be extremely steep at this temperatures, which is common for ice nucleation processes and was found in the previous section for the aluminum surface of the DSC pan. Hence, one can conclude that a change of the AgI surface is not responsible for the large scatter in the heterogeneous freezing temperatures. The summary of these experiments can be considered similar to that of the large droplets covered with nonadecanol, that the measured heterogeneous freezing points depend on nature of the solute and not only on the mole fraction.

4.2.3 Silica (SiO_2)

Stöber et al. (1968) have shown that with a simple synthesis mono dispersed SiO_2 globules can be obtained (see Section 3.4). Hence, the the total surface of the ice nucleus is well known and thus heterogenous freezing experiments with a aqueous suspensions of SiO_2

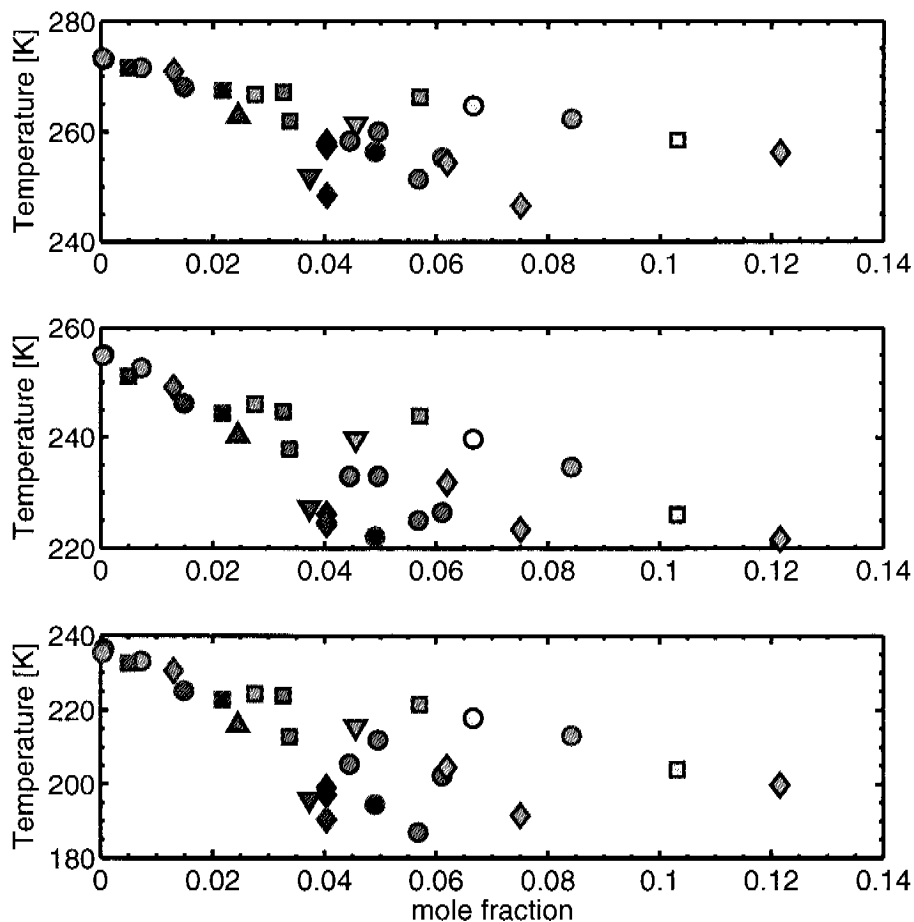


Figure 4.9: Homogeneous and heterogeneous freezing and corresponding ice melting points of emulsified aqueous solutions with immersed AgI. Upper panel: ice melting points, middle panel: heterogeneous freezing points, lower panel: homogeneous freezing points. The bordered colors of the symbols denotes the different preparation procedure, whereas for blue 0.1 ml and for red 0.05 ml of the AgNO_3 and KI solutions are used. The colors and the symbols are labelled as follows: Light green bullets: water; Magenta square and bullets: 19.5 and 28.3 wt% $\text{NH}_4\text{CH}_3\text{COO}$; Cyan bullet, square, downward triangle and diamonds: 2.0, 7.7, 14.9 and 19.9 wt% LiCl; Black square, bullet and diamonds: 17.9, 35.1 and 35.9 wt% K_2CO_3 ; Yellow bullet and square: 39.6 and 55.0 wt% glycerol; Gray diamond, square and bullets: 13.0, 29.8 and 43.9wt% CaNO_3 ; Orange square, bullet and diamond: 21.4, 29.9 and 48.0 wt% ethylene glycol; Purple square, bullet, upward triangle, downward triangle and diamond : 3.0, 9.0, 17.1, 22.5 and 25.0 wt% MgCl_2 . Because of clarity, no uncertainties ranges are depicted, but would exhibit ± 0.2 K and ± 1.0 K for the ice melting points and the ice freezing points, respectively.

globules have been performed. A 0.47 wt% mother suspension was made, from which the other aqueous solutions are prepared. Firstly, emulsions with the mother suspension are stirred and compared to emulsions with pure water. The DSC freezing curves of such two emulsions are not distinguishable. Two different reasons could be responsible for this. Firstly, the SiO₂ globules do not or just poorly act as IN, and therefore homogeneous and heterogeneous freezing temperatures are identical within the accuracy of the measurements. Secondly, the SiO₂ globules could leak into the oil matrix of the emulsions during the stirring process. Therefore in a second approach, large droplets containing SiO₂ (3 μl) are investigated in the DSC. This time, the globules could only sediment to the bottom of the DSC pan, but have to stay in the droplets. Similar to the experiments in the previous section, the DSC pan will also act as an ice nucleus. Therefore, one has to distinguish whether the droplets nucleated on the DSC pan or on the SiO₂ globules. This discrimination is performed for blank and SiO₂ globules containing droplets and shown exemplarily in Tab. 4.3 for 8 freezing temperatures for droplets consisting of a 7.76 wt% (NH₄)₂SO₄ and of a 7.73 wt% (NH₄)₂SO₄/0.47 wt% SiO₂ solution, respectively. The volume of all droplets is 3 μl. The comparison shows clearly that although the weak freezing efficiency of the SiO₂ globules, data series with and without these globules are distinguishable with the Wilcoxon rank sum test on a 5% level. Figure 4.10 depicts the individual freezing points of large aqueous solution droplets with SiO₂ globules as a function of mole fraction of the solution. The scatter in freezing temperature is for mostly series ~5 K, and can be related

Table 4.3: Freezing point comparison of 3 μl droplets with and without suspended SiO₂ performed with the Wilcoxon rank sum test on a 5% level. Samples Nr.1 is made of a 7.76 wt% (NH₄)₂SO₄ solution, whereas samples Nr.2 of a 7.73 wt% (NH₄)₂SO₄/0.47 wt% SiO₂ solution. For every droplet 8 freezing points are investigated, T_{f1} to T_{f8}. *p* is the probability of the Wilcoxon rank sum test that the two compared series are equal or not and indicates whether the null hypothesis (i.e., median of the series are equal) is rejected or not. *h*=0 means that the null hypothesis is valid on a 5% level. Thus for *h*=1, the two series can be considered as two distinguishable droplet series.

	blank	SiO ₂
T _{f1}	237.68	243.93
T _{f2}	235.80	242.11
T _{f3}	236.18	241.69
T _{f4}	235.80	240.39
T _{f5}	239.43	245.43
T _{f6}	240.73	245.17
T _{f7}	239.03	244.44
T _{f8}	239.59	244.22
$p=1.5 \cdot 10^{-4}$, $h=1$		

to the statistical behavior of the nucleation process. Further one can not exclude, that the SiO_2 globules stick together, and thus reduce the SiO_2 surface. However, both IN with a rigid surface in the previous Sections have shown, that a reduction or an enlargement of the surface by a factor of ~ 2 does not change the heterogeneous freezing temperature noticeably. As in the previous results, no obvious between the freezing temperatures and the mole fraction of the droplets can be found. The blue triangles and the magenta bullets for example have similar heterogeneous freezing points, whereas their mole fractions differ by about a factor of two.

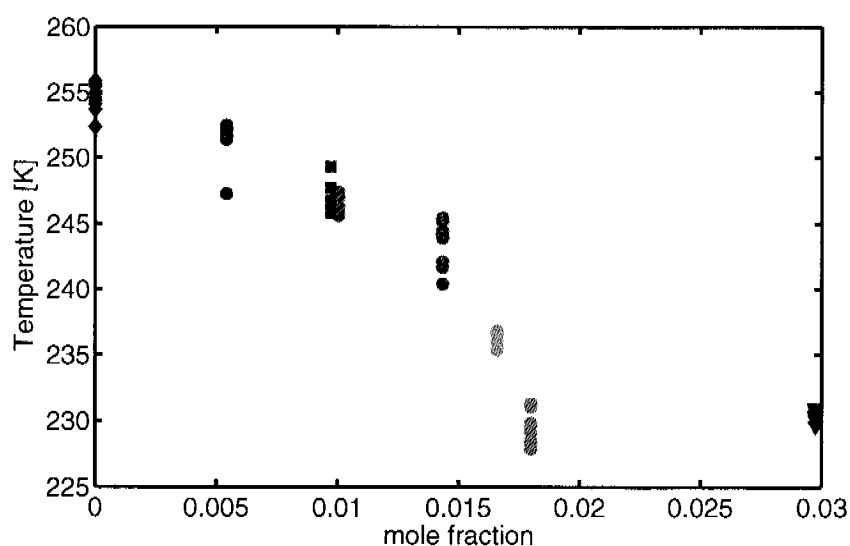


Figure 4.10: Heterogeneous freezing points of large droplets with suspended SiO_2 as a function of mole fraction of the solution. The concentration of SiO_2 globules is in all experiments 0.47 wt%. Blue diamonds: water; Blue, red, green, cyan and magenta bullets: 7.73, 15.73, 25.44, 32.67 and 38.90 wt% $(\text{NH}_4)_2\text{SO}_4$; Blue squares: 10.83 wt% H_2SO_4 ; Blue triangles: 14.90 wt% LiCl .

4.2.4 Dicarboxylic acids

Dicarboxylic acids have been detected in various regions of the atmosphere, namely in marine region (Kawamura and Sakaguchi, 1999), in urban sites (Kawamura and Ikushima, 1993), in Arctic aerosols (Narukawa et al., 2003a), in the free troposphere (Narukawa et al., 2003b) and also as a product of biomass burning (Graham et al., 2002). In terms of abundances, the largest fraction of dicarboxylic acids in the condensed phase is usually oxalic acid followed by malonic and succinic acid. Several laboratory studies have inves-

tigated the hygroscopic behavior of the pure acids (Parsons et al., 2004) and internally mixed inorganic/organic particles (Brooks et al., 2002; Wise et al., 2003) as well as the influence of organics on the homogeneous ice nucleation (Prenni et al., 2001; Wise et al., 2004; Kärcher and Koop, 2005). In a recent study, Parsons et al. (2004) concluded that several solid dicarboxylic acids are not good IN in the deposition mode above 243 K. The solid acids did not nucleate ice, but rather underwent deliquescence to form metastable solutions. Here, the possible role of crystalline dicarboxylic acids to act as IN immersed in aqueous solutions is investigated. Following Marcolli et al. (2004b), the focus was kept on oxalic, succinic, adipic, fumaric and phthalic acids, as these have abundance-to-solubility ratios suitable for the formation of solids under atmospheric conditions.

Figure 4.11 shows DSC heat flow curves for a typical experimental run with an aqueous solution of 4.95 wt% oxalic acid. First the sample was cooled with a constant cooling rate (10 Kmin^{-1}) until the droplets in the emulsion froze (first cycle, solid red line). The sample was then heated up with 1 Kmin^{-1} (solid blue line) to a temperature, which is termed the conditioning temperature. This temperature was chosen to be above the eutectic melting point of ice and oxalic acid dihydrate, but below the melting point of oxalic acid dihydrate (OAD). Then the sample was cooled again with the same cooling rate (second cycle, dashed red line), until freezing occurred. Finally, the probe was heated above the conditioning temperature, so that in addition to the eutectic melting also the melting of the oxalic acid was observed (zoomed area of the dashed blue line).

Pure aqueous dicarboxylic acids

The measurements of the dicarboxylic acid/water systems are summarized in Tab. 4.4, whereas mean values of several emulsions are given for the freezing and melting temperatures. The concentrations of the organic acids have been chosen to cover the atmospherically relevant range and/or to force crystallization of the organic species. Literature values of the saturation concentrations listed in Tab. 4.4 show that the dicarboxylic acid solutions are close to or slightly above saturation at room temperature. As seen in Tab. 4.4, for all, but the least concentrated oxalic acid solutions, as well as for the succinic and adipic acid solutions, the freezing of ice occurred in the first cycle at lower temperature than in the second cycle. This temperature difference may be due to two reasons. First, the crystallized dicarboxylic acid might act as a heterogeneous ice nucleus. Second, the concentration of the dicarboxylic acid is reduced to the saturation level in the presence of crystallized dicarboxylic acid. The second effect is more pronounced the higher the initial concentration is. Therefore the second freezing temperature must be actually compared with a reference measurement of a dicarboxylic acid solution that is just saturated at the ice freezing temperature. This temperature difference is denoted as ΔT_{het} . Since the solubilities of the dicarboxylic acids at around 235 K are extremely small (e.g., saturation concentration of oxalic acid at 236 K is around 0.35 wt%, based on a thermodynamical

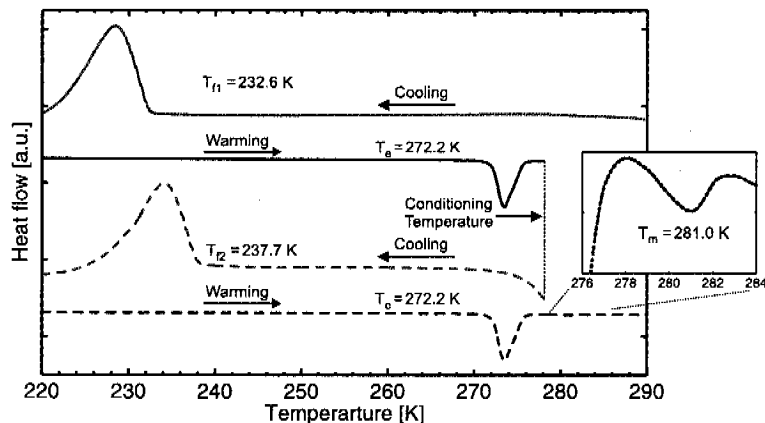


Figure 4.11: DSC heat flow measurements of a 4.95 wt% oxalic acid/water solution representing a typical experiment. The curves belong to different cooling/heating cycles and are shifted vertically for clarity. Solid red line: first cooling cycle with homogeneous freezing of the oxalic acid solution, i.e. formation of ice and oxalic acid dihydrate. Solid blue line: first heating cycle with endothermic peak arising from eutectic melting of ice (T_e). Dotted black line: conditioning temperature. Dashed red line: second cooling cycle with T_{f2} indicating the heterogeneous freezing temperature. Dashed blue line: second heating cycle again showing eutectic melting (T_e) and further an additional melting peak (T_m) at 281 K. (zoomed insert with a 40-times enhanced resolution) due to melting of oxalic acid dihydrate (OAD).

extrapolation of data at higher temperature), pure water is chosen as the reference. This is a conservative estimate, as the small error induced by this procedure leads to a slight underestimation of the nucleation potential of the organic ice nucleus. In summary, a specific dicarboxylic acid acts as a heterogeneous ice nucleus when the freezing temperature of the second cycle is higher than the homogeneous freezing temperature of pure water. For all but the least concentrated oxalic acid/water samples, ΔT_{het} lies in the range of 1.8–2.0 K, showing that solid oxalic acid acts as a heterogeneous ice nucleus in the immersion mode. Since no other exothermic peak is found in the freezing curves and considering also the melting point in the last heating cycle at 281 K of Fig. 4.11, solid oxalic acid must have formed in the first cycle along with or triggered by ice formation. The solid is assumed to precipitate as oxalic acid dihydrate (Braban et al., 2003), which from now on will be denoted as OAD. Heterogeneous nucleation is not observed for the least concentrated oxalic acid solution. From the eutectic concentration of OAD with ice of about 3 wt%, it follows indeed that no solid compounds remained in the droplets after the first heating cycle. Therefore the freezing temperatures of both cycles are identical and the measured endothermic peak does not indicate eutectic but regular ice melting. Melting and eutectic points of these solutions are in good agreement with Braban et al. (2003), who investigated aerosol phase transitions (deliquescence and efflorescence) and bulk solution properties of these aqueous solutions, but not their ice nucleation potential. The concentrations of the

Table 4.4: Summary of experiments with binary dicarboxylic acid/water systems. C_{DA} and C_{sat} are the concentrations of the sample and the saturation concentration at a specific temperature. T_c denotes the conditioning temperature. T_{f1} and T_{f2} are the freezing temperatures of the first and second cycle, respectively (see Fig. 4.11). Literature data of melting points (T_m) are given in brackets. IN indicates whether heterogeneous ice nucleation was observed or not.

Solute	C_{DA} [wt%]	C_{sat} [wt%]	T_c [K]	T_{f1} [K]	T_m^* [K]	T_{f2} [K]	IN
pure water	–	–	–	235.9	273.2	235.9	–
Oxalic acid	2.50	4.46 at 278.15 K [†]	279	234.1	272.6 (272.5 ^{&})	234.1	no
Oxalic acid	4.95	8.69 at 293 K [#]	279	232.3	272.2 (272.5 ^{&})	237.7	yes
Oxalic acid	9.76	9.81 at 298 K [#]	279	229.6	272.2 (272.5 ^{&})	237.7	yes
Oxalic acid	19.87		279	222.9	272.2 (272.5 ^{&})	237.9	yes
Succinic acid	7.31	7.7 at 298 K [#]	277	232.0	272.6 (273.2 [§])	233.9	no
Adipic acid	1.61	1.4 at 288 K [#]	279	234.6	272.6 (273.2 [§])	235.1	no
Phthalic acid	0.63	0.54 at 287 K [#]	279	235.5	272.6	235.6	no
Fumaric acid	0.50	0.499 at 293 K [#]	279	234.9	272.6	234.9	no

*The melting point is either the eutectic or the ice melting point, [†]Apelblat and Manzurola (1987),
[#] Stephen and Stephen (1963), & Braban et al. (2003), [§]Parsons et al. (2004)

oxalic acid in the solutions, and hence the surface area of the solid OAD, are varied over a considerable range: assuming a spherical nucleus, the surface of OAD of the most concentrated solution is larger by a factor of 2.4 than in the 4.95 wt% solution. Nevertheless, the freezing temperatures of the second cycles differ by just ~ 0.2 K, which is less than the variability caused by differences between emulsions. Therefore, one can conclude that the heterogeneous rate coefficient under these freezing conditions must be a very steep function of temperature, which is not unusual for ice nucleation processes and has been found for heterogeneous ice nucleation on AgI surfaces, SiO₂ globules or the surface of the aluminum surface of the DSC pan.

The freezing points of the second cycles of the other dicarboxylic acids are all lower than the reference measurement with pure water, indicating that heterogeneous nucleation is inefficient and that the freezing point depression due to higher solution concentration is responsible for the change of freezing temperatures between the first and the second cycles. Two cases can be distinguished. First, succinic and adipic acid show a similar behavior as oxalic acid with a clear temperature difference between the first and second cooling cycles. Hence, succinic and adipic acid must have crystallized, although their melting points could not be detected when the samples were heated above the conditioning temperature at the end of the experiment. This is also expected in the case of adipic acid as the endothermic peak is smaller than the resolution of the DSC. In a recent study, Parsons et al. (2004)

concluded that succinic and adipic acid are not good IN above 243 K in the ice deposition mode. From both data sets together, we conclude, that these solid acids are unlikely to play any role in heterogeneous ice nucleation in the atmosphere, neither in deposition nor in immersion mode. In the case of phthalic or fumaric acid the difference of the freezing temperatures between the two cycles are negligible small because of the low initial concentrations, but since both acids are supersaturated substantially during ice formation, we may nevertheless assume that the acids have crystallized. With the chosen concentrations these nuclei would not melt at the conditioning temperature. Hence, also phthalic and fumaric acid are unlikely to act as IN under atmospheric conditions.

In summary, out of these five candidates only solid oxalic acid is active as an ice nucleus. However, under atmospheric conditions solid oxalic acid nuclei will rarely occur in pure water, but in aqueous solutions together with other organic or inorganic species.

Oxalic acid/aqueous solutions systems

For the oxalic acid/aqueous solutions systems the same experimental procedure was used as for the pure dicarboxylic acid solutions, with suitable choices for reference samples. Measurements were performed with different inorganic and organic aqueous solutions, all containing various amounts of oxalic acid (Tab. 4.5). The exact composition of the solutions in equilibrium with OAD is not known generally. This problem can be overcome by distinguishing two cases. If the concentration of the oxalic acid is negligible small compared to the additional solute, the concentration of the reference sample can be taken as the composition of the initial solution without the oxalic acid. (e.g., solution of interest: 14.9 wt% NaCl/0.5 wt% oxalic acid, reference solution: 14.9 wt% NaCl). However, if oxalic acid constitutes a substantial part of the total solute, a considerable error would be introduced by the above procedure. After the crystallization of the OAD in the first cycle, most of the oxalic acid and a minor part of water are withdrawn from the solution. Consequently, the sample is more highly concentrated with respect to the additional solute. Therefore the concentration of the reference sample was adjusted for each investigated solution assuming that upon crystallization of OAD no oxalic acid is left in the solution (e.g., solution of interest: 40.0 wt% Malonic acid/4 wt% oxalic acid, reference solution: 42.7 wt% Malonic acid).

Aqueous NaCl/oxalic acid

The solubility of oxalic acid is drastically decreased in a highly concentrated NaCl solution. While the solution with 0.1 wt% oxalic acid and 14.9 wt% NaCl is not yet saturated at room temperature, those with 0.33 and 0.5 wt% oxalic acid and 14.9 wt% NaCl are supersaturated, see Tab. 4.5. Consequently these two solutions had to be placed in a

Table 4.5: Summary of measurements for oxalic acid/aqueous solution systems together with the corresponding reference measurements. The following abbreviations are used for the solutes: Oxalic acid (OA), Malonic acid (MA), $(\text{NH}_4)_2\text{SO}_4$ (AS), H_2SO_4 (SA) and NH_4HSO_4 (ABS). C_{sol} and C_{OA} indicates the total concentrations in wt% of the solute and the oxalic acid, respectively. T_{f1} and T_{f2} are the freezing temperatures of the first and second cycles, respectively. IN indicates whether OAD was crystallized or not. T_{m} indicates the ice melting point of the aqueous solution; the corresponding literature values are given in brackets. All temperature values are given in Kelvin.

Oxalic acid/aqueous solution systems							Reference measurements			
Solute	C_{sol}	C_{OA}	T_{f1}	T_{m}	T_{f2}	IN	C_{sol}	T_{f}	T_{m}	ΔT_{het}
NaCl	14.9	0.1	216.4	262.1	216.4	no	14.9	216.9(215.7) [†]	262.2(262.1) [†]	-0.5
NaCl	14.9	0.33	216.4	262.0	221.7	yes	14.9	216.9(215.7) [†]	262.2(262.1) [†]	4.8
NaCl	14.9	0.5	215.9	262.0	221.3	yes	14.9	216.9(215.7) [†]	262.2(262.1) [†]	4.4
MA	10.0	4.0	228.4	270.5	233.5	yes	10.7	230.5	271.2(271.3) [#]	3.0
MA	20.0	4.0	223.1	268.2	228.9	yes	21.4	225.0	268.8(268.9) [#]	3.9
MA	30.0	4.0	215.2	264.8	222.1	yes	32.1	217.8	265.5(265.2) [#]	4.3
MA	40.0	4.0	204.2	259.7	212.9	yes	42.8	207.9	260.1(260.9) [#]	5.0
AS	4.0	4.0	230.3	271.8	232.3	no	4.27	232.8(232.3) ^{&}	271.9(271.9) [§]	-0.5
AS	30.0	3.0	212.1	262.8	213.2	no	31.8	210.6(210.7) ^{&}	261.0(261.7) [§]	2.6
ABS	4.0	4.0	230.5	271.5	232.3	no	4.27	232.0(230.7) [¶]	271.9(271.7) [§]	0.3
SA	4.0	4.0	229.4	271.0	234.7	yes	4.27	231.3(231.8) [‡]	271.4(271.3) [§]	3.4
SA/ABS	2.0/2.0	4.0	230.0	271.2	234.6	yes	2.13/2.13	232.1	271.90(271.7) [§]	2.5

[†]Rasmussen and MacKenzie (1972), [#]Hansen and Beyer (2004), [&]Bertram et al. (2000), [§]Clegg et al. (1998), [‡]Koop et al. (1998), [¶]Koop et al. (1999)

water bath at ~ 320 K before the emulsions could be prepared. The freezing temperatures of the first and the second cycles are identical for the weakest concentrated solution and thus no solid oxalic acid exists in the droplets after the first heating cycle. The other two solutions show the same behavior as the binary oxalic acid/water system. Namely, the freezing points of the second cycles are clearly higher ($\Delta T_{\text{het}} \sim 4.5$ K) than the one of the reference measurement with a 14.9 wt% NaCl solution. (Again, ΔT_{het} does not depend on the oxalic acid concentration. The melting peak of the solid oxalic acid is smaller than the resolution of the DSC and could not be observed at the end of the experiment.)

Aqueous Malonic acid/oxalic acid

For the malonic/oxalic acid solutions, the concentrations of malonic acid are varied from 10 to 40 wt%, whereas the oxalic acid concentration was kept at 4 wt%. None of these solutions are supersaturated at room temperature. Heterogenous ice nucleation by the oxalic acid is observed in all experiments. ΔT_{het} varied between 3.0 and 5.0 K, whereby the

largest effect was observed for the most concentrated malonic acid solution. The melting of the solid oxalic acid has been identified in all measurements, whereby the melting temperatures increase with increasing concentration of the malonic acid, indicating that the presence of malonic acid decreases the solubility of oxalic acid in the sample.

Aqueous $(\text{NH}_4)_2\text{SO}_4$ /oxalic acid and NH_4HSO_4 /oxalic acid

In the presence of $(\text{NH}_4)_2\text{SO}_4$ (AS) and NH_4HSO_4 (ABS) the solubility of oxalic acid is strongly reduced. The stock solution had to be put in a hot water bath for full dissolution. Overnight crystals slowly formed again, when the solutions were kept at room temperature. Nevertheless, the temperature difference between the first and the second freezing cycle are in accordance with a homogeneous freezing process. ΔT_{het}^i is approximately zero for the 4 wt%/4 wt% AS/oxalic acid and the 4 wt%/4 wt% ABS/oxalic acid systems. The positive value for the 30 wt%/3 wt% AS/oxalic acid solution can not be considered as an indication of heterogeneous freezing since also the melting point is elevated by 1.5 K compared with the reference measurement. Nevertheless a solid phase must have formed based on the increase in freezing temperature between the first and the second freezing cycle and the elevated melting temperature. This solid phase is not active as a heterogeneous ice nucleus and should therefore be different from OAD. To confirm this hypothesis the elemental composition of the crystals that crystallized from the stock solution was determined by elemental analysis (C,H,N,S,O and H_2O). The absence of sulfur and relative ratio of the other elements indicates that this new phase consists of ammonium, oxalic acid and water in a ratio of 1:2:2. This ammoniumbioxalate-oxalic acid hydrate might be the prevalent crystalline phase of oxalic acid in the atmosphere under neutral and moderately acidic conditions. Elemental analysis was performed at Solvias AG (Basel, Switzerland) by pyrolysis methods (C,H,N,S,O). The water content was determined by Karl Fischer titration.

Aqueous H_2SO_4 /oxalic acid and H_2SO_4 / NH_4HSO_4 /oxalic acid

Since at cirrus cloud altitudes aerosols can be very acidic, we investigated acidic solutions with sulfuric acid (SA) and a mixture of SA and ABS. For the chosen concentration of sulfuric acid, we found no evidence of any deterioration of the emulsions. The ΔT_{het}^i values clearly show that heterogeneous nucleation occurred. Therefore OAD must have crystallized under these acidic conditions.

4.2.5 Miscellaneous IN

Within this thesis two other IN have been investigated in the immersion mode, namely Fe_3O_4 (magnetite) nanopowder and Al_2O_3 nanoparticles. Both chemicals were purchased from Fluka. The mean diameter of the dispersed Al_2O_3 particles are smaller than 20 nm. Emulsions as well as large droplets of such suspensions have been investigated in the DSC. Emulsions made of a Al_2O_3 suspension do not behave differently to emulsions with pure water (Fig. 4.12a). The onset freezing temperatures of both emulsions are within 0.25 K, which is smaller than the temperature uncertainty in emulsion experiments. Figure 4.12b) depicts the freezing points of large droplets ($V=3 \mu\text{l}$) for two data series, made of either a 10 wt% Al_2O_3 nanoparticles suspension or pure water, respectively. The series of the droplets are not distinguishable with the Wilcoxon ranksum test ($p=0.1164$, $h=0$, 5% level). Therefore, together with the comparison of the experiments with the emulsions, one can conclude that these dispersed Al_2O_3 nanoparticles do not act as a heterogeneous IN in the immersion mode. The results with the Fe_3O_4 nanopowder are similar to those with the Al_2O_3 nanoparticles, besides the fact that the suspended magnetite particles sediment even quicker to the bottom of the test tube. Thus also Fe_3O_4 particles are inefficient as an IN in the immersion mode. Thus experiments with various aqueous solutions were not continued for both. On the other hand Archuleta et al. (2005) have shown recently, that both Al_2O_3 and Fe_2O_3 induce ice nucleation in the deposition mode, indicating that particles might have different IN efficiency in different ice nucleation modes.

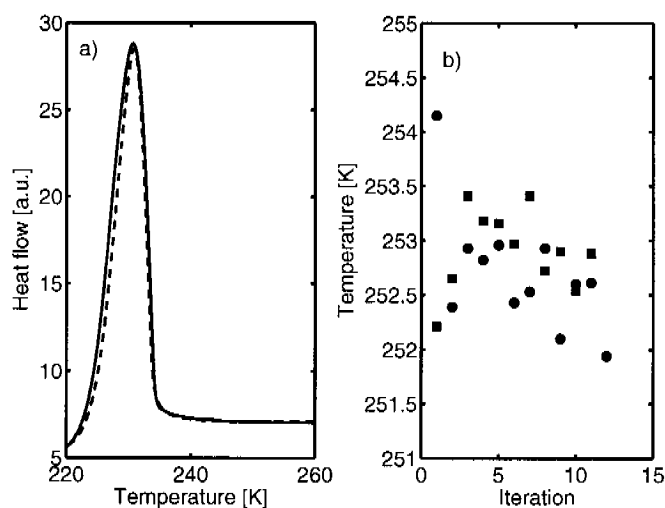


Figure 4.12: Comparison between emulsions (panel a) and large droplets (panel b) containing Al_2O_3 nanoparticles and pure water, respectively. solid line and bullets: 10 wt% Al_2O_3 nanoparticles solution; dashed line and squares: pure water.

4.3 Water activity based ice nucleation theory for heterogeneous ice nucleation

The investigated heterogeneous freezing points with different IN show in general a similar picture. Besides the notable scatter in the freezing temperature for equally prepared samples, the freezing temperatures of various solutions are widely spread as a function of mole fraction of the solution. Therefore, the water activity based nucleation theory was used to combine the experiments with the different IN. The water activity, a_w , of any aqueous solution can be determined at its ice melting point with (Eq. 2.26). In a first attempt, it is assumed that the water activity of each sample is independent of temperature, i.e., a_w at T_f is equal to a_w at T_m . This was shown to be a rather good approximation for most common solutes (Koop et al., 2000).

Figure 4.13 depicts heterogeneous ice freezing temperatures for various IN as a function of water activity (see also Tab. C.1, C.2 and C.3). The median freezing temperatures were chosen for large series of individual single droplets, whereas the mean freezing temperature was used for different emulsions made of the same initial solution. Also shown as colored lines are curves which were constructed by horizontally shifting the ice melting curve such that the new curve fits the $T_{f,het}$ points at $a_w=1$ for each ice nucleus. The freezing points for the different IN show in general a consistent picture, namely that $T_{f,het}$ is decreasing with decreasing water activity, similar to homogeneous ice nucleation (solid black line). This is rather surprising, because various aqueous solutions with different IN are compared with each other. The only analogousness for all experiments is the nucleation pathway, namely the immersion mode. It is further obvious that the different data series exhibit uneven scatters around the colored curves and that the scatter increases for smaller a_w values. As mentioned before, Koop (2004) found that homogeneous ice freezing points of 18 different aqueous solutions are spread within a 5% deviation of the homogeneous ice freezing curve. With a simple model, the author concluded, that a slight change in water activity as a function of temperature may be the most probable explanation. This phenomenon is indeed confirmed by a_w measurements or model studies for several substances such as NH_4NO_3 , H_2SO_4 and poly(ethylene glycol), above the ice melting point curve (e.g., Clarke and Glew, 1985; Clegg et al., 1998; Eliassi et al., 1999). Because of the uneven scatter of the different data series and the different nature of the IN, the series are discussed in a second step separately.

For solutions with OAD and AgI, measurements of homogeneous ice freezing points have been measured as well. Therefore, one can try to compare the scatter in the homogeneous and the heterogeneous freezing points individually to search any systematic trend. Panels a and c of Fig. 4.14 depict the homogeneous and heterogeneous freezing points of AgI and OAD, respectively, as a function of water activity. The same symbols and color code as in Fig. 4.9 is used. The solid black lines in Panel a and c show the prediction of homogeneous

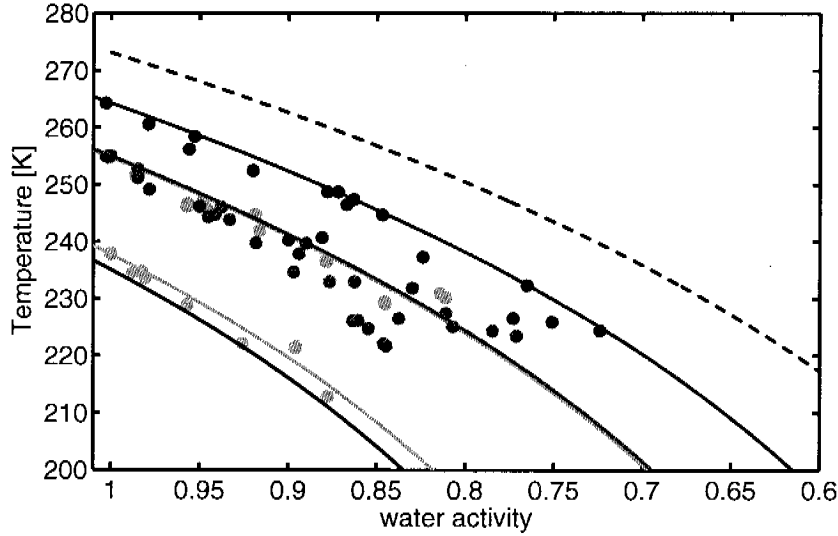


Figure 4.13: Median (blue and green) or mean (red and cyan) heterogeneous freezing points of different aqueous solutions with various IN as a function of water activity. The points correspond to the following IN: Blue: nonadecanol; Green: SiO_2 ; Red: AgI; Cyan: OAD. Dashed and solid black lines: Ice melting and homogeneous ice freezing curves (Koop et al., 2000). Colored lines: horizontally shifted curves of the dashed black line with a constant Δa_w , which are chosen to fit the points at a_w equal to one best.

ice nucleation temperatures based on Koop et al. (2000). The two dashed black lines in Fig. 4.14 depict a $\pm 5\%$ deviation from the solid black line. All the measured homogeneous freezing points are located within this area. Figure 4.14a also indicates, that the scatter of homogeneous and heterogeneous freezing is not random, but a correlation exists between the two quantities. For example, the two cyan diamonds at about $a_w = 0.77$ deviate most in the heterogeneous as well as in the homogeneous mode. Figure 4.14c shows a similar picture for OAD, but with a less pronounced scatter for both curves.

In the following paragraph, these systematic deviations will be analyzed. A horizontal offset with respect to the ice melting point curve can be determined for any individual heterogeneous freezing point, $\Delta a_w(T_{f,\text{het}})$, and homogeneous freezing point, $\Delta a_w(T_{f,\text{hom}})$, by evaluating

$$\Delta a_w(T_{f,\text{het}}) = a_w(T_f) - a_w^i(T_{f,\text{het}}) \quad (4.1)$$

and

$$\Delta a_w(T_{f,\text{hom}}) = a_w(T_f) - a_w^i(T_{f,\text{hom}}), \quad (4.2)$$

where $a_w(T_f) \approx a_w(T_m)$ is the water activity at the freezing point determined from the measured ice melting point, and $a_w^i(T_{f,\text{het}})$ and $a_w^i(T_{f,\text{hom}})$ are the water activities on the

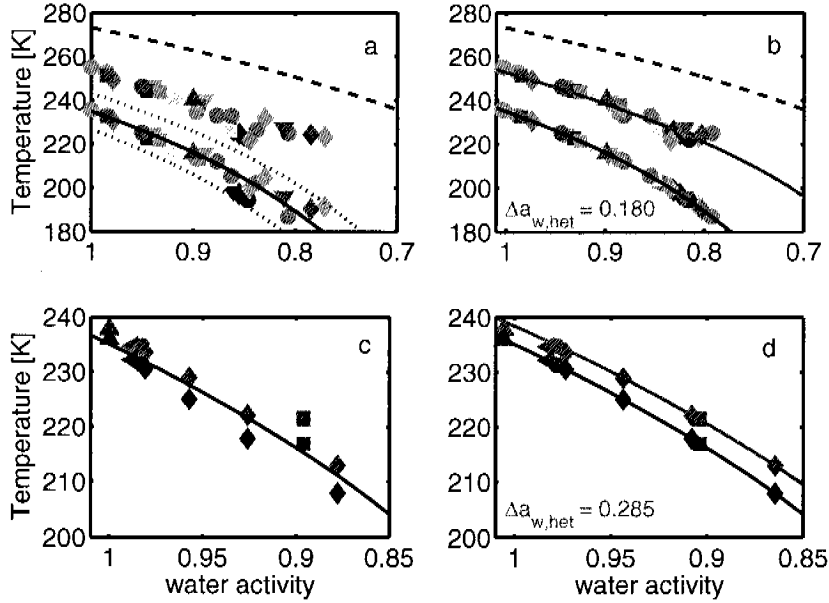


Figure 4.14: Panel a and c depict heterogeneous (upper symbols) and homogeneous (lower symbols) freezing points for different aqueous solutions with immersed AgI and OAD as a function of a_w , respectively. Symbols of the same colored at a certain a_w value correspond to each other. Dashed and solid black lines: Ice melting and homogeneous ice freezing point lines, respectively. Dotted black lines: 5% deviation of the solid black line. Panel b and d: Same data as in a and c, respectively, but the homogeneous freezing points are placed onto the homogeneous freezing point line (black line) and the resulting a_w is adapted also for the heterogeneous freezing points. Red lines, horizontally shifted curves of the dashed black line with a $\Delta a_{w,hct}$ of 0.180 and 0.285, respectively.

ice melting point curve at the heterogeneous and homogeneous freezing temperature, respectively. Subtracting Eq. 4.1 from Eq. 4.2 defines the corresponding difference in water activity, δa_w , between each pair of heterogeneous/homogeneous ice freezing points:

$$\delta a_w = \Delta a_w(T_{f,hom}) - \Delta a_w(T_{f,hct}) \quad (4.3)$$

Since the exact value of $a_w(T_f)$ is unknown, a small change in water activity of a solution with decreasing temperature by adjusting $a_w(T_f)$ is allowed, such that all measured homogeneous freezing points fall onto the water-activity-based homogeneous freezing line predicted by Koop et al. (2000). Technically this can be achieved by defining a $\Delta a_{w,hct}$ which can be calculated for each measured heterogeneous freezing point by

$$\Delta a_{w,hct} = \Delta a_{w,hom} - \delta a_w, \quad (4.4)$$

where $\Delta a_{w,hom} = 0.305$ (Koop et al., 2000).

Figures 4.14b and 4.14d depict the same data points as in Fig. 4.14a and 4.14c, but this time all homogeneous freezing points are forced onto the homogeneous ice freezing point line of Koop et al. (2000) and the resulting water activity values are then also adapted for the heterogeneous freezing points. The two red lines depict a calculated mean values for all individual obtained $\Delta a_{w,\text{het}}$ values of a specific heterogeneous freezing points. The scatter of the heterogeneous freezing points is almost (Fig. 4.14b) and nearly completely (Fig. 4.14d) eliminated.

For the two series of large droplets covered with nonadecanol and immersed SiO_2 globules, the homogeneous freezing points are neither measured nor known from literature. Hence, the upper comparison can not be performed, but $\Delta a_{w,\text{het}}$ can also be estimated for both series with Eq. 4.4. Figure 4.15 depicts the heterogeneous freezing points as function of the corrected (AgI and OAD) and the measured (nonadecanol and SiO_2) water activity values. From this figure one can conclude, that heterogeneous ice freezing temperatures of aqueous solutions with an immersed ice nucleus can be described similarly to homogeneous ice nucleation with a constant $\Delta a_{w,\text{het}}$ for each specific ice nucleus.

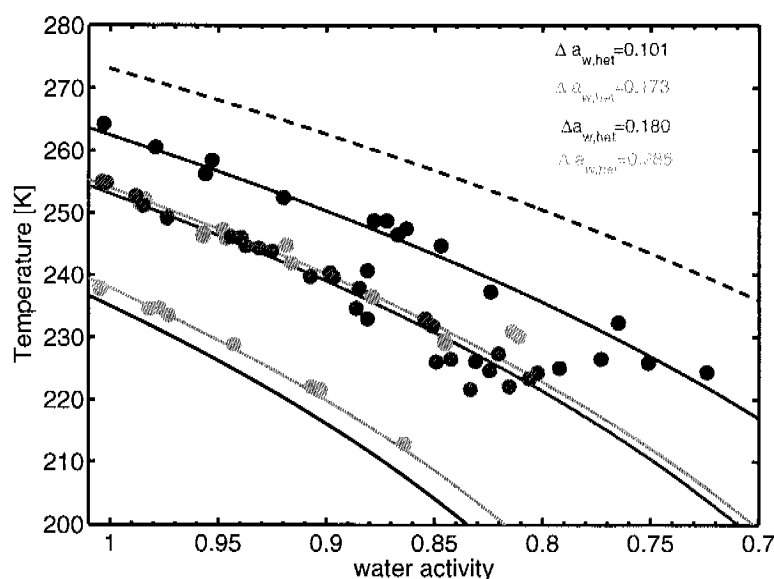


Figure 4.15: Heterogeneous freezing points of various IN as a function of corrected a_w values. The data are the same as in Fig. 4.13, but the a_w values are corrected for the AgI and OAD series. For each data series, a best $\Delta a_{w,\text{het}}$ is estimated: Nonadecanol: 0.101, SiO_2 : 0.173, AgI: 0.180 and OAD: 0.285. Note that the $\Delta a_{w,\text{het}}$ for small droplets covered with nonadecanol or with immersed SiO_2 globules would distinctly differ from the above values.

λ -approach

Another common approach to deal with homogeneous freezing points of various aqueous solutions is to compare ΔT_f , the supercooling of the homogeneous freezing point T_f ($\Delta T_f = T_{f,0} - T_f$) with the equilibrium melting point depression ($\Delta T_m = T_{m,0} - T_m$) (e.g., Rasmussen and MacKenzie, 1972; Rasmussen, 1982). $T_{f,0}$ and $T_{m,0}$ are the homogeneous ice freezing and ice melting points of pure water, respectively. From experimental data, Rasmussen and MacKenzie (1972) found that ΔT_f is a linear function of ΔT_m for each solute.

$$\Delta T_f = \lambda \cdot \Delta T_m. \quad (4.5)$$

Together with other measurements, DeMott (2002) suggested, that λ values of 1.4 to 2.2 can express the data of aqueous solutions made of salts, acids, and simple molecules. On the other hand, λ for aqueous poly(ethylene glycol) and poly(vinyl pyrrolidone) solutions can show values of up to 5 (Rasmussen and MacKenzie, 1972; Rasmussen et al., 1975; Zobrist et al., 2003), indicating that λ can strongly depend on the nature of the solute. Thus, homogeneous ice nucleation can not be generalized without the knowledge of the solute specific parameter λ . Nevertheless, DeMott (2002) suggested that a similar parameterization might also be possible for heterogeneous ice nucleation.

$$T_{f,\text{het}} = T_{f0,\text{het}} + \lambda \cdot \Delta T_m, \quad (4.6)$$

where, $T_{f,\text{het}}$ and $T_{f0,\text{het}}$ are the heterogeneous freezing temperature of the aqueous solutions and of pure water with the same ice nucleus, respectively. It was suggested that the variable parameter $T_{f0,\text{het}}$ describes primarily the role of the insoluble substrate, i.e., capturing the effect of size and of the insoluble particle composition, whereas λ is insensitive to the nucleation process (Archuleta et al., 2005). Table 4.6 shows λ and $T_{f0,\text{het}}$ values for the four investigated IN in this study and data from two other studies (Zuberi et al., 2002; Archuleta et al., 2005). Since all experiments were performed in the immersion mode, one has the chance to compare the different data sets with each other. Note that just a mean λ -value for the different solutes for each ice nucleus is taken. The heterogeneous freezing temperature of the specific ice nucleus in pure water is adopted for $T_{f0,\text{het}}$. λ is estimated with the least square root deviation method, and varies between 1.28 and 1.78. The largest value for λ is found for the lowest $T_{f0,\text{het}}$. Further, two of the estimated λ 's are somewhat smaller than the predicted range for homogeneous ice nucleation. Zuberi et al. (2002) estimated λ as 1.7 for heterogeneous freezing points of aqueous $(\text{NH}_4)_2\text{SO}_4$ solutions with immersed kaolinite and montmorillonite particles. And in recent FTIR study, λ was determined as 1.1 to 1.9 for aluminum oxide, alumina silicate and iron oxide particles (Archuleta et al., 2005). The authors concluded, that just one obtained λ differs from the suggested range of λ for homogeneous ice nucleation. Since also in this study λ is smaller than the lower limit for homogeneous nucleation, it seems likely that this

Table 4.6: λ and $T_{f0,het}$ values for nonadecanol, SiO_2 , AgI, OAD (all this study), kaolin-ite/montmorillonite(KM,DSC study) (Zuberi et al., 2002), aluminum oxide, alumina silicate and iron oxide particles (continuous-flow diffusion chamber study) (Archuleta et al., 2005). In all experiments, the droplets are nucleated in the immersion mode. The number in the brackets indicates the size of the ice nucleus. In this study, $T_{f0,het}$ is adopted as the heterogeneous freezing points of pure water of a specific ice nucleus. λ is estimated with the least square root deviation.

IN	$T_{f0,het}$ [K]	λ
Nonadecanol	264.25	1.28
SiO_2	254.6	1.34
AgI	255.00	1.51
OAD	237.7	1.78
KM	242.21	1.7
Al_2O_3 (100 nm)	234	1.5
Al_2O_3 (200 nm)	244	1.6
$3Al_2O_3 \cdot 2SiO_2$ (100 nm)	230	1.1
$3Al_2O_3 \cdot 2SiO_2$ (200 nm)	247	1.9
Fe_2O_3 (50 nm)	233	1.4
Fe_2O_3 (100 nm)	238	1.4
Fe_2O_3 (200 nm)	244	1.4

parameter can not be treated as insensitive to the fundamental nucleation process as it was suggested by DeMott (2002). However, the data of Zuberi et al. (2002) together with this study indicate that λ is increasing for decreasing $T_{f0,het}$, emphasizing that these two parameter are directly linked with each other.

Figure 4.16 shows a comparison of the λ -approach with the water activity based nucleation theory. The general agreement of the two approaches is very good, when compared to the large scatter of the measured freezing points. Thus, solely from the fit quality, one can not distinguish which approach is more favorable. The λ -approach has two unknown parameters (λ and $T_{f0,het}$), whereas the water activity based theory has just one. However, actually there would be for any solute a slightly different λ . One has to consider that both approaches are semi-empirical and thus the entire physics of the ice nucleation process are not fully covered in either approach. However, there is a reason, which favor the water activity based nucleation theory over the λ -approach, namely there exists a direct link to atmosphere by the water activity.

Let us consider a liquid droplet with an immersed ice nucleus that cools adiabatically in a rising air parcel. While the relative humidity is increasing, the droplet takes up water, and consequently grows and becomes more dilute. The water uptake of the aerosol, and thus its size and concentration are determined by the partial pressure of water in the gas

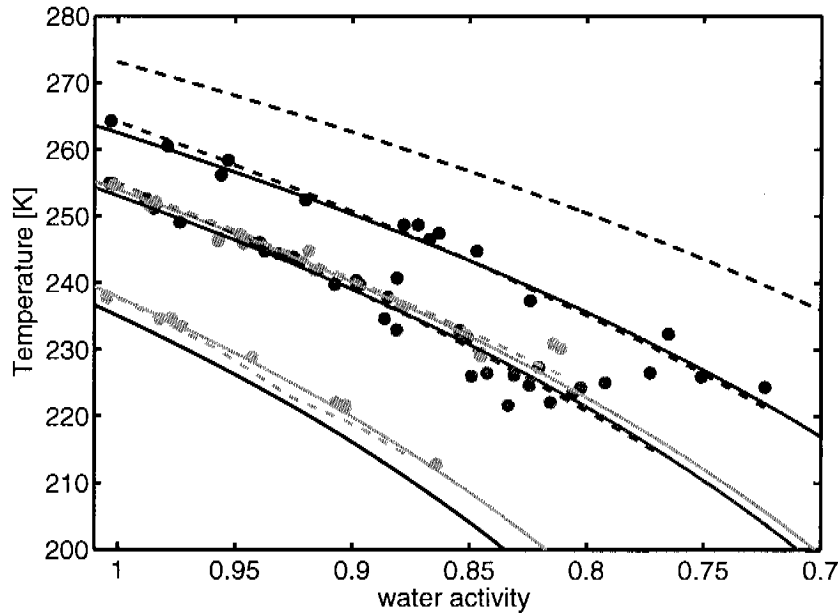


Figure 4.16: Comparison of water activity based nucleation theory versus the λ -approach. Colored bullets, solid lines and dashed lines: Measured heterogeneous freezing points, water activity based nucleation theory (see also Fig. 4.15) and λ -approach (see Tab. 4.6). Blue: Nonadecanol; Green: SiO_2 ; Red: AgI; Cyan: OAD.

phase and the water vapor pressure of the droplet. Assuming that the droplet and its gas phase are in equilibrium, a_w can be directly estimated from the relative humidity, which is often known from field campaigns (see Eq.2.28). Therefore, the water activity based nucleation theory is definitely more favorable than the λ -approach. Further, Koop et al. (2000) have shown, that besides the homogeneous freezing temperature, also a prediction of the homogeneous rate coefficient can be made with the water activity based nucleation theory.

4.4 Heterogeneous rate coefficients estimation from DSC freezing peaks

A freezing peak of an emulsion in DSC measurements represents the sum of $\sim 10^5$ single droplet freezing events. This statistical information of ice nucleation can be used to estimate an ice nucleation rate coefficient from such a freezing peak. Let us first consider the aspects which determine the shape and the size of a freezing peak resulting from a

homogeneously frozen emulsified aqueous solution sample. The shape and the area of a DSC freezing peak correlate with the cooling rate (i.e., a larger cooling rate leads to a larger peak area), the mass of the sample, the crystallization heat of ice, the size distribution in the emulsion and a time lag of the DSC. Because of this size distribution, the larger droplets will nucleate at slightly higher temperatures than smaller droplets. The freezing peak of a single droplet rises almost vertically at its freezing temperature, and then exhibits a considerable decay because of the time lag of the DSC. The released crystallization heat needs a certain time to be detected and thus balanced by the DSC, which results in the time lag. Therefore the freezing peak of an emulsion can be considered as the overlap of $\sim 10^5$ single droplets signals.

Figure 4.17 shows a DSC freezing peak of an emulsion made with pure water. The slow increase of the peak at ~ 239 K is due to the nucleation of a few larger droplets and a steep rise at ~ 236 K determines the freezing temperature of the emulsion. At ~ 233 K ($= T_{\max}$) the maximum of the heat flow signal is reached, and the curve follows a smooth decrease to ~ 223 K. However, the maximum of the freezing probability will be located at a higher temperature than T_{\max} . Based on the following assumptions, a mean nucleation rate of a single droplet within a time interval can be determined as follows: The total peak area for different emulsions can be enclosed by a temperature range of $T_{\max}-10$ K and $T_{\max}+5$ K (embedded area of the dotted black line together with the solid black line in Fig. 4.17), because the cooling rate is constant in all experiments and the size distribution for different emulsions is almost identical. The considered area to estimate the nucleation rate coefficient is chosen as that in which 2 (f_1) to 10% (f_2) of the total volume freezes (dashed area in Fig. 4.17). The total peak area is normalized to one. To determine the sizes of both areas, and consequently the start (T_1) and end temperature (T_2) of the considered interval, the time lag of the DSC has to be known. It is assumed that this decay follows an exponential curve. Following Pruppacher and Klett (1997) a mean homogeneous nucleation rate coefficient (j_{hom}) of a droplet with the volume V_{drop} within the time interval Δt can be calculated with:

$$j_{\text{hom}} = \frac{-\ln([1 - (f_2 - f_1)])}{V_{\text{drop}}\Delta t}, \quad (4.7)$$

whereas Δt can be expressed as

$$\Delta t = \frac{T_1 - T_2}{r_c}. \quad (4.8)$$

r_c is the cooling rate, which was 0.166 Ks^{-1} for all experiments. The shape of the exponential decay is described with a decay parameter τ , which has the same meaning as the life time in the radioactive decay. It was found that a value of 4 K fits the measurements best, but calculations with other values point out that the resulting j_{hom} is very insensitive to this parameter (see Tab. 4.7). The mean homogeneous nucleation rate coefficient for a droplet with a radius of $4 \mu\text{m}$ of the above freezing peak leads to a value of

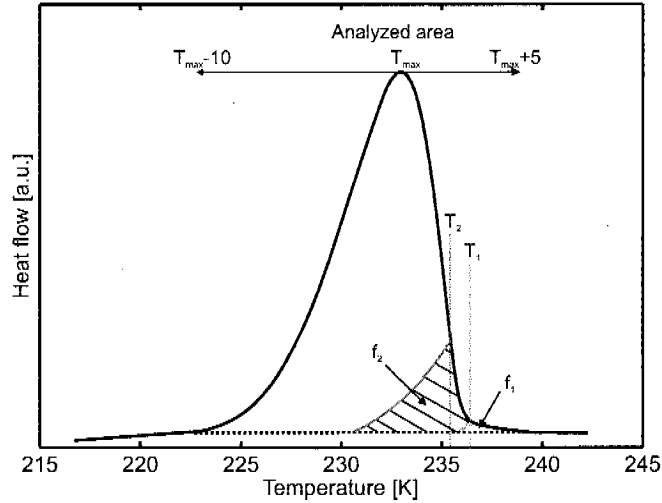


Figure 4.17: DSC freezing peak of a homogeneously nucleated emulsified water sample. The total analyzed area is shown with the two arrows. T_1 and T_2 indicate the start and end temperature of the considered area, in which a mean nucleation rate coefficient is estimated. The dashed area depicts the area in which 2% to 10% of the total volume is frozen. (See text for details)

$8.1 \cdot 10^7 \text{ cm}^{-3} \text{ s}^{-1}$ at a temperature of 236.0 K (T_{hom}). This temperature is ~ 0.15 K lower than T_1 determined by the onset of the freezing peak. j_{hom} , on the other hand, is ~ 1 - 2 orders of magnitude smaller compared to results shown in Pruppacher and Klett (1997), but this deviation reflects the typical uncertainty range of these measurements. Table 4.7 shows a sensitivity study for the two parameters τ and droplet radius (r_{drop}). Adding or subtracting two kelvins to the estimated τ results in reduction or enlargement of j_{hom} by $\sim 10\%$, respectively, indicating the insensitivity of j_{hom} to τ . On the other hand, j_{hom} doubles for a droplet radius of $3 \mu\text{m}$, which is in accordance to Koop (2004). Despite the fact that j_{hom} predictions of freezing peaks of emulsified samples lead to lower values than derived from other studies, the robustness of the analysis procedure is rather convincing. A mean heterogeneous nucleation rate coefficient for a droplet in emulsified samples can be calculated by substituting the droplet volume by the surface of the ice nucleus (S_{IN}) in Eq. 4.7. For this purpose the surface of the crystallized AgI and OAD have to be estimated in a single droplet. The volume of precipitated AgI in an emulsion droplet (V_{AgI}) can be expressed by:

$$V_{\text{AgI}} = \frac{V_{\text{drop}} \cdot \rho_{\text{drop}} \cdot wt_{\text{AgI}}}{\rho_{\text{AgI}}}, \quad (4.9)$$

where ρ_{drop} ($= 1.0 \text{ g cm}^{-3}$) and ρ_{AgI} ($= 5.68 \text{ g cm}^{-3}$, Lidc, 1998) are the densities of the aqueous droplet and AgI, and wt_{AgI} is weight percent of the AgI in the droplet, which can

Table 4.7: Sensitivity study of j_{hom} for different τ and r_{drop} values.

τ [K]	r_{drop} [μm]	T_{hom} [K]	j_{hom} [$\text{cm}^{-3}\text{s}^{-1}$]
4	4	236.0	$8.1 \cdot 10^7$
4	3	236.0	$1.9 \cdot 10^8$
4	5	236.0	$4.2 \cdot 10^7$
2	4	235.8	$8.7 \cdot 10^7$
6	4	236.2	$7.3 \cdot 10^7$
2	5	235.8	$4.5 \cdot 10^7$
6	5	236.2	$3.6 \cdot 10^7$
2	3	235.8	$2.1 \cdot 10^8$
6	3	236.2	$1.7 \cdot 10^8$
4	2	236.0	$6.5 \cdot 10^8$

be calculated as

$$wt_{\text{AgI}} = \frac{V_{\text{AgNO}_3} \cdot \frac{M_{\text{Ag}}}{M_{\text{AgNO}_3}} \cdot wt_{\text{AgNO}_3} + V_{\text{KI}} \cdot \frac{M_{\text{I}}}{M_{\text{KI}}} \cdot wt_{\text{KI}}}{V_{\text{aq}}}, \quad (4.10)$$

where V_{AgNO_3} , V_{KI} and V_{aq} are the volumes of the AgNO_3 , KI and the total aqueous solution, which are 0.1, 0.1 and 0.6 ml, respectively (blue preparation procedure). For the red preparation procedure the three values are 0.05, 0.05 and 0.5 ml, respectively. M_{Ag} , M_{AgNO_3} , M_{I} and M_{KI} are the Molar masses of Ag, AgNO_3 , I and KI, respectively. In the experiments, $wt_{\text{AgNO}_3} = 1.61$ and $wt_{\text{KI}} = 1.64$ are the used concentrations of the AgNO_3 and KI solutions in wt%, respectively.

As shown in Fig. 4.8, besides the heterogeneous freezing peak also the homogeneous freezing peak is always observed in experiments with precipitated AgI. A comparison of the sizes of these peaks indicates that approximately only half of the emulsion droplets nucleated ice heterogeneously. Therefore it seems reasonable to assume that only half of the calculated concentration in Eq. 4.10 contributes to heterogeneous nucleation. Further it is assumed that the precipitated AgI mass is proportional to the volume of the droplets. The radius of an AgI crystal adds up to $0.35 \mu\text{m}$ in a droplet with $r_{\text{drop}} = 4 \mu\text{m}$. Hence, the surface of the crystallite (S_{AgI}) yields $1.5 \cdot 10^{-8} \text{ cm}^2$ for the blue preparation procedure. Table 4.8 lists the calculated $j_{\text{het,AgI}}$ values for the experiments with emulsified samples containing solid AgI. Since the freezing peaks of a repeatedly investigated emulsion differ only slightly, just one j_{het} is calculated for such a series. All the experimentally determined $j_{\text{het,AgI}}$ values lie within 1 order of magnitude and since also S_{AgI} is not varying strongly, indicating that the heterogeneous nucleation rate for all emulsion has a similar magnitude. Note, the emulsion, with NaCH_3COO has the solute, which results in that minimum value for j_{het} has a rather weak increase in the DSC freezing peak. Further one has to add, because of the bad shape of the freezing peak of some emulsions, j_{het} could not

Table 4.8: Calculated $j_{\text{het,AgI}}$ for emulsified samples containing solid AgI. $4 \mu\text{m}$ for r_{drop} is assumed in all calculations. $T_{\text{f,het}}$ are the experimentally determined freezing temperatures (see Tab. C.2).

solute	$S_{\text{AgI}} [\text{cm}^2]$	$T_{\text{f,het}} [\text{K}]$	$j_{\text{het,AgI}} [\text{cm}^{-2}\text{s}^{-1}]$
H ₂ O	$1.5 \cdot 10^{-8}$	255.00	$2.9 \cdot 10^6$
H ₂ O	$1.1 \cdot 10^{-8}$	254.87	$3.1 \cdot 10^6$
NaCH ₃ COO	$1.5 \cdot 10^{-8}$	244.70	$4.7 \cdot 10^5$
NaCH ₃ COO	$1.1 \cdot 10^{-8}$	226.52	$3.9 \cdot 10^6$
NaCH ₃ COO	$1.5 \cdot 10^{-8}$	232.98	$1.8 \cdot 10^6$
LiCl	$1.1 \cdot 10^{-8}$	252.68	$3.6 \cdot 10^6$
LiCl	$1.1 \cdot 10^{-8}$	245.95	$1.7 \cdot 10^6$
LiCl	$1.5 \cdot 10^{-8}$	239.69	$1.7 \cdot 10^6$
LiCl	$1.1 \cdot 10^{-8}$	223.41	$2.9 \cdot 10^6$
LiCl	$1.5 \cdot 10^{-8}$	231.75	$1.2 \cdot 10^6$
Glycerol	$1.5 \cdot 10^{-8}$	226.07	$1.1 \cdot 10^6$
K ₂ CO ₃	$1.1 \cdot 10^{-8}$	244.22	$1.7 \cdot 10^6$
K ₂ CO ₃	$1.1 \cdot 10^{-8}$	221.74	$1.6 \cdot 10^6$
K ₂ CO ₃	$1.5 \cdot 10^{-8}$	224.00	$8.3 \cdot 10^5$
K ₂ CO ₃	$1.1 \cdot 10^{-8}$	225.42	$1.2 \cdot 10^6$
Ethylene glycol	$1.5 \cdot 10^{-8}$	221.50	$1.6 \cdot 10^6$
Ca(NO ₃) ₂	$1.5 \cdot 10^{-8}$	233.01	$3.9 \cdot 10^6$
Ca(NO ₃) ₂	$1.1 \cdot 10^{-8}$	225.04	$3.5 \cdot 10^6$
MgCl ₂	$1.1 \cdot 10^{-8}$	251.14	$1.4 \cdot 10^6$
MgCl ₂	$1.1 \cdot 10^{-8}$	245.95	$1.2 \cdot 10^6$
MgCl ₂	$1.5 \cdot 10^{-8}$	240.27	$1.2 \cdot 10^6$
MgCl ₂	$1.5 \cdot 10^{-8}$	227.34	$1.8 \cdot 10^6$

have been estimated. In general, the results indicate that similar to homogeneous freezing, $j_{\text{het,AgI}}$ can be assumed to be constant for a specific $\Delta a_{\text{w,het}}$. Replacing in Eq. 4.9 the parameters of AgI by those of OAD, i.e., wt_{AgI} by wt_{OAD} , and ρ_{AgI} by ρ_{OAD} ($= 1.9 \text{ gcm}^{-3}$, Lide, 1998), the volume of a OAD crystallite (V_{OAD}) in a droplet can be calculated, whereas wt_{OAD} is known from the initial concentrations. The calculated $j_{\text{het,OAD}}$ lie again within 1 order of magnitude, which strengthen the conclusion that j_{het} is constant for a specific Δa_{w} , independently whether homogeneous ice nucleation of supercooled liquid droplets or heterogeneous ice nucleation with immersed IN are considered. It is obvious, that the calculated $j_{\text{het,OAD}}$ for the sample with solvcd NaCl is largest, because S_{OAD} it lowest, indicating that the heterogeneous rate is also similar for the different experiments, but is enlarged by a factor of ~ 2 compared to the emulsions with immersed AgI.

Two major conclusions can be withdrawn from the freezing points measurements of aqueous solutions with immersed different IN. A constant $\Delta a_{w,\text{het}}$ describes the measurements considerable good and j_{het} is constant for a specific $\Delta a_{w,\text{het}}$, which can be used to parameterize heterogeneous ice nucleation in the immersion mode in microphysical (see Chapter 5.1) or global climate models.

Table 4.9: Calculated $j_{\text{het,OAD}}$ for emulsified samples containing immersed OAD. $4 \mu\text{m}$ for r_{drop} is assumed in all calculations. $T_{\text{f,het}}$ and a_w are the experimentally determined freezing temperature and water activity of the samples.

solute [wt%]	wt_{OAD} [wt%]	S_{OAD} [cm^2]	$T_{\text{f,het}}$ [K]	$j_{\text{het,OAD}}$ [$\text{cm}^{-2}\text{s}^{-1}$]
H ₂ O	4.95	$4.5 \cdot 10^{-7}$	237.7	$4.5 \cdot 10^4$
H ₂ O	9.76	$7.0 \cdot 10^{-7}$	237.7	$3.1 \cdot 10^4$
H ₂ O	19.87	$1.2 \cdot 10^{-6}$	237.9	$1.8 \cdot 10^4$
10.0 malonic acid	4.0	$3.9 \cdot 10^{-7}$	233.5	$4.9 \cdot 10^4$
20.0 malonic acid	4.0	$3.9 \cdot 10^{-7}$	228.9	$4.7 \cdot 10^4$
30.0 malonic acid	4.0	$3.9 \cdot 10^{-7}$	222.1	$5.0 \cdot 10^4$
40.0 malonic acid	4.0	$3.9 \cdot 10^{-7}$	212.9	$3.9 \cdot 10^4$
14.9 NaCl	0.5	$9.7 \cdot 10^{-8}$	221.3	$2.2 \cdot 10^5$
4.0 SA	4.0	$3.9 \cdot 10^{-7}$	234.7	$5.1 \cdot 10^4$
2.0/2.0 SA/ABS	4.0	$3.9 \cdot 10^{-7}$	234.6	$5.5 \cdot 10^4$

Seite Leer /
Blank leaf

Chapter 5

Atmospheric implications

The freezing point experiments of four different ice nuclei have been discussed in the previous chapter. This chapter focuses on the implications of oxalic acid and nonadecanol on heterogeneous ice nucleation in the atmosphere, because the atmospheric presence of AgI and synthetic SiO₂-globules will rather be negligible small. So far, just a minor fraction of the entire organic composition has been identified on the level of individual compounds (Kanakidou et al., 2005), but it was found in several field campaigns that dicarboxylic acids can exhibit a large fraction of the total analyzed organic matter (e.g., Narukawa et al., 2003a,b). Long chain alcohols have been extracted on continentally derived marine aerosols and in biomass burning plumes with concentrations of a few nano grams per cubic meter sampled air (Gagosian et al., 1981; Simoneit et al., 1991; Stephanou, 1992; Nolte et al., 2001). Firstly, the influence of oxalic acid on cirrus cloud formation in the UT and the resulting change of the radiative forcing of such clouds is discussed on a global scale. Secondly, the possible role of nonadecanol as an atmospheric IN is presented.

5.1 Oxalic acid as a heterogeneous ice nucleus in the upper troposphere and its indirect aerosol effect

A manuscript published in *Atmos. Chem. Phys. Discuss.*, 6, 3571-3609, 2006 is presented in this section (Zobrist et al., 2006).

'Oxalic acid as a heterogeneous ice nucleus in the upper troposphere and its indirect aerosol effect'

B. Zobrist,^{1*} C. Marcolli,¹ T. Koop,² B. P. Luo,¹ D. M. Murphy,³
T. Corti,¹ A. Zardini,¹ U. Lohmann,¹ S. Fueglistaler,⁴
D. J. Cziczo,¹ U. K. Krieger,¹ P. K. Hudson,³ D. S. Thomson,³ T. Peter¹

¹Institute for Atmospheric and Climate Science, ETH Zurich, Zurich, Switzerland

²Department of Chemistry, Bielefeld University, Germany

³Earth System Research Laboratory, National Oceanic and Atmospheric Administration, Colorado, USA

*To whom correspondence should be addressed; E-mail: zobrist@env.ethz.ch

Abstract

Heterogeneous ice freezing points of aqueous solutions containing various immersed solid dicarboxylic acids (oxalic, adipic, succinic, phthalic and fumaric) have been measured with a differential scanning calorimeter. The results show that only the dihydrate of oxalic acid (OAD) acts as a heterogeneous ice nucleus, with an increase in freezing temperature between 2-5 K depending on solution composition. In several field campaigns, oxalic acid enriched particles have been detected in the upper troposphere with single particle aerosol mass spectrometry. Simulations with a microphysical box model indicate that the presence of OAD may reduce the ice particle number density in cirrus clouds by up to ~50% when compared to exclusively homogeneous cirrus formation without OAD. Using the ECHAM4 climate model we estimate the global net radiative effect caused by this heterogeneous freezing to result in a cooling as high as -0.3 Wm^{-2} .

Introduction

Cirrus clouds cover about 30% of the Earth's surface, playing an important role in the chemical and physical processes of the atmosphere. Their presence increases the scattering and absorption of solar radiation as well as the absorption of long wave terrestrial radiation (Baker, 1997). A change in cirrus cloud coverage may significantly alter the global radiation balance and hence the Earth's climate. The exact mechanisms of cirrus cloud formation is still unknown. Ice particles in cirrus clouds can form via homogeneous ice nucleation from liquid aerosols or by heterogeneous ice nucleation on solid ice nuclei (IN). Field observations indicate that IN are involved in the heterogeneous formation of some cirrus clouds (Chen et al., 1998; Cziczo et al., 2004b). Several laboratory studies have investigated heterogeneous ice nucleation on black carbon (DeMott et al., 1999) or inorganic IN, e.g., solid $(\text{NH}_4)_2\text{SO}_4$ (Zuberi et al., 2001), kaolinite and montmorillonite (Zuberi et al., 2002), hematite and corundum (Hung et al., 2003), aluminum oxide, alumina-silicate and iron oxide (Archuleta et al., 2005).

While the potential of organic aerosol particles to act as cloud condensation nuclei (CCN) has been established for water clouds (Novakov and Penner, 1993; Facchini et al., 1999), their influence on upper tropospheric ice clouds is less well known although they can constitute up to 50% or more of the dry aerosol mass even in the upper troposphere (UT) (Novakov et al., 1997; Middlebrook et al., 1998; Murphy et al., 1998). Theoretical studies indicate that homogeneous ice nucleation in aerosols containing organics may be impeded (Kärcher and Koop, 2005), in agreement with recent field observations (DeMott et al., 2003; Cziczo et al., 2004a). In contrast, the effect of solid organic IN on heterogeneous ice nucleation processes is largely unexplored. For this purpose, we define three prerequisites for an organic substance to act as an ice nucleus in upper tropospheric cirrus clouds:

- (i) Its abundance in the upper troposphere must be sufficiently high and its volatility sufficiently low to allow crystals to form in aqueous solutions.
- (ii) There must be a pathway leading to nucleation of organic crystalline forms.
- (iii) The organic crystals must act as immersion mode IN.

In the following, we try to identify organics that meet these criteria. As for criterion (i), several field studies have suggested that dicarboxylic acids are a significant component of the organic fraction with low volatility (Chebbi and Carlier, 1996; Yao et al., 2002). Dicarboxylic acids have been detected in various atmospheric environments, such as the marine boundary layer (Kawamura and Sakaguchi, 1999), at urban sites (Kawamura and Ikushima, 1993), in Arctic aerosols (Narukawa et al., 2003a), in the free troposphere (Narukawa et al., 2003b) and also in biomass burning plumes (Graham et al., 2002). The

prevalent dicarboxylic acid is usually oxalic acid, followed by malonic acid and succinic acid. Oxalic acid is the endpoint for the aqueous oxidation of some organics (Ervens et al., 2004).

Criterion (ii) is more restrictive because combined laboratory and modeling studies have revealed that internal mixing of a multitude of solutes - organic and/or inorganic - prevents the crystallization of minor components (Marcolli et al., 2004a). One possible exception are several dicarboxylic acids which may form stable crystals with low aqueous solubilities. Marcolli et al. (2004b) identified oxalic, succinic, fumaric, and phthalic acids as possible candidates for organics with a chance to crystallize from multi-component aqueous aerosol particles. It will be shown below that one pathway leading to crystallization of some of these acids is triggered by homogeneous ice formation. Once crystallized, these compounds will remain in crystalline form due to their low solubility even if the ice sublimates subsequently.

Criterion (iii) asks for IN in immersion mode, not in deposition mode. This is justified by considering that dicarboxylic acids are directly emitted into the atmosphere together with other aerosol components and mix internally via gas phase diffusion (Marcolli et al., 2004b) and/or are produced by slow conversion of organic precursors in the free troposphere (Legrand et al., 2005). Therefore, after crystallization they will remain suspended in a liquid medium and must then act as effective immersion IN.

While it has been shown that some dicarboxylic acids are inefficient IN in the deposition mode (Prenni et al., 2001; Parsons et al., 2004), their ability to induce ice freezing in the immersion mode is yet unexplored. Therefore, following Marcolli et al. (2004b), this study focusses on oxalic, succinic, adipic, fumaric and phthalic acids, as these have abundance-to-solubility ratios suitable for the formation of solids under atmospheric conditions. The possible role of these five crystalline dicarboxylic acids to act as IN immersed in aqueous solutions have been investigated in differential scanning calorimetry measurements. The obtained results were then implemented in a microphysical box model and in a global climate model to estimate the change in the microphysical properties and the radiative effect of cirrus clouds nucleated heterogeneously compared to exclusively homogeneously formed cirrus clouds.

Experimental section

Experimental setup

Experiments of emulsified aqueous solutions containing crystalline dicarboxylic acid were performed with a differential scanning calorimeter (DSC, TA Instruments Q10). Measurements were performed with phthalic, adipic, fumaric, succinic and oxalic acid. All substances were obtained from Fluka with purities of $\geq 99\%$. The emulsions were

made by adding a mixture of 23 wt% lanolin (Fluka Chemical) and 77 wt% mineral oil (Aldrich Chemical) to the aqueous solutions (made with distilled and deionized water, 18.2 M Ω), in which the lanolin/mineral oil represents 80% of the total volume. The samples were emulsified by applying a commercial drilling machine for 15 minutes, which leads to a mean diameter of the droplets of 4 ± 2 μm . Approximately 30 ± 5 mg of the emulsions were used for each DSC measurement, containing $\sim 10^5$ droplets.

The DSC temperature calibration was performed with the melting point of ice and the ferroelectric phase transition of $(\text{NH}_4)_2\text{SO}_4$ at 223.1 K. The accuracy of the reported freezing and melting points is ± 0.5 K and ± 0.4 K, respectively. Note that the precision of freezing points in a single emulsion is distinctly better than 0.2 K.

Experimental procedure

Figure 5.1 shows DSC heat flow curves for a typical experimental run with a 4.95 wt% aqueous oxalic acid solution. First the sample was cooled with a constant cooling rate (10 Kmin $^{-1}$) until the droplets in the emulsion froze (first cycle, solid red line). The onset of the exothermic peak was taken as the freezing point. The sample was then heated up with 1 Kmin $^{-1}$ (solid blue line) to a temperature which we term the conditioning temperature. This temperature was chosen to be above the eutectic melting point of ice and oxalic acid, but below the melting point of oxalic acid. The eutectic melting (all of the ice plus a fraction of the oxalic acid) gives rise to the intense peak with an onset at 272.2 K. In a next step, the sample was cooled again with the same cooling rate (second cycle, dashed red line), until freezing occurred. Finally, the sample was heated above the conditioning temperature such that the melting of oxalic acid was also observed (enlarged peak of the dashed blue line). For most of the solutions at least two independently prepared emulsions were investigated and for each emulsion the second freezing cycle was repeated twice.

Results and Discussion

Dicarboxylic acid/water systems

The measurements performed on dicarboxylic acid/water systems are summarized in Table 5.1. The concentrations of the organic acids have been chosen to cover the atmospherically relevant range and/or to force crystallization of the organic species. The conditioning temperatures were adjusted to ensure that at least part of the dicarboxylic acids remained solid at the end of the first heating cycle. Literature values of the saturation concentrations listed in Table 5.1 show that the dicarboxylic acids are close to or slightly above saturation at room temperature. For all but the least concentrated oxalic acid solutions,

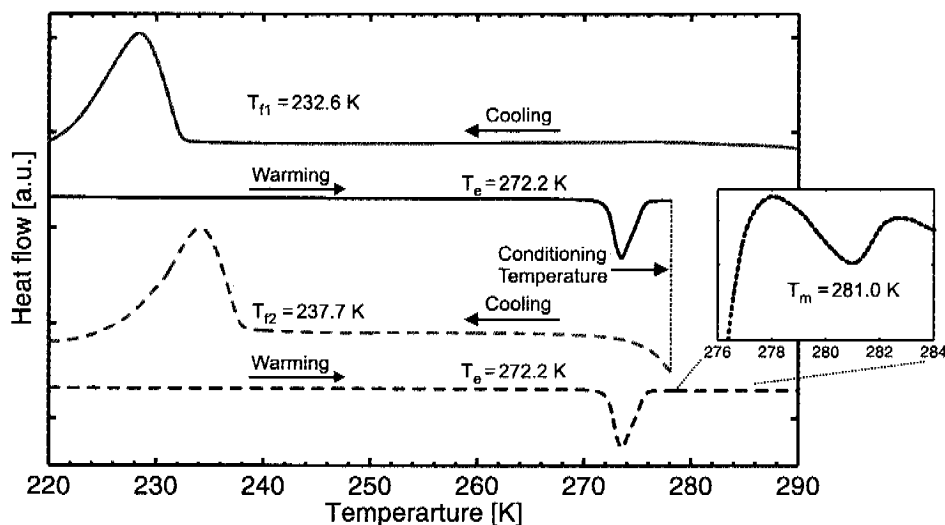


Figure 5.1: Typical DSC heat flow experiment of a 4.95 wt% oxalic acid/water solution. The curves belong to consecutive cooling/heating cycles with the identical sample and are shifted vertically for clarity. Solid red line: first cooling cycle with homogeneous freezing of the oxalic acid solution, i.e., formation of ice and solid oxalic acid. The onset of the heat release represents the homogeneous ice freezing temperature (T_{f1}). Solid blue line: first heating cycle with an endothermic peak arising from eutectic melting of ice and part of the OAD (T_e). The dotted black line is the conditioning temperature at which the sample is stored for ~ 1 min in order to ensure complete melting of ice, while some solid oxalic acid crystals remain in the emulsion droplets. Dashed red line: second cooling cycle with T_{f2} indicating the heterogeneous ice freezing temperature. Dashed blue line: second heating cycle again showing the eutectic melting (T_e) again, and an additional melting peak (T_m) at 281 K corresponding to the melting of the solid oxalic acid (see insert; note that the y-axis of the insert has been enlarged by a factor of 40).

as well as for the succinic and adipic acid solutions, the freezing of ice occurred in the first cycle at lower temperature than in the second cycle. This temperature difference may be due to two reasons. First, the crystallized dicarboxylic acid acts as a heterogeneous ice nucleus. Second, the concentration of the dicarboxylic acid is reduced to the saturation level in the presence of crystallized dicarboxylic acid leading to a higher homogeneous freezing temperature. The second effect is the more pronounced the higher the initial concentration. Therefore, the second freezing temperature must be actually compared with a reference measurement of a dicarboxylic acid solution that is just saturated at the ice freezing temperature. Since the solubilities of the dicarboxylic acids at around 235 K are extremely small (c.g., saturation concentration of oxalic acid at 236 K is around 0.35 wt%, based on a thermodynamical extrapolation of data at higher temperature), pure water was here chosen as the reference (see Table 5.1). This is a conservative estimate, as the small error induced by this procedure leads to a slight underestimation of the nucleation

Table 5.1: Summary of experiments with binary dicarboxylic acid/water systems and pure water reference measurement. C_{sample} and C_{sat} are the sample and the saturation concentration of the specific dicarboxylic acid. T_c is the conditioning temperature. T_{f1} and T_{f2} are the freezing temperatures of the first and second cycle, respectively. Literature data of melting points (T_m) are indicated in the brackets.

Solute	C_{sample} (wt%)	C_{sat} (wt%)	T_c (K)	T_{f1} (K)	T_m^* (K)	T_{f2} (K)	IN
pure water	—	—	—	235.9	273.2	235.9	—
Oxalic acid	2.50	4.46 at 278.15 K [†]	279	234.1	272.6 (272.5 ^{&})	234.1	no
Oxalic acid	4.95		279	232.3	272.2 (272.5 ^{&})	237.7	yes
Oxalic acid	9.76		279	229.6	272.2 (272.5 ^{&})	237.7	yes
Oxalic acid	19.87		279	222.9	272.2 (272.5 ^{&})	237.9	yes
Succinic acid	7.31	7.7 at 298 K [#]	277	232.0	272.6 (273.2 [§])	233.9	no
Adipic acid	1.61	1.4 at 288 K [#]	279	234.6	272.6 (273.2 [§])	235.1	no
Phthalic acid	0.63	0.54 at 287 K [#]	279	235.5	272.6	235.6	no
Fumaric acid	0.50	0.499 at 293 K [#]	279	234.9	272.6	234.9	no

*The melting point is either the eutectic melting point or the ice melting point

†Apelblat and Manzurova (1987), #Stephen and Stephen (1963), &Braban et al. (2003), §Parsons et al. (2004)

potential of the organic ice nucleus. In summary, a specific dicarboxylic acid acts as a heterogeneous ice nucleus when the freezing temperature of the second cycle is higher than the homogeneous freezing temperature of pure water. In the following we term this temperature difference ΔT_{het} .

For all but the least concentrated oxalic acid/water samples, ΔT_{het} lies between 1.8–2.0 K, indicating that solid oxalic acid acts as a heterogeneous ice nucleus in the immersion mode. Since no other exothermic peak is found in the freezing curves and considering also the melting point in the last heating cycle at 281 K of Fig. 5.1, solid oxalic acid must have formed in the first cycle along with or triggered by ice formation. The solid is assumed to precipitate as oxalic acid dihydrate (OAD) nano-crystals (Braban et al., 2003). Heterogeneous nucleation was not observed for the 2.5 wt% aqueous oxalic acid solution since it is below the eutectic concentration of ~ 3 wt%, and hence no solid compounds remained in the droplets after the first heating cycle. Therefore the freezing temperatures of both cycles are identical and the measured endothermic peak does not indicate eutectic but regular ice melting. Melting points and eutectic points of these solutions are in good agreement with Braban et al. (2003), who investigated aerosol phase transitions (deliquescence and efflorescence) and bulk solution properties of these aqueous solutions, but not their ice nucleation potential. The concentration of oxalic acid in the solutions, and hence the surface area of the solid OAD, are varied over a considerable range: assuming a spherical nucleus, the surface of OAD of the most concentrated solution is larger by a factor of 2.4

than in the 5 wt% solution. Nevertheless, the heterogeneous freezing temperatures differ by only ~ 0.2 K, which is less than the variability caused by different emulsions. From this we conclude that the heterogeneous freezing rate coefficient under these conditions must be a very steep function of temperature, which is not unusual for ice nucleation processes (Pruppacher and Klctt, 1997).

The freezing points of the second cycles of the other dicarboxylic acids are all lower than the reference measurement with pure water, indicating that heterogeneous nucleation is inefficient and that freezing point depression due to higher solution concentration dominates. Two cases can be distinguished. First, succinic and adipic acid show a similar behavior as oxalic acid with a clear temperature difference between the first and second cooling cycles. Hence, succinic and adipic acid must have crystallized, although their melting points could not be detected when the samples were heated above the conditioning temperature at the end of the experiment. In a recent study, Parsons et al. (2004) concluded that succinic and adipic acid are not good IN above 243 K in the ice deposition mode. From both data sets, we conclude that these solid acids are unlikely to play any role in heterogeneous ice nucleation in the atmosphere, neither in deposition nor in immersion mode. In the case of phthalic and fumaric acid, the difference of the freezing temperatures between the two cycles are negligibly small because of the low initial concentrations, but since both acids are supersaturated substantially during ice formation, we may nevertheless assume that the acids have crystallized. With the chosen concentrations these nuclei would not melt at the conditioning temperature. Hence, phthalic and fumaric acid are also unlikely to act as IN under atmospheric conditions.

In summary, our results show that out of these five candidates only solid oxalic acid serves as an ice nucleus. However, under atmospheric conditions, solid oxalic acid IN will rarely occur in pure water, but in aqueous solutions together with other organic or inorganic species. Such mixed systems are discussed in the next section.

Oxalic acid/aqueous solutions systems

For the oxalic acid/aqueous solution systems the same experimental procedure was used as for the pure dicarboxylic acid solutions with suitable choices for reference samples. Measurements were performed with different inorganic and organic aqueous solutions, all containing various amounts of oxalic acid (Table 5.2). The exact composition of the solutions in equilibrium with OAD is not generally known. This problem can be overcome by distinguishing two cases. If the concentration of the oxalic acid is negligibly small compared to the additional solute, the concentration of the reference sample can be taken as composition of the initial solution without the oxalic acid. (e.g. solution of interest: 14.9 wt% NaCl/ 0.5 wt% oxalic acid, reference solution: 14.9 wt% NaCl). However, if oxalic acid constitutes a substantial part of the total solute, a considerable error would be introduced by the above procedure. After the crystallization of the OAD in the first cycle,

most of the oxalic acid and a minor part of the water are withdrawn from the solution. Consequently, the sample is more highly concentrated with respect to the additional solute. Therefore the concentration of the reference sample was adjusted for each investigated solution assuming that upon crystallization of OAD no oxalic acid is left in the solution (e.g. solution of interest: 40.0 wt% Malonic acid/ 4 wt% oxalic acid, reference solution: 42.7 wt% Malonic acid).

Table 5.2: Summary of measurements for oxalic acid/aqueous solution systems and for the corresponding reference measurements. The following labels are used for the solutes: oxalic acid (OA), malonic acid (MA), ammonium sulfate (AS), ammonium bisulfate (ABS) and sulfuric acid (SA). The temperature and concentration values are given in Kelvin and weight % of the total solution, respectively. T_{f1} and T_{f2} are the freezing temperatures of the first and second cycles, respectively. T_m indicates the ice melting point of the aqueous solution, with the corresponding literature values in brackets. $\Delta a_{w,het}$ values are determined using Eq. 5.4.

Measurements of oxalic acid/aqueous solution systems							Reference measurements			ΔT_{het}	$\Delta a_{w,het}$
Solute	Conc.	OA Conc.	T_{f1}	T_m	T_{f2}	IN	Conc.	T_f	T_m		
NaCl	14.9	0.1	216.4	262.1	216.4	no	14.9	216.9(215.7) [†]	262.2(262.1 [†])	-0.5	-
NaCl	14.9	0.33	216.4	262.0	221.7	yes	14.9	216.9(215.7) [†]	262.2(262.1 [†])	4.8	0.282
NaCl	14.9	0.5	215.9	262.0	221.3	yes	14.9	216.9(215.7) [†]	262.2(262.1 [†])	4.4	0.284
MA	10.0	4.0	228.4	270.5	233.5	yes	10.7	230.5	271.2(271.3 [#])	3.0	0.288
MA	20.0	4.0	223.1	268.2	228.9	yes	21.4	225.0	268.8(268.9 [#])	3.9	0.284
MA	30.0	4.0	215.2	264.8	222.1	yes	32.1	217.8	265.5(265.2 [#])	4.3	0.284
MA	40.0	4.0	204.2	259.7	212.9	yes	42.8	207.9	260.1(260.9 [#])	5.0	0.284
AS	4.0	4.0	230.3	271.8	232.3	no	4.27	232.8(232.3) ^{&}	271.9(271.9 [§])	-0.5	-
AS	30.0	3.0	212.1	262.8	213.2	no	31.8	210.6(210.7) ^{&}	261.0(261.7 [§])	2.6	-
ABS	4.0	4.0	230.5	271.5	232.3	no	4.27	232.0(230.7) [¶]	271.9(271.7 [§])	0.3	-
SA	4.0	4.0	229.4	271.0	234.7	yes	4.27	231.3(231.8) [‡]	271.4(271.3 [§])	3.4	0.285
SA/ABS	2.0/2.0	4.0	230.0	271.2	234.6	yes	2.13/2.13	232.1	271.90(271.7 [§])	2.5	0.290

[†]Rasmussen and MacKenzie (1972), [#]Hansen and Beyer (2004), [&]Bertram et al. (2000), [§]Clegg et al. (1998), [‡]Koop et al. (1998), [¶]Koop et al. (1999)

Aqueous NaCl/oxalic acid

The solubility of oxalic acid is drastically decreased in a highly concentrated NaCl solution. While the solution with 0.1 wt% oxalic acid is subsaturated at room temperature, those with 0.33 and 0.5 wt% oxalic acid are supersaturated. Consequently these two solutions had to be placed in a water bath (~ 310 K) before the emulsions could be prepared. The freezing temperatures of the first and the second cycles are identical for the weakest concentrated solution and thus no solid oxalic acid exists in the droplets after the first heating cycle. The other two solutions show the same behavior as the binary oxalic acid/water system. Namely, the freezing points of the second cycle are clearly higher

($\Delta T_{\text{het}} \sim 4.5$ K) than that of the reference measurement with a 14.9 wt% NaCl solution. Again, ΔT_{het} does not depend on the oxalic acid concentration. The melting peak of the solid oxalic acid is smaller than the resolution of the DSC and could not be observed at the end of the experiment.

Aqueous malonic acid/oxalic acid

For the malonic/oxalic acid solutions, the concentrations of malonic acid are varied from 10 wt% to 40 wt%, whereas the oxalic acid concentration was held constant at 4 wt%. None of these solutions are supersaturated at room temperature. Heterogeneous ice nucleation induced by OAD is observed in all experiments. ΔT_{het} varied between 3.0 and 5.0 K. The melting of the solid oxalic acid has been identified in all measurements, whereby the melting temperatures increase with increasing concentration of the malonic acid, indicating that the presence of malonic acid decreases the solubility of oxalic acid in the sample.

Aqueous $(\text{NH}_4)_2\text{SO}_4$ /oxalic acid and NH_4HSO_4 /oxalic acid

In the presence of $(\text{NH}_4)_2\text{SO}_4$ (AS) and NH_4HSO_4 (ABS) the solubility of oxalic acid is strongly reduced. The stock solution had to be put in a hot water bath for full dissolution. When the solutions were kept at room temperature overnight, crystals slowly formed again. Nevertheless, the temperature difference between the first and the second freezing cycle are in accordance with a homogeneous freezing process. ΔT_{het} is approximately zero for the 4 wt%/4 wt% AS/oxalic acid and the 4 wt%/4 wt% ABS/oxalic acid systems. The positive value for the 30 wt%/3 wt% AS/oxalic acid solution cannot be considered as an indication of heterogeneous freezing since the melting point is also elevated by 1.5 K compared with the reference measurement. Nevertheless a solid phase must have formed based on the increase in the freezing temperature between the first and the second freezing cycle and the elevated melting temperature. This solid phase is not active as a heterogeneous ice nucleus, and therefore must be different from OAD. To confirm this hypothesis we determined the composition of the crystals that crystallized from the stock solution by elemental analysis (C,H,N,S,O by pyrolysis method and H_2O by Karl Fischer, Solvias AG Basel Switzerland). The absence of sulfur and the relative ratio of the other elements indicates that this new phase consists of ammonium, oxalic acid and water in a ratio of 1:2:2. This stoichiometry is in agreement with the formation of $\text{NH}_4\text{H}_3(\text{C}_2\text{O}_4)_2 \times 2\text{H}_2\text{O}$, a precipitate that was also reported to form in ammoniated oxalic acid solutions above room temperature (Stephen and Stephen, 1963). We conclude that oxalic acid precipitated as $\text{NH}_4\text{H}_3(\text{C}_2\text{O}_4)_2 \times 2\text{H}_2\text{O}$ in the experiments, indicating that it is not oxalic acid per se that acts as an IN, but rather only its dihydrate.

Aqueous H_2SO_4 /oxalic acid and H_2SO_4 / NH_4HSO_4 /oxalic acid

Since at cirrus cloud altitudes aerosols can be very acidic, we also investigated OAD-induced ice nucleation in acidic solutions with sulfuric acid (SA) and a mixture of SA and ABS. We found no evidence of any deterioration of the emulsions. The ΔT_{het} values clearly show that heterogeneous nucleation occurred. Therefore OAD must have crystallized under these acidic conditions.

Water activity based theory for heterogeneous ice nucleation

It has been shown that homogeneous ice nucleation in aqueous solutions depends solely on the water activity of the solution independently of the nature of the solute (Koop et al., 2000). Therefore, a water activity dependence of heterogeneous immersion freezing of ice is well conceivable. In fact, experimental studies with inorganic nuclei seem to support this view (Zuberi et al., 2002; Archuleta et al., 2005), and a water-activity-based parameterization of heterogeneous freezing for model applications has been proposed (Kärcher and Lohmann, 2003). In Fig. 5.2 heterogeneous freezing points of droplets with immersed OAD nano-crystals and reference measurements without OAD nano-crystals as a function of the solution water activity, a_w are shown. The a_w -values of the reference solutions were determined from the measured ice melting point temperatures, T_m . In order to estimate a_w at the freezing temperatures it was assumed that a_w in these solutions does not depend on temperature, i.e., $a_w(T_f) \approx a_w(T_m)$. In addition, since the solubility of OAD at the heterogeneous freezing point is extremely small, the a_w -values determined in the reference measurements were also adopted for the solutions containing OAD nano-crystals.

In previous studies (Koop et al., 2000), it was found that the homogeneous ice freezing points of a large number of aqueous solutions scatter around a common homogeneous freezing point line (solid line) that is horizontally parallel to the ice melting point line (dash-dotted line), i.e., a constant offset between the two lines exists. More generally, a horizontal offset with respect to the ice melting point curve can be determined for any individual heterogeneous freezing point, $\Delta a_w(T_{f,\text{het}})$, and homogeneous freezing point, $\Delta a_w(T_{f,\text{hom}})$, by evaluating:

$$\Delta a_w(T_{f,\text{het}}) = a_w(T_f) - a_w^i(T_{f,\text{het}}) \quad (5.1)$$

and

$$\Delta a_w(T_{f,\text{hom}}) = a_w(T_f) - a_w^i(T_{f,\text{hom}}) \quad (5.2)$$

where $a_w(T_f) \approx a_w(T_m)$ is the water activity at the freezing point determined from the measured ice melting point, and $a_w^i(T_{f,\text{het}})$ and $a_w^i(T_{f,\text{hom}})$ are the water activities on the

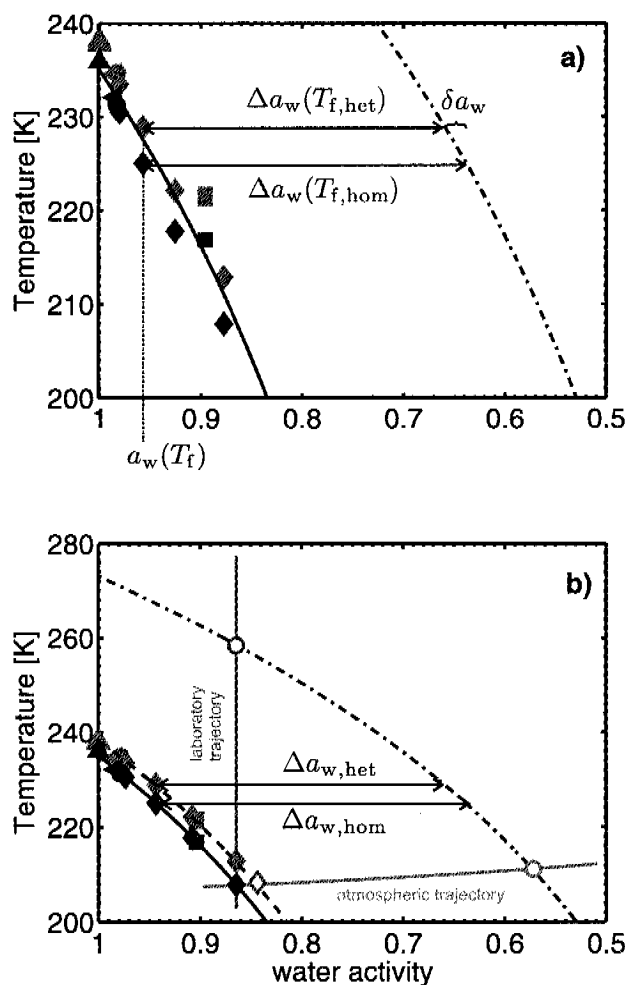


Figure 5.2: Experimental freezing points of micrometer sized aqueous solution droplets. a) Heterogeneous ice freezing points in the presence of OAD nano-crystals (red symbols) and homogeneous ice freezing points (reference, blue symbols) as a function of water activity. Upward triangles: water; left pointing triangles: SA/ABS; bullets: SA; diamonds: MA; squares: NaCl (see Table 5.2). Red and blue symbols appear as pairs at given water activity indicating the ice freezing temperatures of a specific solution in the presence or absence of OAD IN. The solid line is the homogeneous ice freezing curve for supercooled aqueous solutions and the dash-dotted line is the ice melting point curve (Koop et al., 2000). b) Lines and symbols as in a). The various pairs of freezing points were shifted horizontally such that the homogeneous freezing point of the reference sample is in accordance with the homogeneous freezing point line (solid). The magenta and green lines indicate a typical laboratory DSC trajectory and an atmospheric trajectory with ice melting points shown by the magenta and green circles, respectively. Under atmospheric conditions, aerosol particles containing OAD nano-crystals will nucleate ice heterogeneously at a lower water activity, and thus lower supersaturation (open red diamond) than is required for homogeneous ice nucleation without OAD (blue diamond).

ice melting point curve at the heterogeneous and homogeneous freezing temperature, respectively. Subtracting Eq. 5.1 from Eq. 5.2 defines the corresponding difference in water activity, δa_w , between each pair of heterogeneous/homogeneous ice freezing points corresponding to a sample-with-OAD/reference-without-OAD pair:

$$\delta a_w = \Delta a_w(T_{f,\text{hom}}) - \Delta a_w(T_{f,\text{het}}). \quad (5.3)$$

This δa_w is indicated in Fig. 5.2a for one sample/reference pair.

We note, that the homogeneous freezing points (blue) scatter by less than 2% – around the homogeneous ice freezing line predicted by water-activity-based ice nucleation theory (black line). The most likely explanation for these small differences is that the water activity in the investigated solutions changes slightly with temperature, and is not constant as was assumed to construct Fig. 5.2a. Such small changes in water activity with decreasing temperature are quite common, however, measurements of a_w in solutions supersaturated with respect to ice are not available for the investigated solutions at low temperatures. Recently, Braban et al. (2003) measured the water activity of malonic acid solutions in bulk samples as a function of temperature, however, only above 274 K. Their data, together with measurements at room temperature of Choi and Chan (2002), indicate that within experimental error no temperature dependence of the water activity of malonic acid above the ice melting point exists for concentrations relevant to our study. However, it is known from other organic substances that the water activity may indeed vary strongly with decreasing temperature (Zobrist et al., 2003; Koop, 2004). Therefore, since the exact value of $a_w(T_f)$ is unknown, we allow for a small change in water activity of a solution with decreasing temperature by adjusting $a_w(T_f)$, such that all measured homogeneous freezing points fall onto the water-activity-based homogeneous freezing line. Technically this can be achieved by defining a $\Delta a_{w,\text{het}}$ which can be calculated for each measured heterogeneous freezing point by

$$\Delta a_{w,\text{het}} = \Delta a_{w,\text{hom}} - \delta a_w \quad (5.4)$$

where $\Delta a_{w,\text{hom}} = 0.305$ (Koop et al., 2000). The resulting individual $\Delta a_{w,\text{het}}$ -values for each sample are given in Table 5.2, and the arithmetic mean of all measurements is $\Delta a_{w,\text{het}} = 0.285$.

It should be noted that atmospheric aerosol particles in a cooling air parcel follow a pathway different from that used in our experiments. In the laboratory, the droplets are cooled at a constant composition until they freeze homogeneously or heterogeneously. The laboratory trajectory for a solution containing 40 wt% malonic acid and 4 wt% oxalic acid is shown schematically as the magenta line in Fig. 5.2b. In contrast, the composition of an atmospheric aerosol droplet is determined from the balance of water partial and vapor pressures (green line), i.e., from relative humidity, which is equal to a_w under equilibrium conditions. Once the atmospheric trajectory has passed the frost point (green circle), the aerosol particles are supersaturated with respect to ice. Liquid droplets

will freeze at the homogeneous freezing point (blue diamond), unless they contain an ice nucleus such as an OAD nano-crystal which will induce freezing when they reach the heterogeneous freezing line (open red diamond).

Atmospheric implications

So far it was shown that oxalic acid may act as a immersion mode ice nucleus and that the effect can be parameterized using water-activity-based nucleation theory. In the following, the occurrence of OAD in the UT and its possible influence on the microphysical and radiative properties of cirrus clouds are investigated.

Single particle measurements

In a recent field campaign in the UT, oxalic acid constituted a considerable fraction of the total classified organics (Narukawa et al., 2003b). The presence of oxalic acid in upper tropospheric aerosols is also supported by particle analysis by laser mass spectrometry (PALMS) instrument. Figure 5.3a shows an example of a PALMS single particle mass spectrum that contains an oxalate peak at mass peak 89. The cluster ions at mass peak 179 show that the mass peak 89 is due to a molecule with a mass of 90 which readily loses a proton and undergoes little fragmentation. The lack of major isotopes eliminates any molecules with sulfur, chlorine, etc. Oxalic acid is the only species identified in aerosol particles with these characteristics, although peroxypropionic acid and hydroxypropionic acid have the same molecular weight. This exemplary particle is probably quite acidic because laboratory tests have shown that cluster ions containing H_2SO_4 are more common in mass spectra from sulfuric acid than from ammonium sulfate. Up to 1% of the total mass spectra collected in several field campaigns contained a significant oxalate ion peak. Figure 5.3b depicts a vertical distribution of the mass peak 89, indicating a clear maximum of oxalate in the mass spectra in the middle and upper troposphere. At lower altitudes, besides a lower abundance of mass 89 in the spectra, those particles showing mass 89 were usually neutralized (as indicated by the simultaneous presence of sulfate, nitrate, and a wide variety of organic acid peaks) instead of acidic as in the example in Fig 5.3a. The frequency of the oxalic acid enriched particles starts to fall off also in the stratosphere with the smaller overall proportion of organic material there (Murphy et al., 1998).

PALMS was flown in the CRYSTAL-FACE campaign in 2002 with a counterflow virtual impactor inlet with the capability of separating ice crystals from interstitial aerosol particles and then evaporating the water by heating the inlet to detect the ice nucleus (Cziczo et al., 2004a). Despite the heating, one of the mass spectra of ice nuclei had

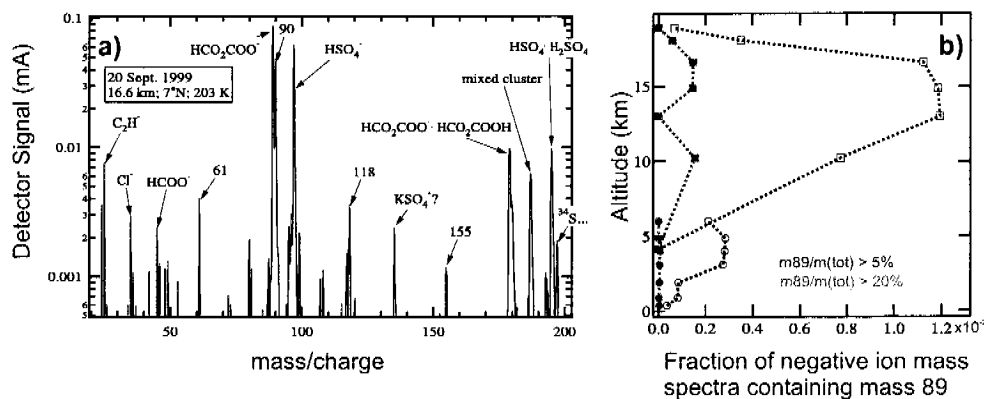


Figure 5.3: a) Mass spectra of the PALMS with a large mass peak 89. b) The frequency of negative ion mass spectra measured by the PALMS instrument, where the relative intensity of the $m89$ peak is 5% (black) or 20% (red) of the total ion signal. The B57 (open and solid squares; 33323 spectra, mostly above 10 km) data include flights from 1998 (WAM), 1999 (ACCENT) and 2004 (PAVE) missions. The P3 data (open and solid circles; 249,949 spectra, below 7 km) are from 2004 (NEAQS/ICARTT).

a significant oxalate peak as well as sulfate probably in the form of sulfuric acid (199 ice crystals were sampled in this flight). Although only one particle, it does indicate that mixed particles of oxalic and sulfuric acid can act as ice nuclei in clouds. This spectrum of an ice nucleus had the largest oxalate peak of any particle observed during the CRYSTAL-FACE mission and was acquired at 14.4 km altitude during a flight on the 9th July 2002 south along the Yucatan peninsula (Cziczo et al., 2004a). It is interesting to note that most of the cirrus clouds sampled during this mission were convectively formed and contained residues with the signature of aerosols of boundary layer and lower tropospheric origin (e.g., sea salt and mineral dust). The cloud encountered on the 9th July was the only case of a cloud which appeared to freeze from aerosols with a free tropospheric signature (i.e., predominantly sulfates).

The OAD nano-crystal precipitation in the atmosphere may be triggered by ice formation when a cirrus cloud is nucleated homogeneously, similar to the laboratory experiments. Once formed, OAD nano-crystals will grow via gas phase diffusion of oxalic acid at the expense of remaining liquid particles, similar to a Bergeron-Findeisen process. Vapor pressure measurements of aqueous oxalic acid particles performed in an electrodynamic balance (see Appendix A) suggest that the growth of a OAD nano-crystal to a particle with a radius of $0.1 \mu\text{m}$ takes 33 hours at 235 K, which is sufficiently fast to occur on atmospheric time scales. Because of their low solubility and vapor pressure OAD nano-crystals will persist even if the ice crystals sublimate in drier air masses or at lower altitudes in sedimenting ice particles.

Microphysical Box model

In order to investigate the change in the microphysical properties of cirrus clouds nucleated on OAD compared to cirrus clouds exclusively formed by homogeneous nucleation, the microphysical box model first described by Hoyle et al. (2005) was expanded to include heterogeneous ice nucleation (see Appendix B). Figure 5.4 shows the simulated ice number densities (n_{ice}) as a function of constant cooling rate in the absence and presence of OAD nano-crystals. The presence of a limited number of heterogeneous IN reduces the final ice number density largely when compared to the homogeneous case, an effect that has also been observed in a similar modeling study (Kärcher and Lohmann, 2003). This reduction is maximized when the ice number density expected from homogeneous nucleation is similar to the number density of the heterogeneous IN, because in this case the heterogeneously nucleated ice particles deplete the gas phase sufficiently to suppress subsequent homogeneous nucleation, leading to a maximum lowering of ice number densities as compared to the purely homogeneous case.

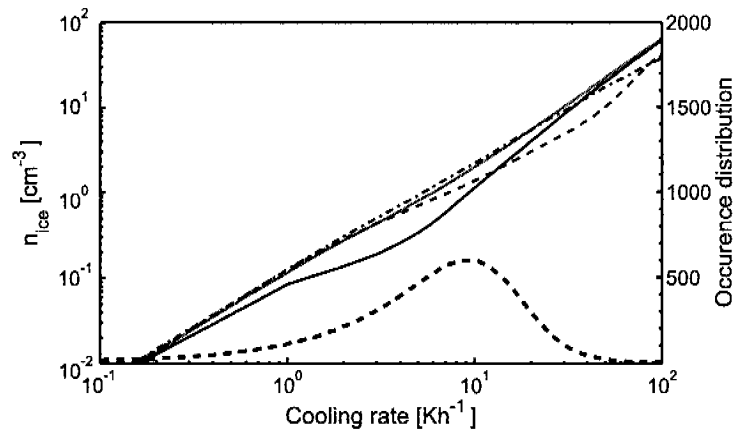


Figure 5.4: Ice number density as a function of cooling rates for homogeneous and heterogeneous ice nucleation with OAD. Colored curves: simulated ice number density as a function of cooling rate. Red line: only homogeneous nucleation. Blue lines: homogeneous nucleation together with heterogeneous nucleation on solid oxalic acid aerosols with various IN numbers for oxalic acid. Solid, dashed and dashed dotted blue line: $n_{\text{OAD}} = 0.1, 1$ and 10 cm^{-3} , respectively. Black dashed line: occurrence distribution of mesoscale cooling rates based on aircraft measurement during the SUCCESS campaign (see Appendix B and Hoyle et al., 2005).

Occurrence frequencies of ice particle number densities (n_{ice}) can be simulated for initial homogeneous nucleation followed by competitive OAD-induced heterogeneous and homogeneous ice nucleation. The simulations were performed at temperatures of 200, 215 and

230 K thus covering a range in altitudes from 11-15 km. The results shown in Fig. 5.5 indicate that the presence of OAD in the aerosols leads to a reduction in n_{ice} by up to $\sim 50\%$ when compared to purely homogeneous freezing, resulting in $\sim 20\%$ decrease in optical depth, which corresponds to a negative Twomey effect (Kärcher and Lohmann, 2003; Lohmann and Feichter, 2005). In addition, fewer ice particles with larger sizes sediment faster and reduce the lifetime of the cloud.

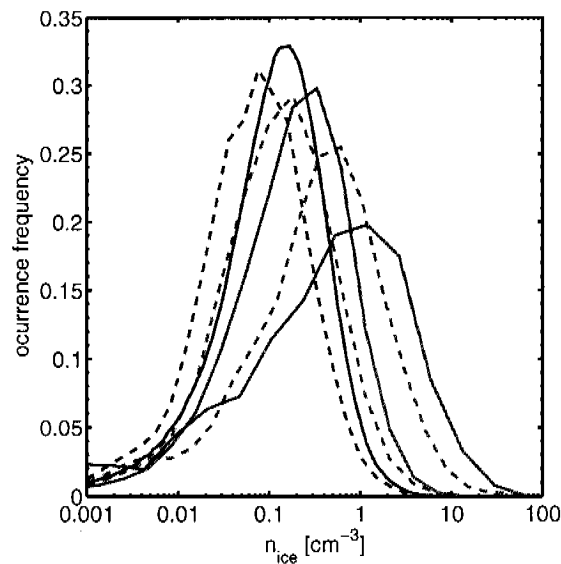


Figure 5.5: Simulated ice particle number density distributions of cirrus clouds on three different height levels induced by homogeneous ice nucleation alone (solid lines) and by homogeneous together with heterogeneous ice nucleation on OAD particles (dashed lines). red: 15 km, $T=200$ K, ice water content (IWC)=6 ppm; green: 13 km, $T=215$ K, IWC=38 ppm; blue: 11 km, $T=230$ K, IWC=180 ppm.

Global radiative modeling

We calculated the shortwave and longwave radiative effect at the top-of-the-atmosphere (TOA) using the ECHAM4 climate model (Appendix C) in order to investigate the global impact of the reduction of n_{ice} caused by heterogeneous freezing in the presence of OAD. This effect was obtained by implementing the temperature dependent increase in effective ice crystal radius in the radiation routine derived from the above microphysical calculations (see Fig. 5.5). The radiative transfer scheme was then called once again diagnostically with this changed effective radius while keeping all other parameters the

same, such as ice water content and cloud cover. Figure 5.6 shows shortwave and longwave TOA effect of cirrus clouds formed in the presence of OAD nano-crystals compared to cirrus clouds exclusively homogeneously nucleated. With the obtained temperature dependent reduction of n_{ice} , heterogeneous freezing in the presence of OAD causes a global mean negative Twomey effect of $+0.3 \text{ Wm}^{-2}$ in the shortwave that is overcompensated by increased longwave emission of -0.6 Wm^{-2} , yielding a net effect of -0.3 Wm^{-2} . This effect is most pronounced in areas of tropical deep convection and extratropical storm tracks. This estimate represents an upper bound because all cirrus clouds were considered to have frozen in the presence of OAD.

These results pose the question, which fraction of atmospheric ice particles might actually nucleate in the absence of OAD, which would then reduce the estimate in Fig.5.6? We have presently no suitable method to estimate which percentage of all cirrus clouds in the real atmosphere has previously undergone ice formation, exposing them to the effect of OAD, and which percentage of all cirrus clouds has nucleated for the first time, i.e., without exposure to OAD. This percentage might be different for regions with cirrus originating predominantly from deep convection than for regions with cirrus nucleating predominantly in situ in slow upwelling. For liquid clouds it is well known that the water undergoes multiple condensation and evaporation cycles before the water precipitates, typically 10-times (Pruppacher and Jaenicke, 1995). Although it is likely to be similar for ice clouds, we are not aware of investigations of this issue.

We have attempted to estimate how many freezing/evaporation cycles an air mass passes through by using trajectory calculations based on the 3-dimensional, 6 hourly wind fields of the 40 year reanalysis ERA-40 provided by the European Centre for Medium-range Weather Forecast (ECMWF). 10-day backward trajectories provide the required information to determine the fraction of clouds nucleating in air parcels that had previously been glaciated and therefore contain OAD. It was found that at 150 hPa typically 90% of all air in cirrus clouds had experienced a previous glaciation, at 200 hPa still 63%, but at 300 hPa only 13% (globally averaged numbers). When these results were implemented in the ECHAM4 climate model, the calculated effect of OAD reduces from -0.3 Wm^{-2} to -0.04 Wm^{-2} , simply because many of the cirrus clouds at lower levels have nucleated ice for the first time. In this sense the results shown in Fig. 5.6 present upper limits of the OAD effect. However, we think that the lower limit of only -0.04 Wm^{-2} is likely to be a gross underestimation of the OAD effect because the trajectory calculations ignore the presence of smaller scale temperature perturbations (including in-cloud turbulence) which will increase the frequency of nucleation/evaporation cycles far beyond the result from the synoptic-scale trajectory calculation. We have at present no proper means to calculate the frequency of cirrus formation in individual air parcels.

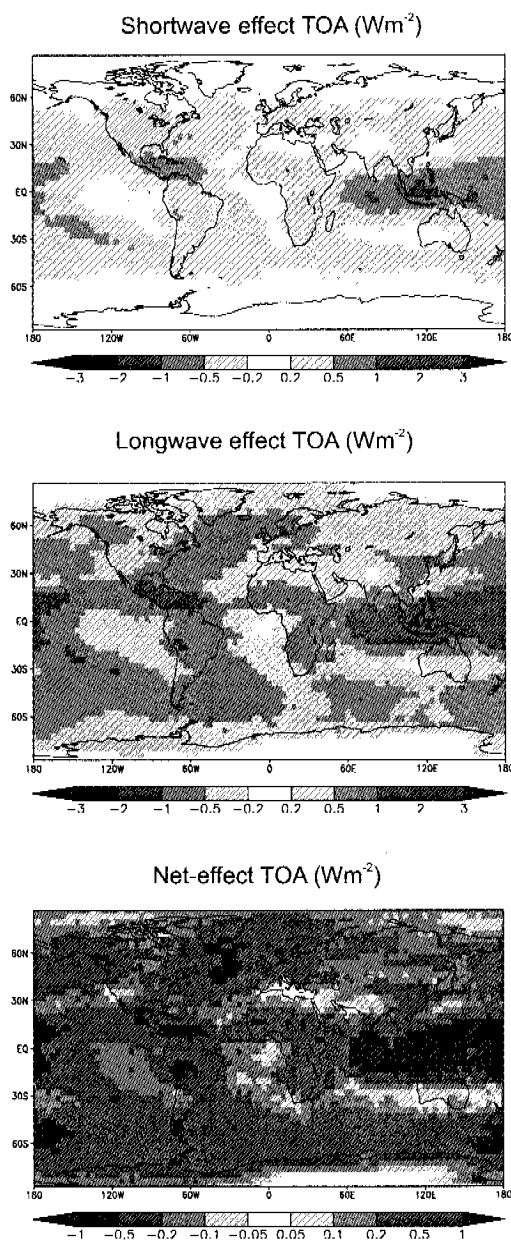


Figure 5.6: Global shortwave, longwave and net TOA effect of cirrus clouds that have nucleated heterogeneously on solid OAD particles as compared to cirrus clouds formed in the absence of OAD. A positive shortwave effect means that less solar radiation is reflected to space. A negative longwave effect means that more longwave radiation is emitted to space.

Conclusion

Measurements of heterogeneous freezing points with various immersed dicarboxylic acids in different aqueous solutions have been presented. It was found that only oxalic acid, in the form of OAD, acts as a heterogeneous ice nucleus. The heterogeneous freezing points do not depend strongly on the oxalic acid surface area, which indicates that the heterogeneous rate coefficient is a strong function of temperature. The ΔT_{het} for the different aqueous solution is between 1.8 and 5 K, with ΔT_{het} increasing with increasing concentration of the solution. Water-activity-based nucleation theory (Koop et al., 2000) adapted to heterogeneous ice nucleation in the immersion mode showed that the measured heterogeneous freezing points are well described by a constant offset of $\Delta a_{\text{w,het}} = 0.285$. We can conclude that the heterogeneous ice nucleation in the immersion mode is generally described by a constant offset $\Delta a_{\text{w,het}}$ for each ice nucleus, since the same approach was already applied successfully in two other independent studies using different IN (Zuberi et al., 2002; Archuleta et al., 2005). Simulations with a microphysical box model indicate that OAD nano-crystals decrease the ice particle number density in cirrus clouds by up to 50%, which leads to a reduction of the optical depth by up to 20%. The net-radiative effect of cirrus clouds nucleated heterogeneously on OAD nano-crystals compared to exclusively homogeneously nucleated clouds is estimated by the ECHAM4 model to be at most -0.3 Wm^{-2} .

These results suggest a potentially strong influence of oxalic acid on the radiation budget. However, they also give rise to several questions that should be investigated in future studies: What are the major sources for oxalic acid in the UT and how are they influenced by anthropogenic factors? Could a change in emissions of organic precursors or in climatic conditions have influenced the abundance of oxalic acid in the free troposphere?

For OAD containing particles to be active as IN, the oxalic acid must crystallize as OAD. Our DSC experiments have shown that this happens concurrently with or induced by ice freezing. In the atmosphere this means that an air parcel must have undergone a freezing/evaporation cycle to contain OAD IN. Hence, the occurrence of this type of IN depends on the history of the air parcel.

There is ample evidence that the UT at cirrus levels is heavily loaded with oxalic acid (Narukawa et al., 2003a, and this study) and it is very likely that its mixing ratio is anthropogenically influenced. However, this does not mean that the OAD-induced heterogeneous ice nucleation discussed here must also be affected by changes in the oxalic acid mixing ratios. Rather, there could be a threshold for the OAD effect which results as follows. According to the process outlined here, the number density of OAD nuclei is solely determined by the initial homogeneous ice nucleation, i.e., independent of the oxalic acid mixing ratio. The resulting OAD IN grow subsequently via the Bergeron-Findeisen process. If oxalic acid mixing ratios change, this will affect the size of OAD IN but not their number density, and hence will not affect the ice particle number densities of second

and higher generation clouds. Therefore, it is unlikely that there is a linear dependence between oxalic acid and cirrus properties. Conversely, there must be a threshold at some low mixing ratio, below which the oxalic acid concentration is too low to form OAD or the resulting IN become too small to be still efficient. However, this argument also has limitations. It ignores that OAD number densities might change through outmixing and entrainment of air in clouds. It will require future investigations to explore the consequences of mixing effects for OAD-induced ice nucleation.

Notwithstanding the answers to these questions, the present work demonstrates that oxalic acid is likely to play a considerable role in the Earth's climate system.

Appendix A: Vapor pressure of aqueous oxalic acid particles

Vapor pressures of aqueous oxalic acid solutions were obtained using a single levitated oxalic acid aqueous solution particle in an electrodynamic balance. Details of the experimental setup of the electrodynamic balance and its analytical capabilities are given in Colberg et al. (2004). For the measurements of vapor pressures of semivolatile compounds in aqueous solutions, the relative humidity in the experimental chamber is kept constant while the gas phase vapor pressure of the organic compound is kept infinitely small by means of a continuous flow of a N_2/H_2O gas mixture through the chamber. Mie resonance spectroscopy is used to monitor the radius change of the particle due to loss of the organic compound to the gas phase (Chylek et al., 1983). To follow a resonance peak as a function of time, a point source broad band LED (centered at 585 nm) is used to illuminate the particle. A spectrograph with CCD detector records the spectrum of the elastically backscattered light (Zardini et al. manuscript in preparation). Thus, the radius and its change with time at a chosen temperature and relative humidity can be determined. The vapor pressure is then calculated using the evaporation equation. The vapor pressures as a function of temperature, $p_{\text{vap}}(T)$, follow the Clausius-Clapeyron equation,

$$p_{\text{vap}}(T) = p_0 \exp \left[-\frac{\Delta H}{R} \cdot \left(\frac{1}{T} - \frac{1}{T_0} \right) \right], \quad (5.5)$$

where p_0 is the vapor pressure of a liquid solution at the reference temperature T_0 and ΔH the evaporation enthalpy in Jmol^{-1} . To calculate the vapor pressure from the particle radius change, the density of the aqueous oxalic acid solution has to be known. Since no accurate experimental data is available, we calculated the vapor pressures given in Table 5.3 for two different realistic densities for the aqueous solutions (ρ_{aq}). The uncertainty of the vapor pressures of 15% is mainly due to the error in absolute radius, originating from the finite resolution of the spectrograph used.

For a tropospheric aerosol containing liquid particles with an oxalic acid concentration of

2 wt% at cirrus temperatures, a previous nucleation event will result in the crystallization of OAD together with ice. The low OAD vapor pressure leads to the growth of the OAD crystals at the expense of the oxalic acid in the liquid particle. Thus one can estimate whether the gas phase transport from a liquid aerosol particle to a solid OAD crystal occurs on timescales of atmospheric relevance.

The growth of a spherical particle to the radius of r_0 can be described as (Fahey et al., 2001),

$$r_0^2 = 2VD_g^*(n_g - n_{\text{vap}}^{\text{OAD}})\Delta t, \quad (5.6)$$

where V is the molecular volume of OAD, D_g^* is the effective gas phase diffusion coefficient of oxalic acid in air, n_g and $n_{\text{vap}}^{\text{OAD}}$ are the gas phase and equilibrium oxalic acid concentrations over OAD and Δt is the time needed for a particle to grow to the size of r_0 .

D_g^* can be expressed by the diffusion coefficient over a bulk phase (D_g) and a kinetic reduction factor due to small particle radii:

$$D_g^* = \frac{D_g}{1 + \frac{4D_g}{r\bar{v}}}, \quad (5.7)$$

where r and \bar{v} are the radius and the mean thermal velocity of the particle. D_g can be estimated with the diffusion coefficient of water vapor (Pruppacher and Klett, 1997) and an adjustment factor due to the different masses of water and oxalic acid.

$$D_g = 0.211 \cdot \left(\frac{T}{T_0}\right)^{1.94} \cdot \frac{p_0}{p} \cdot \sqrt{\frac{\mu_{\text{H}_2\text{O}}}{\mu_{\text{OA}}}} \quad (5.8)$$

where T and p are the temperature and pressure of the growing particle. T_0 and p_0 are 298 K and 1013 mbar. $\mu_{\text{H}_2\text{O}}$ and μ_{OA} are the reduced masses of water molecules in air and oxalic acid molecules in air, respectively. \bar{v} can be expressed as:

$$\bar{v} = \sqrt{\frac{8RT}{\pi M_{\text{OA}}}}. \quad (5.9)$$

Here, M_{OA} is the molar mass of oxalic acid.

Assuming a constant volume of the air mass, n_g can be determined by means of the ideal gas law. The rate at which the solid particles grow by gas phase transport of oxalic acid proceeds can be obtained assuming $p_{\text{vap}}^{\text{OAD}}=0$ and calculating p_g for a 2 wt% aqueous solution based on Raoult's law and ideal solutions. Thus a new particle grows at $T = 235$ K in ~ 33 hours to a size of $0.1 \mu\text{m}$.

Appendix B: Microphysical box model

To estimate the influence of OAD on the ice number density of cirrus clouds, the microphysical box model described by Hoyle et al. (2005) was used. So far, in this model only

Table 5.3: Vapor pressure measurements (p_{vap}) of two liquid oxalic acid droplets with an electrodynamic balance at different temperatures (T) and constant relative humidities (RH). ρ_{aq} is the estimated density of the aqueous oxalic acid solution.

$T = 282.7 \text{ K}$	$RH = 85.0 \%$	$T = 268.2 \text{ K}$	$RH = 84.5 \%$
$\rho_{\text{aq}}=1.1 \text{ gcm}^{-3}$	$p_{\text{vap}} = 5.9 \cdot 10^{-3} \text{ Pa}$	$\rho_{\text{aq}}=1.1 \text{ gcm}^{-3}$	$p_{\text{vap}} = 9.1 \cdot 10^{-4} \text{ Pa}$
$\rho_{\text{aq}}=1.3 \text{ gcm}^{-3}$	$p_{\text{vap}} = 5.0 \cdot 10^{-3} \text{ Pa}$	$\rho_{\text{aq}}=1.3 \text{ gcm}^{-3}$	$p_{\text{vap}} = 7.7 \cdot 10^{-4} \text{ Pa}$
$\Delta H/R = 9800 \pm 500 \text{ K}$			

homogeneous ice nucleation has been considered. In the presence of an IN, such as OAD, the total ice nucleation rate, R_{tot} , is given by

$$R_{\text{tot}}(T) = j_{\text{hom}}(T) \cdot V_{\text{liquid}} + j_{\text{het}}(T) \cdot S_{\text{OAD}}, \quad (5.10)$$

where $j_{\text{hom}}(T)$ and $j_{\text{het}}(T)$ are the homogeneous and heterogeneous ice nucleation rate coefficients at temperature T , respectively. V_{liquid} and S_{OAD} are the volume of the liquid droplet and the surface of the ice nucleus, which both can be determined based on field data or laboratory experiments. j_{hom} is described according to Koop et al. (2000), while j_{het} can be determined by the DSC freezing points experiments carried out in this study. In the DSC experiments the cooling rates and the sample volumes are equal for the homogeneous and heterogeneous ice nucleation and ΔT_{het} is rather small (see Table 5.2). Moreover, the width of the heterogeneous and homogeneous freezing peaks in the DSC are similar. Therefore, the homogeneous, $R_{\text{hom}}(T_1)$, and heterogeneous, $R_{\text{het}}(T_2)$, nucleation rates are approximately equal for both experiments:

$$\begin{aligned} R_{\text{hom}}(T_1) &\simeq R_{\text{het}}(T_2) \\ j_{\text{hom}}(T_1) \cdot V_{\text{liquid}} &\simeq j_{\text{het}}(T_2) \cdot S_{\text{OAD}}. \end{aligned} \quad (5.11)$$

T_1 is the homogeneous freezing temperature of the reference sample and T_2 the heterogeneous freezing temperature of the second cycle (see Table 5.2). V_{liquid} is calculated using the mean diameter of the emulsion droplets of $4 \mu\text{m}$. The surface of the OAD is determined by assuming that all oxalic acid in a particle is incorporated in a spherical crystal. Based on this assumption $j_{\text{het}}(T_{\text{het}})$ can be estimated for the measured freezing points. Parameterization of the heterogeneous freezing temperatures in terms of a constant water activity offset with respect to the ice melting point curve as done in Section 5.1 allows to calculate j_{het} at any given temperature and a_w by,

$$j_{\text{het}}(a_w, T) = \frac{V_{\text{liquid}}}{S_{\text{OAD}}} \cdot j_{\text{hom}}(a_w + \delta a_w^{\text{avg}}, T), \quad (5.12)$$

where $\delta a_w^{\text{avg}} = \Delta a_{w,\text{hom}} - \Delta a_{w,\text{het}} = 0.02$ (see Fig. 5.2).

With these nucleation rate coefficients it is possible to calculate the total nucleation rate of an air parcel containing background aerosol particles as well as OAD IN. Aerosol properties are taken from the PACE-7 campaign over the northwestern Pacific Ocean in 2000, since in this field study, the concentration of oxalic acid (collected on Teflon filters, Narukawa et al., 2003b) as well as the size distribution of the background aerosol (Zaizen et al., 2004) have been measured at several heights in the upper troposphere. For the initial aerosol size distribution of the model, mean values of several flights at 11 km of the PACE-7 campaign are used. The size distribution and surface areas of the OAD nano-crystals are estimated starting from an oxalic acid concentration of uniformly 2 wt% in the liquid phase. Solid OAD nano-crystals that form in a first homogeneous freezing event result in an ice particle number density according to the solid lines in Fig. 5.5. In all nucleated ice particles, the oxalic acid is assumed to crystallize fully to OAD. The OAD particles then grow by a Bergeron-Findeisen type process at the expense of the liquid aerosol particles.

In the atmosphere, gravity waves and turbulence lead to mesoscale cooling rates which are in most cases clearly larger than the synoptic scale cooling rates (Hoyle et al., 2005). One has to take into account that the cooling rate at the moment of the nucleation is crucial for the nucleation process itself. For the SUCCESS campaign (Subsonic Aircraft: Contrail and Cloud Effects Special Study) we have converted measurements of the vertical winds to mesoscale cooling rates (black dashed line in Fig. 5.4). The same Monte-Carlo techniques as in Hoyle et al. (2005) are used here to simulate the number density of ice particles by homogeneous nucleation alone and by homogeneous together with heterogeneous nucleation. For this purpose a simplified synoptic scale trajectory with a cooling rate of 0.2 K h^{-1} was assumed, and this trajectory was calculated repeatedly (4000 times) with superimposed mesoscale temperature fluctuations to obtain the ice number density for homogeneous ice nucleation (red line in Fig. 5.5). For the subsequent heterogeneous nucleation cycle, the number density of the OAD and their surface area distribution were calculated by modeling their formation during a first freezing cycle as explained above. The number density of OAD in each simulation was chosen stochastically from the calculated ice number density after the first homogeneous freezing cycle. This time the trajectory was calculated 4000 times with varying overlaying mesoscale fluctuations (see dashed lines in Fig. 5.5).

Appendix C: Global climate model (ECHAM4)

The cirrus scheme described by Lohmann and Kärcher (2002) was used for the ECHAM4 model simulation. The homogeneous freezing parameterization uses temperature, aerosol number density, and updraft speeds empirically corrected for subgrid-scale variability to determine the number concentration of newly formed ice crystals, n_i , in a given model time step Δt . The evaluation of n_i is based on a nucleation rate expression that links the rate with temperature and water activity in the freezing aerosol (Koop et al., 2000). The

latter is approximated by the ambient relative humidity in order to obtain an analytical solution. For homogeneous freezing to occur within one time step, the adiabatic cooling from a constant updraft speed has to exceed the critical supersaturation. The climate model then uses n_i and integrates prognostic equations for the cloud ice mass mixing ratio and ice crystal number concentrations. The climate model simulation was conducted in T30 horizontal resolution ($3.75^\circ \times 3.75^\circ$) with 19 vertical levels and a 30 minute time-step for one full year after an initial spin-up of 3 months using climatological sea surface temperatures and sea ice extent.

Acknowledgements

We are grateful for support by the Swiss National Fund in various projects and by the European Commission through the integrated project SCOUT-O3.

5.2 Nonadecanol and heterogeneous ice nucleation in the atmosphere

So far, just a few studies have measured long chain alcohols in the atmosphere (marine and urban sites), whereas typical concentrations of a few nano grams per cubic meter sampled air were observed (Gagosian et al., 1981; Simoneit et al., 1991; Stephanou, 1992; Nolte et al., 2001). It was found that the burning of oak, eucalyptus, and pine is one biogenic source (Nolte et al., 2001), but there is increasing evidence that such hydrophobic films can have both biogenic and anthropogenic sources (Kanakidou et al., 2005). The measured samples usually consist of a mixture of alcohols with different chain lengths, whereas those alcohols with an even C-atom number are typically predominant compared to those with an odd C-atom number (Nolte et al., 2001). Despite the fact that the presence of long chain alcohols in the UT has not yet been proven, it seems likely that they can occur also at such high altitudes.

To adapt the observed ice nucleation ability of long chain alcohols to the atmosphere, two points have to be considered. Firstly, because of the low concentrations of these alcohols in the atmosphere, it seems reasonable that a liquid aerosol will just be partially covered. Secondly, since usually a mixture of different alcohols is observed, the surface coating will probably consist of a mixture of different alcohols. Popovitz-Biro et al. (1994) have shown that the heterogeneous ice freezing temperature of a large droplet covered with an equally concentrated mixture of the C28 and C30 alcohol is reduced by ~ 10 K compared to the freezing temperatures of droplets covered with either pure C28 or C30.

The microphysical box model described in Section 5.1 was slightly adapted to estimate the change in ice particle radius (r_{ice}) and ice number density (n_{ice}) of droplets nucleated heterogeneously on a nonadecanol surface compared to homogeneously frozen ice particles. This time, an parcel starts its trajectory at 200 K and was cooled linearly with 10 K h^{-1} , whereas no overlaying mesoscale temperature fluctuations are included. An ice water content of 616 g cm^{-3} was used for the simulations. $j_{het}(T)$ of droplets covered with nonadecanol is parameterized with the function derived in Chapter 4.1, whereas j_{hom} is again adopted from (Koop et al., 2000). Further it is assumed that j_{het} is constant for any $\Delta a_{w,h}$. The initial aerosol distribution is described by a lognormal distribution with a mode radius of 25 nm and a σ of 1.6. It is assumed that all aerosols have a 10% partial coverage of long chain alcohols. Two case studies have been investigated. Firstly, the coverage consists of a nonadecanol monolayer and in a second case, it consists of a mixture of different long chain alcohols. In doing so, it is assumed, that droplets covered with a mixture of different long chain alcohols have a 10 K lower freezing temperature than those covered with pure nonadecanol. Further a 10 times smaller heterogeneous nucleation rate is taken for the partially covered droplets compared to the fully covered ones.

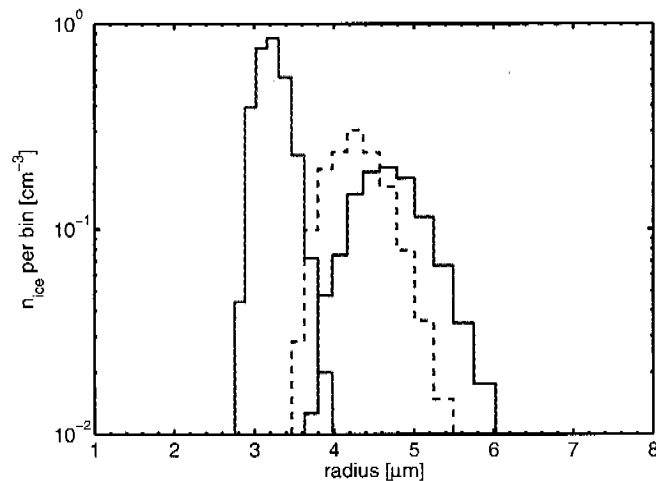


Figure 5.7: Radius of ice particles as a function of ice number density per bin (n_{ice}) for droplets nucleated homogeneously (red line) or heterogeneously (blue lines) on nonadecanol. Solid blue line: 10% of the droplets surface is covered with nonadecanol. Dashed blue line: 10% of the droplets surface is covered with a mixture of long chain alcohols, implying a reduction in the freezing temperature of 10 K compared to droplets covered with nonadecanol.

Figure 5.7 shows preliminary simulations of droplets frozen either homogeneously or heterogeneously on nonadecanol. Heterogeneous ice nucleation for the mixed and pure surfactant coverage leads to a 3-4 times smaller maximal size distribution compared to homogeneous ice nucleation, to larger ice particles and to a broader range in radius distribution. Since all droplets are covered with nonadecanol, homogeneous ice nucleation did not take part in the simulations with the covered droplets, which is in contrast to the simulations with OAD. The reduced ice number density and the larger particles radii result from the weak steepness of j_{het} as a function of temperature (see Fig. 4.5). This indicates that the firstly frozen larger aerosols have sufficient time to grow, before the next aerosols nucleate to ice. Larger ice particles lead to an enhancement in sedimentation and in a lower optical depth of such a cirrus cloud. This first result indicates clearly heterogeneous ice nucleation on nonadecanol could considerably influence cirrus cloud formation. However, so far the simulations are far away from realistic atmospheric conditions. The influence of the partial coverage on the freezing temperature and measurements of long chain alcohols in the UT are needed for further simulations. The first issue is discussed in the next paragraph.

Preliminary experiments of droplets covered partially with nonadecanol have been investigated to estimate the influence of a partial coverage on the heterogeneous ice freezing temperature (see Fig. 5.8). The experiments are performed in the DSC, and the nonadecanol is arranged at the air/water interface. Each data series consists of 12 to 48 single freezing experiments of 3 μl droplets. The droplets are placed with a pipette onto the DSC

pan and for each degree of coverage the concentration of the nonadecanol/hexane solutions was chosen by calculating the numbers of molecules needed from the target coverage. The DSC pan was sealed with a vacuum grease to prevent the droplets from water evaporation. A microscope picture was taken at the beginning and the end of an experiment, and thus one can be sure that no water evaporates from the droplets during the experimental observation time. Figure 5.8 shows a rather surprising picture, namely that the median freezing temperatures of the droplets just slightly change until a coverage of $\sim 10\%$ is obtained. The median freezing temperatures of the two data series with less than 10% coverage are still considerably higher than the median freezing temperature of the uncovered water droplet. This indicates, that liquid aerosols with a low partial coverage of nonadecanol can induce heterogeneous nucleation at distinctly higher temperatures compared to an uncovered droplet. Note that the uncovered droplet is not frozen homogeneously, but ice nucleation was rather induced by the surface of the DSC pan. Therefore, the difference between a homogeneously and a heterogeneously frozen droplet with a partial coverage of nonadecanol will even be larger. One future aim will be to include the freezing temperature dependence of the partial coverage of the nonadecanol into the microphysical box model.

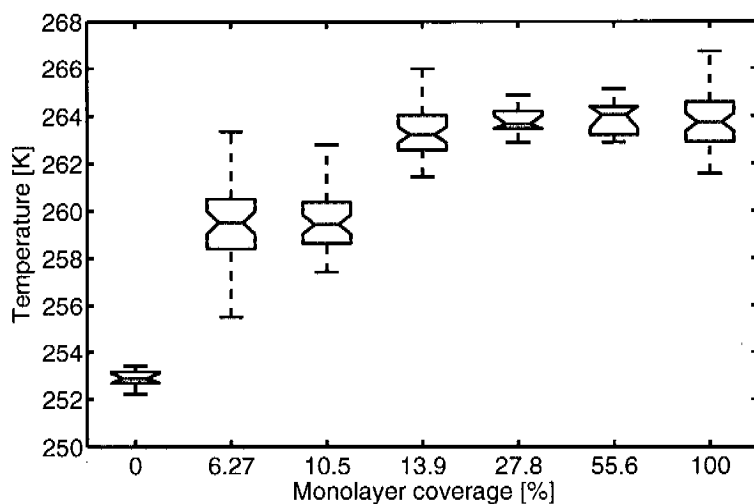


Figure 5.8: Box and whisker plot of heterogeneous freezing temperatures of large droplets as a function of nonadecanol coverage of the droplets (Note the nonlinear x axis scale). Each series consists of 12 to 48 single freezing point measurements. The red line depicts the median values, whereas the upper and lower horizontally black lines indicate the highest and lowest freezing temperatures of a series. The blue box shows the upper and lower quartile.

Chapter 6

Conclusions and Outlook

6.1 Conclusions

This thesis investigates various aspects of heterogeneous ice nucleation processes. Besides the atmospheric relevance, also a more general point of view of the phase transition of supercooled water to ice induced by heterogeneous nucleation has been considered. Therefore the requirements for the investigated IN included two major points. They have to have either an atmospheric relevance and/or convenient properties for heterogeneous freezing point experiments in the immersion mode. The experimental setups were chosen in such a way that the radius of the droplets and the experimental temperature range can be varied between $2\ \mu\text{m}$ to $1\ \text{mm}$ and from 150 to $273\ \text{K}$, respectively. On the other hand, the experimental setups allow solely investigating heterogeneous ice nucleation in the immersion mode, which constitutes just one major pathway for heterogeneous ice nucleation.

Heterogeneous ice nucleation rate coefficients of water droplets coated with nonadecanol

For the first time, heterogeneous rate coefficients of an ice nucleus over a temperature range of more than $10\ \text{K}$ have been experimentally determined. These experiments have been performed with nonadecanol arranged at a water/mineral oil interface, whereas a decrease of the droplet radius leads consequently to a smaller ice nucleus surface. The results indicate that the slope of j_{het} as a function of temperature has by far not the same steepness compared to homogeneous ice nucleation of supercooled liquid droplets or to heterogeneous ice nucleation of an ice nucleus with a rigid surface. It was found that CNT with a temperature dependent α agrees considerably well with the measurements. Molec-

ular arrangement and structural properties of long chain alcohols have been presented, which indicate that their arrangement at the droplet surface contributes strongly to their ice nucleation efficiency. However, neither the strong temperature dependence of α nor its physical meaning could be fully explained. Therefore, further studies, i.e., Molecular Dynamics simulations, are strongly demanded to understand the physics behind the freezing efficiency of long chain alcohols (Nutt and Stone, 2003). Despite the fact that CNT with a temperature dependent α can describe the measurements fairly well, it highlights also the weakness of this theory, namely that the parameter α is approximated by macroscopic interfacial tensions, whereas the nucleation process itself happens on a microscopic scale. Similar studies with other IN could help to gain more knowledge on α , which could lead to an improvement of CNT or our view of heterogeneous ice nucleation.

Heterogeneous freezing point experiments with different immersed IN

Heterogeneous freezing point experiments of various aqueous solutions with four different IN in the immersion mode (two organic and two inorganic) have been presented. The results show that water activity based nucleation theory with a constant $\Delta a_{w,\text{het}}$ for a specific ice nucleus agrees well with the measurements, whereas $\Delta a_{w,\text{het}}=0.101, 0.173, 0.180$ and 0.285 are determined for nonadecanol, silica, AgI and OAD, respectively. The agreement is even improved when the slight temperature dependence of a_w is considered, which is also found for several substances above the ice melting point (e.g., Clarke and Glew, 1985; Clegg et al., 1998; Eliassi et al., 1999). A comparison of the water activity based nucleation theory with the λ -approach shows that measurements of different studies are reproduced by both approaches with the same quality. However, since only the water activity based nucleation theory has a direct link to the atmosphere, this approach seems more persuasive.

Heterogeneous rate coefficients have been estimated from DSC freezing peaks by considering different determining reasons resulting in the shape of the freezing peak. The estimated value for j_{hom} of an emulsion of pure water is ~ 1 order of magnitude smaller compared with other measurements, but this deviation reflects the typical uncertainty range of these measurements. (Pruppacher and Klett, 1997). It was found that j_{het} for emulsions containing either AgI or OAD crystallites are within one order of magnitude for both series, indicating that for a constant $\Delta a_{w,\text{het}}$ also constant j_{het} can be assumed. The constant $\Delta a_{w,\text{het}}$ together with the corresponding constant j_{het} can be used to parameterize heterogeneous ice nucleation in the immersion mode in microphysical or global climate models.

The indirect aerosol effect of oxalic acid enriched particles on cirrus clouds

Heterogeneous ice freezing points of emulsified aqueous solutions containing different immersed solid dicarboxylic acids (oxalic, adipic, succinic, phthalic and fumaric acid) have been measured with a differential scanning calorimeter. It was found that only oxalic acid acts as an ice nucleus, whereas ΔT_{het} lies between 2-5 K depending on solution composition. Single particle aerosol mass spectrometry has observed solid OAD in several field campaigns in the UT. Therefore microphysical box model simulations have been carried out to estimate the possible effect of OAD nano-crystals in aerosols on cirrus cloud properties. The results indicate that the ice number density (n_{ice}) of cirrus clouds containing solid OAD is reduced by $\sim 50\%$ when compared to ice particles that exclusively formed by homogeneous nucleation. Such a reduction leads to optically thinner cirrus clouds and an enhancement in sedimentation of ice particles. A comparison of global simulations with the ECHMA4 climate model of cirrus clouds formed with and without OAD nano-crystals leads to a radiative net forcing of -0.3 Wm^{-2} , indicating the importance of heterogeneous ice nucleation for global climate.

Nonadecanol and heterogeneous ice nucleation in the atmosphere

Preliminary simulations with the 1D microphysical model indicate that aerosols partially covered with either pure nonadecanol or a hypothetical mixture of different long chain alcohols leads to a 3-4 times smaller maximal size distribution compared to homogeneous ice nucleation, which shows that the heterogeneously frozen ice particles had sufficient time to deplete the gas phase. Heterogeneously nucleated ice particles are further larger in size and show a broader range in radius distribution. Such larger ice particles lead to an enhancement in sedimentation and in a lower optical depth of a cirrus cloud.

So far, the freezing temperature dependence of the partial coverage of the nonadecanol has not yet been included in the microphysical box model, which has to be taken into account in future simulations. Further field data concerning the concentrations and appearances of long chain alcohols should be expanded to the UT, to estimate the influence of heterogeneous ice nucleation on nonadecanol more accurately.

6.2 Outlook

General questions concerning the formation and occurrence of cirrus clouds are still unresolved. Namely what is the exact pathway for cirrus cloud formation, or is it possible to distinguish whether homogeneous or heterogeneous ice nucleation are more important for

different altitudes and/or different regions? The knowledge of the microphysical processes behind homogeneous and heterogeneous ice nucleation will significantly contribute to answer these questions.

So far, the homogeneous ice nucleation process is well parameterized, but water activity measurements of supercooled aqueous solutions would help to strengthen the conclusion of Koop et al. (2000). The results of this study show that immersion nucleation can be similar parameterized similarly to homogeneous ice nucleation, but there is still no general understanding of the other heterogeneous pathways. Therefore equivalent studies, i.e., investigation of different IN in the deposition, contact, and condensation mode could deepen the understanding of heterogeneous ice nucleation process in general.

The impact of OAD on cirrus cloud formation and the global net radiative forcing indicate that even a rather weak ice nucleus has the potential to influence the microphysical properties of cirrus clouds as well as their radiative effects. Field campaigns, such as CRYSTAL-FACE, are highly demanded to determine the compositions of IN, which could certainly change due to anthropogenic emission. Information of the composition together with microphysical experiment and modeling studies as well as radiative calculations would enlarge the understanding of the formation of cirrus clouds as well as their impact on global climate change.

Appendix A

Temperature calibrations

For each experimental setup an accurate temperature calibration is needed, which are discussed individually. Besides absolute temperature calibrations, also different phase transition processes have to be treated separately. For example in the DSC, freezing of an aqueous solution and melting of ice results in different heat flow curves, and thus a suitable calibration has to be performed for both processes. Further, different masses, cooling rates and concentrations of the aqueous solutions have to be distinguished for the calibrations.

A.1 DSC

A.1.1 Absolute temperature calibration

The absolute temperature of the DSC is calibrated with the ice melting point of water and the ferroelectric phase transition of $(\text{NH}_4)_2\text{SO}_4$ (Tab. A.1). The differences to the literature values are saved in the calibration file of the DSC software. Therefore, the absolute temperature correction is automatically executed by the DSC software. A linear fit through these two data points is used by the software to adjust the temperature during an experimental run. Note, that for measurements at higher temperatures ($T \gtrsim 350$ K), an additional calibration point (e.g., melting point of indium) would be recommended. Further, to avoid a slight change in the absolute temperature of the DSC, the calibration should be checked every three months.

A.1.2 Freezing point calibration

If the cooling rate in a DSC experiment is increased, the onset of the freezing peak is shifted to smaller temperatures. Therefore, a freezing point or cooling rate calibration has been performed for three different cooling rates, in which solely the ferroelectric phase

Table A.1: Absolute temperature calibration of the DSC performed with the melting point of water and the ferroelectric phase transition of $(\text{NH}_4)_2\text{SO}_4$. T_{cal} is the median temperature of 4 independent measurements and T_{lit} is the corresponding literature value. The heating rate for all measurements is 1 Kmin^{-1} .

Substance	mass [mg]	T_{cal} [K]	T_{lit} [K]	$T_{\text{cal-lit}}$ [K]
$(\text{NH}_4)_2\text{SO}_4$	4	$224.21 \pm 0.05 \text{ K}$	223.10^\dagger	1.11
water	4	$273.45 \pm 0.05 \text{ K}$	273.15	0.3

† Knopf (2003)

transition temperature of $(\text{NH}_4)_2\text{SO}_4$ is used as a calibration point (Tab. A.2). Thus, it is assumed that this calibration is independent of the absolute temperature.

Table A.2: Freezing point or cooling rate calibration of the DSC performed at the ferroelectric phase transition temperature of $(\text{NH}_4)_2\text{SO}_4$. T_f is the median freezing point of four independent samples. The calibration is valid for emulsions and large droplets ($1 \text{ ml} \leq V \leq 10 \text{ ml}$). Example: The onset of the freezing peak of an emulsion cooled with 10 Kmin^{-1} gives a temperature of 225.3 K , hence the calibrated temperature is 226.96 K .

Cooling rate [Kmin^{-1}]	T_f [K]	Pan	Temperature correction [K]
3	223.41 ± 0.03	small	+0.80
10	223.10 ± 0.08	small	+1.11
1	223.41 ± 0.04	large	+0.80
3	223.16 ± 0.03	large	+1.05
10	222.55 ± 0.10	large	+1.66

A.1.3 Melting point calibration

As seen in Fig. 3.4, the emulsion, made of an aqueous solution, starts to melt as soon the it has passed the eutectic temperature in the phase diagram. On the other hand, a pure substance, will not melt until its final melting temperature is reached. Therefore, one has to distinguish the melting point calibration for pure substances (c.g., ice) and aqueous solutions samples.

Pure substances

The calibration for pure substances is performed with the ferroelectric phase transition of $(\text{NH}_4)_2\text{SO}_4$ and the ice melting point of water (Tab. A.3). Since both substances will not melt before the final melting point temperature is achieved, the melting point temperatures are read out with the onset of the melting peak.

Emulsified aqueous solutions

The melting point calibration of emulsified aqueous solutions is based on the ice melting points of well known aqueous systems. As mentioned before, the ice starts to melt inside the droplets as soon the temperature of the sample is larger than the eutectic melting point temperature. Thus, the minimum of the ice melting peak is used to determine the final ice melting point temperature. However, because the size of a melting peak is increasing with decreasing concentration of the solution, two different temperature area are distinguished (Tab. A.4), which is found as the intercept point between the two fit functions (see bottom row in Tab. A.4).

A.1.4 Accuracy and precision of the different calibrations

Although, the emulsions are highly reproducible, there exists a variability of freezing temperature between different emulsions of ± 0.5 K, probably because of slightly varying size distributions. This effect is distinctly smaller for the melting point, namely ± 0.1 K. Note that the precision of freezing points in a single emulsion is distinctly smaller than 0.2 K. The accuracy of the freezing and melting points calibrations is ± 0.5 K and ± 0.4 K, respectively. Therefore the total error in freezing and melting temperature is ± 1.0 K and ± 0.5 K, respectively.

A.2 Single droplet cooling stage

The absolute temperature calibration were performed with the melting points of four different organic solvents. For all experiments a heating rate of 1 Kmin^{-1} was used. A thin film of the organic solvent was placed on a regular glass substrate and the melting point was detected optically (Dobler (2003), Tab. A.5). A best fit trough the data of Tab. A.5 leads to,

$$T_{\text{abs}} = 1.00099 \cdot T_{\text{cell}} - 0.325K \quad (\text{A.1})$$

where T_{abs} and T_{cell} are the calibrated and the measured temperature in Kelvin. The accuracy of the calibration is ± 0.20 K. Since just moderate cooling rates ($\text{max } 3 \text{ Kmin}^{-1}$)

Table A.3: Melting point calibration for pure substances with different pans and sample types. T_m is the measured melting point of four independent samples. The two samples in the large pan with the heating rate of 1 Kmin^{-1} are already corrected with the absolute temperature calibration (see Tab. A.1). Therefore no correction has to be made.

substance	Heating rate (Kmin^{-1})	T_m [K]	Pan	Correction [K]
$(\text{NH}_4)_2\text{SO}_4$	10	224.26 ± 0.02	small	-0.05
$(\text{NH}_4)_2\text{SO}_4$	10	224.81 ± 0.10	large	-0.60
water	10	273.60 ± 0.03	small, emulsion	-0.15
water	10	273.86 ± 0.06	large, emulsion	-0.41
water	10	274.06 ± 0.08	large, large droplet	-0.61
$(\text{NH}_4)_2\text{SO}_4$	1	223.90 ± 0.04	small	+0.31
$(\text{NH}_4)_2\text{SO}_4$	1	224.21 ± 0.11	large	no correction
water	1	273.47 ± 0.05	small, emulsion	-0.02
water	1	273.45 ± 0.10	large, emulsion	no correction
water	1	273.71 ± 0.01	large, large droplet	-0.26

Table A.4: Melting point calibration for emulsified aqueous solution samples in the large pan. The heating rate is always 1 Kmin^{-1} . EG and AS are ethylene glycol and $(\text{NH}_4)_2\text{SO}_4$, respectively. T_m and T_{lit} are the measured melting point and the corresponding literature value, respectively. In the bottom row of the Table, the two fit functions for the melting point calibrations are listed.

$T_m < 269.2 \text{ K}$				$T_m > 269.2 \text{ K}$			
substance	conc. [wt%]	T_m [K]	T_{lit} [K]	substance	conc. [wt%]	T_m [K]	T_{lit} [K]
EG	20.0	265.28	265.22^\dagger	EG	1.0	273.76	272.85^\dagger
EG	30.0	258.24	257.95^\dagger	EG	5.0	272.27	271.57^\dagger
EG	42.9	245.43	246.00^\dagger	EG	10.0	270.06	269.78^\dagger
EG	48.1	239.39	239.85^\dagger	AS	5.6	272.16	$271.45^\#$
$T_{\text{cal}} = 0.99368 \cdot T_m + 1.54$				$T_{\text{cal}} = 0.82741 \cdot T_m + 46.31$			

† Lide (1998), $^\#$ Clegg et al. (1998)

Table A.5: Absolute temperature calibration with four organic solvents. T_{cell} and T_{lit} are the median melting temperature of 10 independent samples and the corresponding literature values (Lide, 1998), respectively.

substance	T_{cell} [K]	T_{lit} [K]	$T_{\text{cell-lit}}$ [K]
tetradecane	278.97 ± 0.05	278.95^\dagger	0.02 ± 0.05
dodecane	263.60 ± 0.1	263.50^\dagger	0.10 ± 0.1
decane	243.54 ± 0.1	243.45^\dagger	0.09 ± 0.1
octane	216.45 ± 0.04	216.35^\dagger	0.1 ± 0.04

† Lide (1998)

are used, a separate cooling rate calibration was not performed.

Measured ice melting points of various aqueous solution droplets were calibrated with Eq. A.1. It was found that the calibration fits just nicely for melting points below 262 K. Therefore, at higher temperatures an additional calibration for the melting temperature has to be investigated with aqueous solutions droplets. The resulting data are fitted with a new function.

$$T_{\text{abs}} = -0.0091K^{-1} \cdot T_{\text{cell}}^2 + 5.7997 \cdot T_{\text{cell}} - 632.62K, \quad (\text{A.2})$$

where T_{abs} and T_{cell} are the calibrated and the measured temperature in Kelvin. The accuracy of the calibration is again ± 0.20 K.

Summarized, the calibration function (Eq. A.1) must be used for the freezing points and the melting points below 262 K. For melting points above 262 K, the calibration function (Eq. A.2) is used.

A.3 Linkam cooling stage

The absolute temperature calibration for the Linkam cooling stage was investigated with the melting points of five different organic solvent (dodecane, tetradecane, pentadecane, heptadecane and diphenyl ether) (Gasser and Jöri, 2004). Thereby, a thin film of the solvent was spread onto the glass substrate and cooled until the solvent crystallized. The sample was then heated with a rate of 1 Kmin^{-1} until the melting point was detected optically. A best fit through the data leads to,

$$T_{\text{abs}} = 0.9760114 \cdot T_{\text{Linkam}} + 0.63 \quad (\text{A.3})$$

where T_{abs} and T_{Linkam} are the calibrated absolute and the measured temperatures in Kelvin, respectively. The R^2 of the linear fit is 0.9999. This leads to an accuracy of the absolute temperature of ± 0.2 K. Because of the small sample volume a dynamical calibration was not performed.

Seite Leer /
Blank leaf

Appendix B

Statistical analysis of the single droplet measurements

B.1 Comparison of the freezing temperatures of droplets covered with nonadecanol at the air/water and at the oil/water interface

The measurements in chapter 4.1 to determine the heterogeneous rate coefficient were performed with droplets covered with a nonadecanol/mineral oil solution. In contrast, Gavish et al. (1990) investigated their experiment with the long chain alcohols at the air/water interface. To insure, that the droplets measured in this study are fully covered and the nonadecanol has the same nucleation efficiency at the oil/water interface as at the air/water interface, series of both experimental approaches are compared with the Wilcoxon rank sum test on a 5% level. This test determines at what significance level two populations or data series of single droplets measurements are shifted with respect to each other. The null hypothesis, h , is rejected (i.e., $h=1$), when the two populations are significantly different. The h and p value of Tab. B.1 indicates that the droplets covered

Table B.1: *Statistical comparison of the freezing temperature of droplets covered with nonadecanol at the air/water and at the oil/water interface with the Wilcoxon rank sum test on a 5% level*

air/water interface: 135 freezing points	oil/water interface : 25 freezing points	$h=0$ $p=0.1273$
---	---	---------------------

with the nonadecanol/mineral oil solution are fully covered and that nonadecanol has the same nucleation efficiency at the oil/water as at the air/water interface, i.e., $h=0$.

B.2 t-test for the slopes of series of single droplets

To analyze the data series of single droplets with the poisson statistics, it is important that the individual freezing events have the same conditions as those before and those afterwards. Therefore the slope of such data series must not show any trend. The t-test gives a statistical answer, whether the slope of the data series is zero or not. The slopes of the six data series used in chapter 4.1 are treated with a t-test on a 5% level. If the resulting p value is smaller than 0.1, the hypothesis of a constant slope must be rejected. Otherwise the assumption that the slope of the series is zero can be accepted.

Table B.2: *t*-test statistics for the slopes of the data series in Fig. 4.2, whereas the same symbols as in Fig. 4.2 are shown. If $p > 0.1$, the slopes of the series is accepted as zero, i.e. there is no trend in the data series

Series:	number of freezing points	p
□	92	0.878
○	95	0.877
◇	98	0.776
▽	72	0.303
▷	50	0.192
★	68	0.928

B.3 Upper and lower limits of the poisson statistics

Table B.3 shows the upper and lower freezing event limits of the poisson statistics on the 95% confidence level (Beyer, 1987). This means that, if 7 freezing events are measured in a specific, it would also be statistically plausible to observe 2.8 to 14.4 freezing events. Therefore for each measured j_{het} an upper and lower heterogeneous rate coefficient can be calculated according to Eq. 2.38.

Table B.3: Lower ($n_{\text{nuc,low}}$) and upper $n_{\text{nuc,up}}$ freezing event limits of the poisson statistics on the 95% confidence level for $n_{\text{nuc}} = 0-50$.

$n_{\text{nuc,low}}$	n_{nuc}	$n_{\text{nuc,up}}$	$n_{\text{nuc,low}}$	n_{nuc}	$n_{\text{nuc,up}}$
0	0	3.7	17.0	26	38.0
0.1	1	5.6	17.8	27	39.2
0.2	2	7.2	18.6	28	40.4
0.6	3	8.8	19.4	29	41.6
1.0	4	10.2	20.2	30	42.8
1.6	5	11.7	21.0	31	44.0
2.2	6	13.1	21.8	32	45.1
2.8	7	14.4	22.7	33	46.3
3.4	8	15.8	23.5	34	47.5
4.0	9	17.1	24.3	35	48.7
4.7	10	18.4	25.1	36	49.8
5.4	11	19.7	26.0	37	51.0
6.2	12	21.0	26.8	38	52.2
6.9	13	22.3	27.7	39	53.3
7.7	14	23.5	28.6	40	54.5
8.4	15	24.8	29.4	41	55.6
9.4	16	26.0	30.3	42	56.8
9.9	17	27.2	31.1	43	57.9
10.7	18	28.4	32.0	44	59.0
11.5	19	29.6	32.8	45	60.2
12.2	20	30.8	33.6	46	61.3
13.0	21	32.0	34.5	47	62.5
13.8	22	33.2	35.3	48	63.6
14.6	23	34.4	36.1	49	64.8
15.4	24	35.6	37.0	50	65.9
16.2	25	36.8			

Seite Leer /
Blank leaf

Appendix C

Heterogeneous freezing point measurements with different IN

In this chapter, the data of the freezing and melting points of the measurements with different ice nuclei are listed.

C.1 Large droplets covered with nonadecanol

The results of the droplets covered with nonadecanol discussed in Chapter 4.2.1 are listed in Tab. C.1. Besides the median freezing and melting points also the maximal and minimal value for each solution is tabulated.

C.2 Emulsions with immersed AgI

All the freezing point experiments of emulsified samples with immersed AgI discussed in Chapter 4.2.2 are listed in Tab. C.2.

C.3 Large droplets with suspended SiO₂

The heterogeneous freezing experiments of large aqueous solution droplets with SiO₂ globules are discussed in Chapter 4.2.3. Here, all measured data and the reference measurements of freezing points of large droplets without SiO₂ globules are tabled. Further the freezing temperatures of the series with and without are statistically compared with the Wilcoxon rank sum test on a 5% level with each other to ensure that the data series are distinguishable.

Table C.1: Heterogeneous freezing and melting points of different aqueous solution droplets covered with nonadecanol. All the droplets have a volume of 3 μl . C_{sol} is the initial concentration of the solution. n is the number of investigated droplets and $T_{\text{f,tot}}$ is the total number of freezing points. T_{med} , T_{max} and T_{min} are the median freezing, the maximal and the minimal temperature of all measured freezing and melting points, respectively. All temperatures are indicated in Kelvin. $a_{\text{w,med}}$ is the water activity calculated according to Eq. 2.26 with $T_{\text{m,med}}$ (See Section 4.3).

Solute	C_{sol} [wt%]	n	$T_{\text{f,tot}}$	$T_{\text{f,med}}$	$T_{\text{f,max}}$	$T_{\text{f,min}}$	$T_{\text{m,med}}$	$T_{\text{m,max}}$	$T_{\text{m,min}}$	$a_{\text{w,med}}$
H ₂ O	-	12	48	264.25	266.75	260.55	273.37	273.47	273.25	1.003
(NH ₄) ₂ SO ₄	5.59	18	66	260.55	264.00	256.45	270.99	271.07	270.82	0.979
(NH ₄) ₂ SO ₄	14.98	18	66	258.43	262.40	253.15	268.34	268.50	267.96	0.953
(NH ₄) ₂ SO ₄	23.90	12	48	252.45	256.60	247.80	264.85	265.08	264.09	0.920
(NH ₄) ₂ SO ₄	34.21	18	72	247.45	250.70	236.55	258.40	259.30	257.35	0.863
MgCl ₂	6.89	6	24	256.20	260.50	253.45	268.72	268.84	268.48	0.956
MgCl ₂	13.71	12	36	240.73	248.60	234.35	260.45	260.75	259.35	0.881
MgCl ₂	17.13	12	42	237.30	242.85	231.25	253.52	254.16	252.91	0.824
MgCl ₂	19.58	6	24	226.53	233.70	221.65	246.87	247.75	245.72	0.773
NaCl	15.11	6	24	248.73	250.40	241.70	260.10	260.56	259.93	0.878
NaCl	19.85	6	24	244.75	248.15	236.95	256.45	256.86	255.27	0.847
EG	30.01	6	24	246.53	251.40	239.15	258.79	259.08	257.00	0.867
EG	42.86	6	24	232.33	238.35	229.35	245.65	246.39	244.82	0.765
EG	48.08	6	24	224.38	230.60	220.80	239.60	240.26	239.00	0.724
Ca(NO ₃) ₂	29.81	6	24	248.73	254.45	244.65	259.43	259.99	257.93	0.872
Ca(NO ₃) ₂	43.84	12	42	225.90	232.15	216.75	243.68	244.22	242.52	0.751

Table C.2: Summary of the heterogeneous freezing experiments of various emulsified samples containing AgI. C_{sol} is the concentration of the additional solute. V_{add} , V_{AgNO_3} and V_{KI} are the volume of the additional solute, the 1.64 wt% AgNO_3 and the 1.61 wt% KI solution, respectively. $T_{\text{f,het}}$, $T_{\text{f,hom}}$ and T_{m} are the measured heterogeneous, homogeneous and ice melting points, respectively. Volumes and temperatures are indicated in ml and Kelvin, respectively. mol_{tot} is total mole fraction of the solution. a_{w} is the water activity of the solution at the ice melting point calculated with Eq. 2.26. The horizontal lines separate different emulsion.

Solute	C_{sol} [wt%]	V_{add}	V_{AgNO_3}	V_{KI}	$T_{\text{f,het}}$	$T_{\text{f,hom}}$	T_{m}	mol_{tot}	a_{w}
H ₂ O	-	0.4	0.1	0.1	255.00	235.67	273.16	$5.83 \cdot 10^{-4}$	1.000
H ₂ O	-	0.4	0.05	0.05	254.87	235.46	273.34	$3.49 \cdot 10^{-4}$	1.002
H ₂ O	-	0.4	0.05	0.05	254.92	235.41	273.35	$3.49 \cdot 10^{-4}$	1.003
H ₂ O	-	0.4	0.05	0.05	254.82	235.37	273.35	$3.49 \cdot 10^{-4}$	1.003
NaCH ₃ COO	19.5	0.4	0.1	0.1	244.70	223.89	267.12	$3.26 \cdot 10^{-2}$	0.9412
NaCH ₃ COO	19.5	0.4	0.1	0.1	244.74	224.01	267.13	$3.26 \cdot 10^{-2}$	0.9413
NaCH ₃ COO	19.5	0.4	0.1	0.1	244.77	223.82	267.13	$3.26 \cdot 10^{-2}$	0.9413
NaCH ₃ COO	28.3	0.4	0.05	0.05	226.52	202.26	255.28	$6.11 \cdot 10^{-2}$	0.8376
NaCH ₃ COO	28.3	0.4	0.05	0.05	226.49	202.29	255.28	$6.11 \cdot 10^{-2}$	0.8376
NaCH ₃ COO	28.3	0.4	0.05	0.05	226.50	202.31	255.28	$6.11 \cdot 10^{-2}$	0.8376
NaCH ₃ COO	28.3	0.4	0.1	0.1	232.98	211.97	259.99	$4.96 \cdot 10^{-2}$	0.8768
NaCH ₃ COO	28.3	0.4	0.1	0.1	232.96	211.96	259.99	$4.96 \cdot 10^{-2}$	0.8768
NaCH ₃ COO	28.3	0.4	0.1	0.1	232.98	211.96	259.99	$4.96 \cdot 10^{-2}$	0.8768
LiCl	2.0	0.4	0.05	0.05	252.68	233.11	271.61	$7.23 \cdot 10^{-3}$	0.9849
LiCl	2.0	0.4	0.05	0.05	252.66	233.14	271.61	$7.23 \cdot 10^{-3}$	0.9849
LiCl	7.7	0.4	0.05	0.05	245.95	224.32	266.77	$2.76 \cdot 10^{-2}$	0.9378
LiCl	7.7	0.4	0.05	0.05	246.15	224.34	266.77	$2.76 \cdot 10^{-2}$	0.9379
LiCl	14.9	0.4	0.1	0.1	239.69	215.51	261.38	$4.56 \cdot 10^{-2}$	0.8899
LiCl	14.9	0.4	0.1	0.1	239.72	215.55	261.38	$4.56 \cdot 10^{-2}$	0.8899
LiCl	14.9	0.4	0.1	0.1	239.71	215.57	261.38	$4.56 \cdot 10^{-2}$	0.8899
LiCl	19.9	0.4	0.05	0.05	223.41	191.43	246.54	$7.50 \cdot 10^{-2}$	0.7711
LiCl	19.9	0.4	0.05	0.05	223.41	191.52	246.55	$7.50 \cdot 10^{-2}$	0.7711
LiCl	19.9	0.4	0.05	0.05	223.38	191.61	246.55	$7.50 \cdot 10^{-2}$	0.7711
LiCl	19.9	0.4	0.1	0.1	231.75	204.49	254.34	$6.19 \cdot 10^{-2}$	0.8300
LiCl	19.9	0.4	0.1	0.1	231.87	204.56	254.34	$6.19 \cdot 10^{-2}$	0.8300
LiCl	19.9	0.4	0.1	0.1	231.86	204.60	254.32	$6.19 \cdot 10^{-2}$	0.8299
K ₂ CO ₃	17.9	0.4	0.05	0.05	244.22	222.68	267.53	$2.18 \cdot 10^{-2}$	0.9450
K ₂ CO ₃	17.9	0.4	0.05	0.05	244.42	222.77	267.54	$2.18 \cdot 10^{-2}$	0.9451
K ₂ CO ₃	17.9	0.4	0.05	0.05	244.44	222.76	267.54	$2.18 \cdot 10^{-2}$	0.9451
K ₂ CO ₃	35.1	0.4	0.05	0.05	221.74	194.59	256.34	$4.90 \cdot 10^{-2}$	0.8462
K ₂ CO ₃	35.1	0.4	0.05	0.05	222.46	194.38	256.34	$4.90 \cdot 10^{-2}$	0.8462
K ₂ CO ₃	35.9	0.4	0.1	0.1	224.00	197.28	257.40	$4.03 \cdot 10^{-2}$	0.8549
K ₂ CO ₃	35.9	0.4	0.1	0.1	225.36	197.04	257.39	$4.03 \cdot 10^{-2}$	0.8548

Table C.2 (continued)

Solute	C_{sol} [wt%]	V_{add}	V_{AgNO_3}	V_{KI}	$T_{\text{f,het}}$	$T_{\text{f,hom}}$	T_{m}	mol_{tot}	a_w
K ₂ CO ₃	35.9	0.4	0.1	0.1	225.42	199.15	258.08	4.03·10 ⁻²	0.8606
K ₂ CO ₃	35.9	0.4	0.1	0.1	225.96	199.09	258.08	4.03·10 ⁻²	0.8606
K ₂ CO ₃	35.9	0.4	0.1	0.1	226.36	199.08	258.08	4.03·10 ⁻²	0.8606
K ₂ CO ₃	35.9	0.4	0.1	0.1	226.50	199.05	258.08	4.03·10 ⁻²	0.8606
K ₂ CO ₃	35.9	0.4	0.1	0.1	226.60	199.02	258.08	4.03·10 ⁻²	0.8606
Glycerol	39.6	0.4	0.1	0.1	239.73	217.86	264.66	6.67·10 ⁻²	0.9183
Glycerol	39.6	0.4	0.1	0.1	239.75	217.88	264.66	6.67·10 ⁻²	0.9183
Glycerol	55.0	0.4	0.1	0.1	226.07	204.03	258.45	1.03·10 ⁻¹	0.8637
Glycerol	55.0	0.4	0.1	0.1	226.07	204.10	258.45	1.03·10 ⁻¹	0.8637
Glycerol	55.0	0.4	0.1	0.1	226.08	204.13	258.45	1.03·10 ⁻¹	0.8637
Ca(NO ₃) ₂	13.0	0.4	0.05	0.05	249.25	230.64	270.97	1.30·10 ⁻²	0.9785
Ca(NO ₃) ₂	13.0	0.4	0.05	0.05	249.08	230.58	270.97	1.30·10 ⁻²	0.9785
Ca(NO ₃) ₂	13.0	0.4	0.05	0.05	249.04	230.60	270.98	1.30·10 ⁻²	0.9785
Ca(NO ₃) ₂	29.8	0.4	0.05	0.05	237.84	212.82	261.98	3.38·10 ⁻²	0.8941
Ca(NO ₃) ₂	29.8	0.4	0.05	0.05	237.95	212.86	261.98	3.38·10 ⁻²	0.8941
Ca(NO ₃) ₂	29.8	0.4	0.05	0.05	237.85	212.84	261.96	3.38·10 ⁻²	0.8940
Ca(NO ₃) ₂	43.9	0.4	0.1	0.1	233.01	205.24	258.32	4.45·10 ⁻²	0.8626
Ca(NO ₃) ₂	43.9	0.4	0.1	0.1	232.86	205.65	258.32	4.45·10 ⁻²	0.8626
Ca(NO ₃) ₂	43.9	0.4	0.05	0.05	225.04	186.49	251.41	5.68·10 ⁻²	0.8072
Ca(NO ₃) ₂	43.9	0.4	0.05	0.05	225.03	187.49	251.40	5.68·10 ⁻²	0.8071
Ca(NO ₃) ₂	43.9	0.4	0.05	0.05	225.11	186.88	251.40	5.68·10 ⁻²	0.8071
Ethylene glycol	21.4	0.4	0.05	0.05	243.67	221.41	266.28	5.71·10 ⁻²	0.9332
Ethylene glycol	21.4	0.4	0.05	0.05	244.08	221.64	266.28	5.71·10 ⁻²	0.9332
Ethylene glycol	29.9	0.4	0.05	0.05	234.64	213.12	262.29	8.42·10 ⁻²	0.8969
Ethylene glycol	29.9	0.4	0.05	0.05	234.63	213.20	262.30	8.42·10 ⁻²	0.8970
Ethylene glycol	29.9	0.4	0.05	0.05	234.62	213.25	262.30	8.42·10 ⁻²	0.8970
Ethylene glycol	48.0	0.4	0.1	0.1	221.50	199.65	256.14	1.22·10 ⁻¹	0.8446
Ethylene glycol	48.0	0.4	0.1	0.1	221.71	199.89	256.15	1.22·10 ⁻¹	0.8447
Ethylene glycol	48.0	0.4	0.1	0.1	221.78	199.85	256.15	1.22·10 ⁻¹	0.8447
MgCl ₂	3.0	0.4	0.05	0.05	251.14	232.50	271.62	5.00·10 ⁻³	0.9850
MgCl ₂	3.0	0.4	0.05	0.05	251.19	232.53	271.62	5.00·10 ⁻³	0.9850
MgCl ₂	9.0	0.4	0.05	0.05	245.95	225.17	268.06	1.49·10 ⁻²	0.9501
MgCl ₂	9.0	0.4	0.05	0.05	246.40	225.15	268.07	1.49·10 ⁻²	0.9502
MgCl ₂	17.1	0.4	0.1	0.1	240.27	215.92	262.85	2.45·10 ⁻²	0.9019
MgCl ₂	17.1	0.4	0.1	0.1	240.26	215.87	262.85	2.45·10 ⁻²	0.9019
MgCl ₂	17.1	0.4	0.1	0.1	240.47	215.84	262.85	2.45·10 ⁻²	0.9019
MgCl ₂	17.1	0.4	0.1	0.1	240.44	215.82	262.85	2.45·10 ⁻²	0.9019
MgCl ₂	22.5	0.4	0.05	0.05	223.92	190.45	248.43	4.04·10 ⁻²	0.7848
MgCl ₂	22.5	0.4	0.05	0.05	224.72	190.34	248.43	4.04·10 ⁻²	0.7848
MgCl ₂	25.0	0.4	0.1	0.1	227.34	195.93	251.92	3.73·10 ⁻²	0.8111
MgCl ₂	25.0	0.4	0.1	0.1	227.44	196.05	251.90	3.73·10 ⁻²	0.8109

Table C.3: Heterogeneous freezing points of large droplets with suspended SiO_2 . The following abbreviations are used for the solutes: AS, SA and SI are $(\text{NH}_4)_2\text{SO}_4$, H_2SO_4 and 0.47 wt% SiO_2 , respectively. For each solute and concentration 8 freezing cycles are investigated, T_{f1} to T_{f8} . Temperatures are indicated Kelvin. Note that for the first two data series, 12 instead of 8 freezing points have been measured. The column comparison describes which freezing temperatures of the different series are compared with the Wilcoxon rank sum test. p is the probability that the two compared series are distinguishable or not and h indicates whether the null hypothesis (i.e. median of the series are equal) is rejected or not, respectively. $h=1$ means that the two compared series are statistically distinguishable. T_m and a_w are the mean ice melting points and the water activity at the mean ice melting point for the series containing SiO_2 globules.

Sample	Nr.	$T_{f1/5}$	$T_{f2/6}$	$T_{f3/8}$	$T_{f4/9}$	Comparison	p	h	T_m	a_w
H_2O	1	252.21	252.65	252.83	253.41	1 ↔ 2	$4.7 \cdot 10^{-4}$	1		1.0015
		253.18	253.16	252.97	253.41					
		252.72	252.90	252.54	252.88					
SI/ H_2O	2	252.35	254.97	254.05	255.42				273.25	1.0015
		255.85	254.51	255.64	254.84					
		254.85	254.09	253.67	254.34					
7.76 wt% AS	3	244.24	244.38	245.32	246.67	3 ↔ 4	$1.5 \cdot 10^{-4}$	1		
		245.47	245.93	246.29	245.86					
SI/7.73 wt% AS	4	252.13	252.48	252.26	251.68				271.77	0.9864
		247.25	251.78	251.39	251.97					
15.73 wt% AS	5	243.03	243.33	243.62	243.78	5 ↔ 6	$1.5 \cdot 10^{-4}$	1		
		243.02	242.81	243.09	243.17					
SI/15.73 wt% AS	6	247.39	247.32	246.13	246.06				268.80	0.9572
		245.60	246.26	246.14	247.00					
25.37 wt% AS	7	239.43	240.73	239.03	239.59	7 ↔ 8	$3.1 \cdot 10^{-4}$	1		
		237.68	235.80	236.18	235.80					
SI/25.44 wt% AS	8	245.43	245.17	244.44	244.22				264.45	0.9163
		243.93	242.11	241.69	240.39					
32.41 wt% AS	9	233.21	232.87	232.71	232.96	9 ↔ 10	$1.5 \cdot 10^{-4}$	1		
		234.31	234.03	235.07	232.15					
SI/32.67 wt% AS	10	236.48	236.36	236.36	236.80				260.25	0.8791
		236.62	236.54	235.86	236.73					
38.90 wt% AS	11	226.60	225.65	228.46	226.26	11 ↔ 12	$1.1 \cdot 10^{-4}$	0		
		226.82	226.32	227.35	226.26					
SI/39.00 wt% AS	12	228.44	229.67	228.12	231.05				256.24	0.8454
		227.87	231.29	229.14	229.82					
14.80 wt% LiCl	13	226.62	224.82	225.65	226.13	13 ↔ 14	$1.1 \cdot 10^{-4}$	1		
		228.01	227.31	227.94	230.33					
SI/14.90 wt% LiCl	14	230.07	229.64	230.30	230.42				252.32	0.8142
		230.73	230.88	230.98	230.95					
10.66 wt% SA	15	244.30	245.65	242.89	245.01	15 ↔ 16	$1.5 \cdot 10^{-4}$	1		
		244.35	243.55	243.37	244.01					
SI/10.83 wt% SA	16	246.81	246.39	247.74	249.32				267.67	0.9464
		245.84	246.22	245.80	245.88					

Seite Leer /
Blank leaf

Bibliography

- Albrecht, B. A., 1989. Aerosols, cloud microphysics and fractional cloudiness. *Science* 245, 1227–1230.
- Apelblat, A., Manzurola, E., 1987. Solubility of malonic, oxalic, succinic, adipic, malic, citric, and tartaric acids in water from 278.15 to 338.15 K. *J. Chem. Thermodynamics* 19, 317–320.
- Archuleta, C. M., DeMott, P. J., Kreidenweis, S. M., 2005. Ice nucleation by surrogates for atmospheric mineral dust and mineral dust/sulfate particles at cirrus temperatures. *Atmos. Chem. Phys.* 5, 2617–2634.
- Atkins, P. W., 1996. *Physikalische Chemie*. VCH, Weinheim.
- Baker, M. B., 1997. Cloud microphysics and climate. *Science* 276, 1072–1078.
- Becker, R., Döring, W., 1935. Kinetische Behandlung der Keimbildung in übersättigten Dämpfen. *Ann. Phys.* 24, 719–752.
- Benz, S., Megahed, K., Möhler, O., Saathoff, H., Wagner, R., 2005. T-dependent rate measurements of homogeneous ice nucleation in cloud droplets using a large atmospheric simulation chamber. *J. Photochem. Photobiol.* 176, 208–217.
- Bertram, A. K., Koop, T., Molina, L. T., Molina, M. J., 2000. Ice formation in $(\text{NH}_4)_2\text{SO}_4$ - H_2O particles. *J. Phys. Chem. A* 104, 584–588.
- Beyer, W. H., 1987. *CRC Handbook of Tables for Probability and Statistics*, 2nd Edition. CRC Press, Boca Raton.
- Braban, C. F., Carroll, M. F., Styler, S. A., Abbatt, J. P. D., 2003. Phase transitions of malonic and oxalic acid aerosols. *J. Phys. Chem. A* 107, 6594–6602.
- Brooks, S. D., Wise, M. E., Cushing, M., Tolbert, M. A., 2002. Deliquescence behavior of organic/ammonium sulfate aerosol. *Geophys. Res. Lett.* 29(19), 1917, doi:10.1029/2002GL014733.

- Cantrell, W., Heymsfield, A., 2005. Production of ice in tropospheric clouds: A review. *Bull. Amer. Meteor. Soc.* 86, 795–807.
- Chebbi, A., Carrier, P., 1996. Carboxylic acids in the troposphere, occurrence, sources, and sinks: A review. *Atmos. Environment* 30, 4233–4249.
- Chen, Y., Kreidenweis, S. M., McInnes, L. M., Rogers, D. C., DeMott, P. J., 1998. Single particle analyses of ice nucleating aerosols in the upper troposphere and lower stratosphere. *Geophys. Res. Lett.* 25, 1391–1394.
- Choi, M. Y., Chan, C. K., 2002. Continuous measurements of the water activities of aqueous droplets of water-soluble organic compounds. *J. Phys. Chem. A* 106, 4566–4572.
- Chylek, P., Ramaswamy, V., Ashkin, A., Dziedzic, J. M., 1983. Simultaneous determination of refractive index and size of spherical dielectric particles from light scattering data. *Appl. Opt.* 22, 2302–2307.
- Clarke, E. C. W., Glew, D. N., 1985. Evaluation of the thermodynamic functions for aqueous sodium chloride from equilibrium and calorimetric measurements below 154°C. *J. Phys. Chem. Ref. Data* 14, 489–610.
- Clegg, S. L., Brimblecombe, P., Wexler, A. S., 1998. Thermodynamic model of the system H^+ - NH_4^+ - SO_4^{2-} - NO_3^- - H_2O at tropospheric temperatures. *J. Phys. Chem. A* 102, 2137–2154.
- Colberg, C. A., Krieger, U. K., Peter, T., 2004. Morphological investigations of single levitated $\text{H}_2\text{SO}_4/\text{NH}_3/\text{H}_2\text{O}$ aerosol particles during deliquescence/efflorescence experiments. *J. Phys. Chem. A* 108(14), 2700–2709.
- Colberg, C. A., Luo, B. P., Wernli, H., Koop, T., Peter, T., 2003. A novel model to predict the physical state of atmospheric $\text{H}_2\text{SO}_4/\text{NH}_3/\text{H}_2\text{O}$ aerosol particles. *Atmos. Chem. Phys.* 3, 909–924.
- Cziczo, D. J., DeMott, P. J., Brooks, S. D., Prenni, A. J., Thomson, D. S., Baumgardner, D., Wilson, J. C., Kreidenweis, S. M., Murphy, D. M., 2004a. Observations of organic species and atmospheric ice formation. *Geophys. Res. Lett.* 31, doi:10.1029/2004GL019822.
- Cziczo, D. J., Murphy, D. M., Hudson, P. K., Thomson, D. S., 2004b. Single particle measurements of the chemical composition of cirrus ice residue during CRYSTAL-FACE. *J. Geophys. Res.* 109, D04201, doi:10.1029/2003JD004032.

- Dai, Y., Evans, J. S., 2001. Molecular Dynamics simulations of template-assisted nucleation: Alcohol monolayers at the air-water interface and ice formation. *J. Phys. Chem. B* 105, 10831–10837.
- DeMott, P. J., 2002. Laboratory studies of cirrus cloud processes. In: Lynch, D. K., Sassen, K., Starr, D. O. C., Stephens, G. (Eds.), *Cirrus*. Oxford Univ. Press, Oxford, pp. 102–135.
- DeMott, P. J., Chen, Y., Kreidenweis, S. M., Rogers, D. C., Sherman, D. E., 1999. Ice formation by black carbon particles. *Geophys. Res. Lett.* 26, 2429–2432.
- DeMott, P. J., Cziczo, D. J., Prenni, A. J., Murphy, D. M., Kreidenweis, S. M., Thomson, D. S., Borys, R., Rogers, D. C., 2003. Measurements of the concentration and composition of nuclei for cirrus formation. *Proc. Natl. Acad. Sci.* 100, 14655–14660.
- Diehl, K., Matthias-Maser, S., Jaenicke, R., Mitra, S. K., 2002. The ice nucleating ability of pollen: Part II. Laboratory studies in immersion and contact freezing modes. *Atmos. Res.* 61, 125–133.
- Dobler, A., 2003. Softwareentwicklung zur visuellen Untersuchung von heterogener Eiskernung. Semester thesis, ETH Zurich, Zurich, Switzerland.
- Duft, D., Leisner, T., 2004. Laboratory evidence for volume-dominated nucleation of ice in supercooled water microdroplets. *Atmos. Chem. Phys.* 4, 1997–2000.
- Eliassi, A., Modarress, H., Mansoori, G. A., 1999. Measurement of activity of water in aqueous poly(ethylene glycol) solutions (effect of excess volume on the Flory-Huggins χ -parameter). *J. Chem. Eng. Data* 44, 52–55.
- Ervens, B., Feingold, G., Frost, G. J., Kreidenweis, S. M., 2004. A modeling study of aqueous production of dicarboxylic acids: 1. Chemical pathways and speciated organic mass production. *J. Geophys. Res.* 109, D15205doi:10.1029/2003JD004387.
- Facchini, M. C., Mircea, M., Fuzzi, S., Charlson, R. J., 1999. Cloud albedo enhancement by surface-active organic solutes in growing droplets. *Nature* 401, 257–259.
- Fahey, D. W., Gao, R. S., Carslaw, K. S., Kettleborough, J., Popp, P. J., Northway, M. J., Holecek, J. C., Ciciora, S. C., McLaughlin, R. J., Thompson, T. L., Winkler, R. H., Baumgardner, D. G., Gandrud, B., Wennberg, P. O., Dhaniyala, S., McKinney, K., Peter, T., Salawitch, R. J., Bui, T. P., Elkins, J. W., Webster, C. R., Atlas, E. L., Jost, H., Wilson, J. C., Herman, R. L., Kleinböhl, A., von König, M., 2001. The detection of large HNO₃-containing particles in the winter Arctic stratosphere. *Science* 29, 1026–1031.

- Farkas, L., 1927. Keimbildungsgeschwindigkeit in übersättigten Dämpfen. *Z. Phys. Chem.* 125, 236–242.
- Finlayson-Pitts, B. J., Pitts, J. N. J., 2000. *Chemistry of the upper and lower atmosphere.* Academic Press, San Diego.
- Fukuta, N., 1963. Ice nucleation by metaldehyde. *Nature* 199, 475–476.
- Fukuta, N., 1966. Experimental studies of organic ice nuclei. *J. Atmos. Sci.* 23, 191–196.
- Gagosian, R. B., Peltzer, E. T., Zafriou, O. C., 1981. Atmospheric transport of continentally derived lipids to the tropical North Pacific. *Nature* 291, 312–314.
- Gasser, L., Jöri, M., 2004. Experimente zur Wasseraufnahme auf feste Aerosolpartikel unterhalb der Deliqueszenzfeuchte: Der Einfluss von Poren, Korngrenzen und Oberflächenmorphologie. Diploma thesis, ETH Zurich, Zurich, Switzerland.
- Gavish, M., Popovitz-Biro, R., Lahav, M., Leiserowitz, L., 1990. Ice nucleation by alcohols arranged in monolayers at the surface of water drops. *Science* 250, 973–975.
- Graddel, T. E., Crutzen, P. J., 1994. *Chemie der Atmosphäre.* Spektrum Akademischer Verlag, Heidelberg.
- Graham, B., Mayol-Bracero, O. L., Guyon, P., Roberts, G. C., Decesari, S., Facchini, M. C., Artaxo, P., Maenhaut, W., Köll, P., Andreae, M. O., 2002. Water-soluble organic compounds in biomass burning aerosols over Amazonia 1. Characterization by NMR and GC-MS. *J. Geophys. Res.* 107(D20), 8047, doi:10.1029/2001JD000336.
- Haag, W., Kärcher, B., Ström, J., Minikin, A., Lohmann, U., Ovarlez, J., Stohl, A., 2003. Freezing thresholds and cirrus cloud formation mechanisms inferred from in situ measurements of relative humidity. *Atmos. Chem. Phys.* 3, 1791–1806.
- Hansen, A. R., Beyer, K. D., 2004. Experimentally determined thermochemical properties of the malonic acid/water system: Implications for atmospheric aerosols. *J. Phys. Chem. A* 108, 3457–3466.
- Hemminger, W. F., Cammenga, H. K., 1989. *Methoden der thermischen Analyse.* Springer-Verlag, Berlin.
- Heneghan, A. F., Wilson, P. W., Haymet, A. D. J., 2002. Heterogeneous nucleation of supercooled water, and the effect of an added catalyst. *Proc. Natl. Acad. Sci.* 99, 9631–9634.
- Higuchi, K., Fukuta, N., 1966. Ice in capillaries of solid particles and its effect on their nucleating ability. *J. Atmos. Sci.* 23, 187–190.

- Hobbs, P., 1974. *Ice Physics*. Larendon Press, Oxford.
- Houghton, J., Ding, Y., Griggs, D. J., Nougier, M., van der Linden, P. J., Dai, X., Maskell, K., Johnson, C. A., 2001. *Climate Change 2001: The Scientific Basis*. Contribution of working group I to the Third Assessment Report of the Intergovernmental Panel on Climate Change. Cambridge University Press, United Kingdom and New York.
- Hoyle, C. R., Luo, B. P., Peter, T., 2005. The origin of high ice crystal number densities in cirrus clouds. *J. Atmos. Sci.* 62, 2568–2579.
- Hung, H. M., Malinowski, A., Martin, S. T., 2003. Kinetics of heterogeneous ice nucleation on the surfaces of mineral dust cores inserted into aqueous ammonium sulfate particles. *J. Phys. Chem. A* 107, 1296–1306.
- Jensen, E. J., Toon, O., 1997. The potential impact of soot particles from aircraft exhaust on cirrus clouds. *Geophys. Res. Lett.* 25, 249–252.
- Kabath, P., Stöckel, P., Baumgärtel, H., 2006. The nucleation of ice in supercooled D₂O and H₂O. *J. Mol. Liq.* 125, 204–211.
- Kanakidou, M., Seinfeld, J. H., Pandis, S. N., Barnes, I., Dentener, F. J., Facchini, M. C., Dingenen, R. V., Ervens, B., Nenes, A., Nielsen, C. J., Swietlicki, E., Putaud, J. P., Balkanski, Y., Fuzzi, S., Horth, J., Moortgat, G. K., Winterhalter, R., Myhre, C. E. L., Tsigaridis, K., Vignati, E., Stephanou, E. G., Wilson, J., 2005. Organic aerosol and global climate modelling: A review. *Atmos. Chem. Phys.* 5, 1053–1123.
- Kärcher, B., Busen, R., Petzold, A., Schröder, F. P., Schumann, U., Jensen, E. J., 1998. Physicochemistry of aircraft-generated liquid aerosols, soot and ice particles, 2. Comparison with observations and sensitivity studies. *J. Geophys. Res.* 103(D14), 17129–17147.
- Kärcher, B., Koop, T., 2005. The role of organic aerosols in homogeneous ice formation. *Atmos. Chem. Phys.* 5, 703–714.
- Kärcher, B., Lohmann, U., 2003. A parameterization of cirrus cloud formation: Heterogeneous freezing. *J. Geophys. Res.* 108(D14), 4402, doi:10.1029/2002JD003220.
- Kawamura, K., Ikushima, K., 1993. Seasonal changes in the distribution of dicarboxylic acids in the urban atmosphere. *Environ. Sci. Technol.* 27, 2227–2235.
- Kawamura, K., Sakaguchi, F., 1999. Molecular distributions of water soluble dicarboxylic acids in marine aerosols over the Pacific Ocean including tropics. *J. Geophys. Res.* 104, 3501–3509.

- Knopf, D. A., 2003. Thermodynamic properties and nucleation processes of upper troposphere and lower stratosphere aerosol particles. Phd thesis, ETH Zurich, Zurich, Switzerland.
- Koop, T., 2004. Homogeneous ice nucleation in water and aqueous solutions (Review article). *Z. Phys. Chem.* 218, 1231–1258.
- Koop, T., Bertram, A. K., Molina, L. T., Molina, M. J., 1999. Phase transitions in aqueous NH_4HSO_4 solutions. *J. Phys. Chem. A* 103, 9042–9048.
- Koop, T., Luo, B. P., Biermann, U. M., Crutzen, P. J., Peter, T., 1997. Freezing of $\text{HNO}_3/\text{H}_2\text{SO}_4/\text{H}_2\text{O}$ solutions at stratospheric temperatures: Nucleation statistics and experiments. *J. Phys. Chem. A* 101, 1117–1133.
- Koop, T., Luo, B. P., Tsias, A., Peter, T., 2000. Water activity as the determinant for homogeneous ice nucleation in aqueous solutions. *Nature* 406, 611–614.
- Koop, T., Ng, H. P., Molina, L. T., Molina, M. J., 1998. A new optical technique to study aerosol phase transitions: The nucleation of ice from H_2SO_4 aerosols. *J. Phys. Chem. A* 102, 8924–8931.
- Krämer, B., Hübner, O., Vortisch, H., Wöste, L., Leisner, T., Schwell, M., Rühl, E., Baumgärtel, H., 1999. Homogeneous nucleation rates of supercooled water measured in single levitated microdroplets. *J. Chem. Phys.* 111, 6521–6527.
- Kulmala, M., Pirjola, L., Mäkelä, J. M., 2004. Stable sulphate clusters as a source of new atmospheric particles. *Nature* 404, 66–69.
- Legrand, M., Preunkert, S., Galy-Lacaux, C., Lioussé, C., Wagenbach, D., 2005. Atmospheric year-round records of dicarboxylic acids and sulfate at three French sites located between 630 and 4360 m elevation. *J. Geophys. Res.* 110, D13302, doi:10.1029/2004JD005515.
- Lide, D. R., 1998. Handbook of Chemistry and Physics, 79th Edition. CRC Press, Boca Raton.
- Linke, W., 1958. Solubilities of inorganic and metal-organic compounds, Fourth Edition. American chemical society, Washington D.C.
- Lohmann, U., Feichter, J., 2005. Global indirect aerosol effects: A review. *Atmos. Chem. Phys.* 5, 715–737.
- Lohmann, U., Kärcher, B., 2002. First interactive simulations of cirrus clouds formed by homogeneous freezing in the ECHAM general circulation model. *J. Geophys. Res.* 107(D10), doi:10.1029/2001JD000767.

- Lohmann, U., Lesins, G., 2002. Stronger constraints on the anthropogenic indirect aerosol effect. *Science* 298, 1012–1015.
- Luo, B. P., Peter, T., Wernli, H., Fueglistaler, S., Wirth, M., Kiemle, C., Flentje, H., Yushkov, V. A., Khattatov, V., Rudakov, V., Thomas, A., Borrmann, S., Toci, G., Mazzinghi, P., Beuermann, J., Schiller, C., Cairo, F., Di-Donfrancesco, G., Adriani, A., Volk, C. M., Strom, J., Noone, K., Mitev, V., MacKenzie, R. A., Carslaw, K. S., Trautmann, T., Santacesaria, V., Stefanutti, L., 2003. Ultrathin Tropical Tropopause Clouds (UTTCS): II. Stabilization mechanisms. *Atmos. Chem. Phys.* 3, 1093–1100.
- Majewski, J., Margulis, L., Jacquemain, D., Leveiller, F., Bohm, C., Arad, T., Talom, Y., Lahav, M., Leiscrowitz, L., 1993. Electron diffraction and imaging of uncompressed monolayers of amphiphilic molecules on vitreous and hexagonal ice. *Science* 261, 899–902.
- Majewski, J., Popovitz-Biro, R., Bouwman, W. G., Kjaer, K., Als-Nielsen, J., Lahav, M., Leiscrowitz, L., 1995. The structural properties of uncompressed crystalline monolayers of alcohols $C_nH_{2n+1}OH$ ($n=13-31$) on water and their role as ice nucleators. *Chem. Euro. J.* 5, 304–311.
- Marculli, C., Luo, B. P., Peter, T., 2004a. Mixing of the organic aerosol fractions: Liquids as the thermodynamically stable phases. *J. Phys. Chem. A* 108, 2216–2224.
- Marculli, C., Luo, B. P., Peter, T., Wienhold, F. G., 2004b. Internal mixing of the organic aerosol by gas phase diffusion of semivolatile organic compounds. *Atmos. Chem. Phys.* 4, 2593–2599.
- Martin, S. T., 2000. Phase transitions of aqueous atmospheric particles. *Chem. Rev.* 100, 3403–3453.
- Middlebrook, A. M., Murphy, D. M., Thomson, D. S., 1998. Observations of organic material in individual marine particles at Cape Grim during the First Aerosol Characterization Experiment (ACE 1). *J. Geophys. Res.* 103(D13), 16475–16483.
- Murphy, D. M., Koop, T., 2005. Review of the vapour pressures of ice and supercooled water for atmospheric applications. *Q. J. R. Meteorol. Soc.* 131, 1539–1565.
- Murphy, D. M., Thomson, D. S., Mahoney, M. J., 1998. In situ measurements of organics, meteoric material, mercury and other elements in aerosols at 5 to 19 kilometers. *Science* 282, 1664–1669.
- Narukawa, M., Kawamura, K., Anlauf, K. G., Barrie, L. A., 2003a. Fine and coarse modes of dicarboxylic acids in the Arctic aerosols collected during the Polar Sunrise Experiment 1997. *J. Geophys. Res.* 108(D18), 4575, doi:10.1029/2003JD003646.

- Narukawa, M., Kawamura, K., Okada, K., Zaizen, Y., Makino, Y., 2003b. Aircraft measurements of dicarboxylic acids in the free tropospheric aerosol over the western central North Pacific. *Tellus* 55B, 777–786.
- Nolte, C. G., Schauer, J. J., Cass, G. R., Simoneit, B. R. T., 2001. Highly polar organic compounds present in wood smoke and in the ambient atmosphere. *Environ. Sci. Technol.* 35, 1912–1919.
- Novakov, T., Hegg, D. A., Hobbs, P. V., 1997. Airborne measurements of carbonaceous aerosols on the East Coast of the United States. *J. Geophys. Res.* 102(D25), 30023–30030.
- Novakov, T., Penner, J. E., 1993. Large contribution of organic aerosols to cloud-condensation-nuclei concentrations. *Nature* 365, 823–826.
- Nutt, D. R., Stone, A. J., 2003. Theoretical studies of the interface between water and Langmuir films of aliphatic alcohols. *J. Chem. Phys.* 119, 5670–5679.
- Parsons, M. T., Mak, J., Lipetz, S. R., Bertram, A. K., 2004. Deliquescence of malonic, succinic, glutaric, and adipic acid particles. *J. Geophys. Res.* 109, D06212, doi:10.1029/2003JD004075.
- Parungo, F. P., Lodge Jr., J. P., 1965. Molecular structure and ice nucleation of some organics. *J. Atmos. Sci.* 22, 309–313.
- Petit, J. R., Jouzel, J., Raynaud, D., Barkov, N. I., Barnola, J.-M., Basile, I., Bender, M., Chappellaz, J., Davis, M., Delaygue, G., Delmotte, M., Kotlyakov, V. M., Legrand, M., Lipenkov, V. Y., Lorius, C., Pépin, L., Ritz, C., Saltzman, E., Stievenard, M., 1999. Climate and atmospheric history of the past 420,000 years from the Vostok ice core, Antarctica. *Nature* 399, 429–436.
- Popovitz-Biro, R., Wang, J. L., Majewski, J., Shavit, E., Leiserowitz, L., Lahav, M., 1994. Induced freezing of supercooled water into ice by self-assembled crystalline monolayers of amphiphilic alcohols at the air-water interface. *J. Am. Chem. Soc.* 116, 1179–1191.
- Prenni, A. J., DeMott, P. J., Kreidenweis, S. M., Sherman, D. E., Russell, L. M., Ming, Y., 2001. The effects of low molecular weight dicarboxylic acids on cloud formation. *J. Phys. Chem. A* 105, 11240–11248.
- Pruppacher, H. R., Jaenicke, R., 1995. The processing of water vapor and aerosols by atmospheric clouds, a global estimate. *Atmos. Res.* 38, 283–295.
- Pruppacher, H. R., Klett, J. D., 1997. *Microphysics of clouds and precipitation*. Kluwer, Dordrecht.

- Rasmussen, D. H., 1982. Thermodynamics and nucleation phenomena - A set of experimental observations. *J. Cryst. Growth* 56, 56–66.
- Rasmussen, D. H., MacAulay, M. N., MacKenzie, A. P., 1975. Supercooling and nucleation of ice in single cells. *Cryobiology* 12, 328–339.
- Rasmussen, D. H., MacKenzie, A. P., 1972. Effect of solute on ice-solution interfacial free energy; calculation from measured homogeneous nucleation temperatures. In: Jellinek, H. H. G. (Ed.), *Water structure at the water polymer interface*. Plenum Press, New York, pp. 126–145.
- Rosinski, J., 1980. Heterogeneous nucleation of ice on surfaces of liquids. *J. Phys. Chem.* 84, 1829–1832.
- Sassen, K., 2002. Cirrus clouds, a modern perspective. In: Lynch, D. K., Sassen, K., Starr, D. O. C., Stephens, G. (Eds.), *Cirrus*. Oxford Univ. Press, Oxford, pp. 11–40.
- Sassen, K., DeMott, P. J., Prospero, J. M., Poellot, M. R., 2003. Saharan dust storms and indirect aerosol effects on clouds: CRYSTAL-FACE results. *Geophys. Res. Lett.* 30, 1633, doi:10.1029/2003GL017371.
- Schönwiese, C. D., 2003. *Klimatologie*, 2nd edition. Ulmer, Stuttgart.
- Schumann, U., 2002. Contrail cirrus. In: Lynch, D. K., Sassen, K., Starr, D. O. C., Stephens, G. (Eds.), *Cirrus*. Oxford Univ. Press, Oxford, pp. 231–255.
- Seeley, L. H., Seidler, G. T., 2001a. Preactivation in the nucleation of ice by Langmuir films of aliphatic alcohols. *J. Chem. Phys.* 114, 10464–10470.
- Seeley, L. H., Seidler, G. T., 2001b. Two-dimensional nucleation of ice from supercooled water. *Phys. Rev. Lett.* 87, doi:10.1103/PhysRevLett.87.055702.
- Seinfeld, J. H., Pandis, S. N., 1998. *Atmospheric chemistry and physics*. John Wiley & Sons, Inc., New York.
- Simoneit, B. R. T., Cardoso, J. N., Robinson, N., 1991. An assessment of terrestrial higher molecular weight lipid compounds in aerosol particulate matter over the South Atlantic from about 30–70°S. *Chemosphere* 23, 447–465.
- Smith, R. S., Kay, B. D., 1999. The existence of supercooled liquid water at 150 K. *Nature* 398, 788–791.
- Stephanou, E. G., 1992. Biogenic and anthropogenic organic compounds in eolian particulates in the east Mediterranean region: I. Occurrence and origin. *Atmos. Environ.* 26A, 2821–2829.

- Stephen, H., Stephen, T., 1963. Solubilities of inorganic and organic compounds. Pergamon Press, Oxford.
- Stöber, W., Fink, A., Bohn, E., 1968. Controlled growth of monodisperse silica spheres in the micron size range. *J. Colloid. Interface. Sci.* 26, 62–69.
- Stöckel, P., Weidinger, I. M., Baumgärtel, H., Leisner, T., 2005. Rates of homogeneous ice nucleation in levitated H₂O and D₂O droplets. *J. Phys. Chem. A* 109, 2540–2546.
- Ström, J., Seifert, M., Kärcher, B., Ovarlez, J., Minikin, A., Gayet, J.-F., Krejci, R., Petzold, A., Auriol, F., Haag, W., Busen, R., Schumann, U., Hansson, H. C., 2003. Cirrus cloud occurrence as function of ambient relative humidity: A comparison of observations obtained during the INCA experiment. *Atmos. Chem. Phys.* 3, 1807–1816.
- Tabazadch, A., Toon, O. B., 1998. The role of ammoniated aerosols in cirrus cloud nucleation. *Geophys. Res. Lett.* 25, 1379–1382.
- Taubenheim, J., 1969. Statistische Auswertung geophysikalischer und meteorologischer Daten. Akademische Verlagsgesellschaft Geest & Portig, Leipzig.
- Turnbull, D., Fisher, J. C., 1949. Rate of nucleation in condensed systems. *J. Chem. Phys.* 17, 71–73.
- van Helden, A. K., Jansen, J. W., Vrij, A., 1981. Preparation and characterization of spherical monodisperse silica dispersions in nonaqueous solvents. *J. Colloid. Interface. Sci.* 81, 354–368.
- Volmer, M., Weber, A., 1926. Keimbildung in übersättigten Gebilden. *Z. Phys. Chem.* 119, 277–301.
- Wayne, R. P., 2000. Chemistry of atmospheres, Third Edition. University Press, Oxford.
- Wise, M. E., Garland, R. M., Tolbert, M. A., 2004. Ice nucleation in internally mixed ammonium sulfate/dicarboxylic acid particles. *J. Geophys. Res.* 109, D19203, doi:10.1029/2003JD004313.
- Wise, M. E., Surratt, J. D., Curtis, D. B., Shilling, J. E., Tolbert, M. A., 2003. Hygroscopic growth of ammonium sulfate/dicarboxylic acids. *J. Geophys. Res.* 108(D20), 4638, doi:10.1029/2003JD003775.
- WMO, 1956. International cloud atlas. WMO, Geneva.
- Yao, X. H., Fang, M., Chan, C. K., 2002. Size distributions and formation of dicarboxylic acids in atmospheric particles. *Atmos. Environment* 36, 2099–2107.

- Yu, F., Turco, R. P., 1998. Contrail formation and impacts on aerosol properties in aircraft plumes: Effects of fuel sulfur content. *Geophys. Res. Lett.* 25, 313–316.
- Zaizen, Y., Okada, K., Ikegami, M., Sawa, Y., Makino, Y., 2004. Number-size distributions of aerosol particles in the free troposphere over the Northwestern Pacific ocean-influence of Asian outflow and tropical air transport. *J. Meteo. Soc. Japan* 82, 1147–1160.
- Zeldovich, Y. B., 1942. Theory of new-phase formation: Cavitation. *J. Exp. Theor. Phys.* 12, 525–538.
- Zhang, Y., Macke, A., Albers, F., 1999. Effect of crystal size spectrum and crystal shape on stratiform cirrus radiative forcing. *Atmos. Res.* 52, 59–75.
- Zobrist, B., 2001. Untersuchungen zum Gefrierverhalten von wässrigen Polyethylenglykol-Lösungen mit einem selbstentwickelten Kalorimeter. Diploma thesis, ETH Zurich, Zurich, Switzerland.
- Zobrist, B., Marcolli, C., Koop, T., Luo, B. P., Murphy, D. M., Corti, T., Zardini, A., Lohmann, U., Fueglistaler, S., Cziczo, D. J., Krieger, U. K., Hudson, P. K., Thomson, D. S., Peter, T., 2006. Oxalic acid as a heterogeneous ice nucleus in the upper troposphere and its indirect aerosol effect. *Atmos. Chem. Phys. Discuss.* 6, 3571–3609.
- Zobrist, B., Weers, U. G., Koop, T., 2003. Ice nucleation in aqueous solutions of poly[ethylene glycol] with different molar mass. *J. Chem. Phys.* 118, 10254–10261.
- Zuberi, B., Bertram, A. K., Cassa, C. A., Molina, L. T., Molina, M. J., 2002. Heterogeneous nucleation of ice in $(\text{NH}_4)_2\text{SO}_4\text{-H}_2\text{O}$ particles with mineral dust immersions. *Geophys. Res. Lett.* 29(10), doi:10.1029/2001GL014289.
- Zuberi, B., Bertram, A. K., Koop, T., Molina, L. T., Molina, M. J., 2001. Heterogeneous freezing of aqueous particles induced by crystallized $(\text{NH}_4)_2\text{SO}_4$, ice, and letovicite. *J. Phys. Chem. A* 105, 6458–6464.

Seite Leer /
Blank leaf

Acknowledges

Over the past three years, many colleagues, friends and family members have strongly supported and encouraged me for this work. I am hardly convinced that I would not have finished this work without their help. It is not so easy for me to express my sentiments and impressions of the last years in words, but ...

I thank

- Thomas Peter who gave me the possibility to do this work in his group (I never had such a short interview). I appreciated your advices for my work and your engagement and energy to bring forward science in general with so much pleasure and humor.
- Thomas Koop, who was over the past five years my tutor, or der grosse Meister, and I was the little apprentice. I would not have start this work without you. He taught me the secrets of supercooled water and ice. Hopefully, I will have soon another lesson at the Venezia.
- Claudia Marcolli to be first a pleasant and helpful room mate and then my other tutor. I had the great fortune to have two awesome tutors!! I extremely appreciated our long discussions and your tremendous energy for my work.
- René Schwarzenbach for being my "objective" co-examiner.
- Beiping Luo for patiently introducing and teaching me in microphysics and fortran. Further, I will never forget the lovely badminton fights we had.
- Marc Wüest, Peter Isler, Ruedi Lüthi and Dani Lüthi for technical and infrastructural support.
- Petra Forney and Eva Choffat for administrative advice.
- All the co-authors of the Science Paper.
- Andreas Dobler for helping me to built up the single cooling apparatus, essentially writing the Labview interface. I enjoyed to be the adviser of your Semesterarbeit.

- Uwe Weers for supporting me in different problems of my work and for a nice trip on the boat. Frikadellen!! In the case you ever will open a bar, I will help out as a waiter, and of course will wear a white chemise.
- Edwin Hausammann for technical help for my experiments. Is there still a TV in the garage?? Let's go Roger!
- Daniel DJ Knopf for a wonderful time in our large laboratory in the M-floor and in several other places in Zürich. You know what it means to be a member of the subgroup Koop, but we both survived!!
- Michaela Hegglin, my little "Winselprinzessin", for a wonderful time in Sardinia.
- Maurus Hess showing a Zürcher the culture of Basel and Obwalden.
- my former office mates, Micha Semmler and Frank Wienhold in the L11 at the HPP, the Italian Mafia, Alessandro Zardini and Jacob Balzani in the D24 as well as my new office mates Stefan Gedamke and Mathieu Nicolet for a nice time.
- Christina Colberg and Christian Braun for giving also non-scientific inputs in the group! NERD!!
- all the other members of the IAC for having a nice time at the institute.
- Beatrice and Jörg for giving me the opportunity and freedom to choose my own way and for supporting that way.
- Mats for being there when a real brother is needed.
- Matschi for a close friendship over the last 15 years, and for articulating that there is more besides a Ph.D-thesis.
- Sebi, Schnitzel, Sürbel, Anu, Sonja, Chanti, Mio and all my other friends. From now on, I will have more time to spent with you!
- the soccer team of Toni Polsteri. Nice Shirt!!
- Silja for giving me the encouragement and love that I needed. Ti amo!!

Curriculum Vitae

Bernhard Zobrist

Date of birth: 10.06.1975
Citizen: Rapperswil (AG)

Education

1982 - 1991: Elementary School in Uster, ZH.
1991 - 1996: Graduate in Type C at the Cantonal Schools in Wetzikon, ZH.
1996 - 2001: Studies of Earth science at ETH Zurich.
2001 : Diploma thesis at the Institute for atmospheric and climate science, ETH Zurich.
2002 - 2005: Ph.D. doctoral thesis at the Institute for atmospheric and climate science, ETH Zurich.

Profession

1994 - 2000: Private teacher for mathematics, chemistry and physics.
1996 : Mailman in the post office of Uster, ZH.